

MEASUREMENT OF TURBULENT FLAME SPEEDS OF HYDROGEN AND
NATURAL GAS BLENDS (C1-C5 ALKANES) USING A NEWLY DEVELOPED
FAN-STIRRED VESSEL

A Dissertation

by

SANKARANARAYANAN RAVI

Submitted to the Office of Graduate and Professional Studies of
Texas A&M University
in partial fulfillment of the requirements for the degree of

DOCTOR OF PHILOSOPHY

Chair of Committee,	Eric L Petersen
Committee Members,	Gerald L Morrison
	Devesh Ranjan
	Adonios Karpetis
	Felix Güethe
Head of Department,	Andreas Polycarpou

May 2014

Major Subject: Mechanical Engineering

Copyright 2014 Sankaranarayanan Ravi

ABSTRACT

A fan-stirred flame speed vessel was developed at Texas A&M University to conduct turbulent combustion studies. Four high-speed impellers were installed in a central-symmetric pattern at the central circumference of an existing cylindrical laminar flame bomb. The fans generated homogeneous and isotropic turbulence with negligible mean flow ($< 10\% u'$) at the vessel center, and flames up to 12.7 cm in diameter can be measured. The fan designs were optimized using particle image velocimetry inside a Plexiglas model of the vessel. The uniformity of the flow fields was verified using spatial uniformity maps, two-point correlations, and the energy spectra. Additionally, the capability to independently vary the intensity level and the integral length scale was developed. Where the former changed with fan speeds, increasing the blade pitch angle of the impeller decreased the integral length scale.

Turbulent flame speeds of fuels that are of topical interest to gas turbines were measured in the fan-stirred bomb. Schlieren photography was used to visualize the flame growth under constant-pressure conditions, and the captured images were processed using an edge-detection code developed in-house. The equivalent-circle-area method was used to determine the flame radii. The shot-to-shot variability was minimal, which resulted in a low experimental scatter close to 10 cm/s. The flame speeds increased with radius due to flame acceleration. Effective turbulent intensity levels were estimated which increased progressively with flame radius.

A systematic approach was followed to determine the effects of hydrogen addition on the turbulent displacement speeds of alkanes (C1-C3). Particularly, a natural gas surrogate (NG2) containing large amounts of C2+ hydrocarbons (>20%) was studied. Turbulent displacements were higher for alkane mixtures with Lewis number below unity than those with $Le > 1$. NG2 and methane gave near-identical turbulent displacement speeds consistent with the laminar flame speed trends. Similar trends in displacement speeds were observed for blends of NG2/H₂ and CH₄/H₂, thus validating the newly established experimental technique. Additionally, turbulent flame speeds of hydrogen and a generic, high-hydrogen-content syngas blend (50:50 H₂:CO) were studied. The wide range of laminar flame speeds explored herein revealed significantly different flame surface features between the various regimes of turbulent combustion.

To my parents

ACKNOWLEDGMENTS

I'm eternally indebted to Dr. Petersen who hired me even though I had no prior combustion research experience. The past four years have been an enriching experience and the lessons learnt go far beyond this dissertation.

I would like thank the committee members for reading the dissertation and providing valuable inputs. Dr. Felix Güethe, Alstom is acknowledged for fruitful discussions regarding the experimental test matrix.

I would like to thank to all my friends from inside and outside the lab for their love and support. I would like to extend my gratitude to Texas A&M University for being a gracious host to a foreigner for the past six years and helping me successfully complete this degree.

Special thanks to my wife, Priya, for agreeing to marry me when I didn't have a real job!

This project was funded by the National Energy Technology Laboratory of the US Department of Energy through the UTSR grant No. DE-FE0004679. Additional financial support from Alstom, Switzerland is acknowledged.

TABLE OF CONTENTS

	Page
ABSTRACT	ii
ACKNOWLEDGMENTS.....	v
TABLE OF CONTENTS	vi
LIST OF FIGURES.....	ix
LIST OF TABLES	xiii
CHAPTER I INTRODUCTION	1
CHAPTER II PREMIXED TURBULENT COMBUSTION	4
1. Laminar flames.....	6
2. Turbulent flame brush	7
3. Reaction progress variable	11
4. Turbulent propagation rates- definition dependency	13
5. Turbulent combustion regime diagram	15
6. Summary	22
CHAPTER III FAN-STIRRED BOMBS.....	25
1. Measurement techniques	26
2. Dependencies of turbulent flame speeds	28
3. Acceleration of spherical turbulent kernels.....	31
4. Self-similar scaling of turbulent flames	36
5. Summary	38
CHAPTER IV IMPELLER DESIGN STUDY	41
1. Introduction	41
2. Background literature	42
a. HIT inside a confined volume.....	42
b. Spherically expanding turbulent flames.....	45
3. Experimental setup and impeller design methodology	49
4. Particle image velocimetry system.....	53
5. Turbulence statistics	55
a. Mean flow, RMS intensity, and velocity PDF	55

b. Homogeneity and isotropy ratios	60
6. Two-point velocity correlations	63
7. Energy spectra	67
8. Turbulent kinetic energy dissipation rate and turbulence statistics.....	70
a. Dissipation rate (ϵ)	70
b. Turbulent statistics	71
9. Discussion	76
10. Summary	77
CHAPTER V EXPERIMENTAL SETUP	80
1. Existing facility description	80
2. Apparatus description.....	83
3. Experimental procedure and data analysis	85
4. Measurement uncertainties.....	90
5. Summary	92
CHAPTER VI RESULTS	93
1. Results	94
a. Pure-fuel flame speeds	94
b. Natural gas blends	99
c. Effects of hydrogen addition on the displacement speeds	100
2. Discussion	105
a. Borghi diagram.....	105
b. NG2-alkane comparison.....	107
CHAPTER VII CONCLUSIONS	112
1. Summary	112
2. Recommendations for future efforts	114
REFERENCES	116
APPENDIX A FUNDAMENTALS OF TURBULENT FLOWS	121
1. Characteristics of turbulence	122
2. Single-point correlation.....	123
3. Energy cascade and Kolmogorov hypotheses	124
a. First hypothesis- local isotropy	125
b. Second hypothesis- first similarity hypothesis.....	125
c. Third hypothesis- second similarity hypothesis	127
4. Two-point correlations	128
a. Integral (Euler) scales.....	129
b. Taylor scales.....	130

5. Energy spectrum.....	131
6. Non-dimensional numbers for turbulent combustion.....	135
References	137

LIST OF FIGURES

	Page
Figure 1. Turbulent flame brush thickness. Developing flame brush (brush thickness varies spatially or temporally) - (a) Bunsen burner (b) v-flame (c) fan-stirred bomb. Fully developed flame brush (characterized by constant brush thickness) (d) stagnation flow burner (e) low-swirl burner.	9
Figure 2. (c) Isocontours for various flame configurations- (a) stagnation flow-stabilized burner (b) V-Flame (c) Bunsen burner (d) spherically (statistical) expanding flame. The various isocontours in spherical flames are identified by their corresponding radii.	13
Figure 3. Classical turbulent combustion regime diagram (Borghi diagram).	18
Figure 4. Modified Borghi diagram as described by Peters [17] showing the thin-reaction zone.	19
Figure 5. Non-dimensional power spectral density function normalized by the Kolmogorov scale.	34
Figure.6. Effective turbulent intensity (Eq. 15) seen by the flame (u'_{k}) normalized by the fan-generated intensity level ($u' \sim 1.5$ m/s) for a stoichiometric ethane-air mixture (shown as the curve).	35
Figure.7. Flame surface dissipation spectrum as described by Chaudhuri et al. [2].	37
Figure 8. Self-similar scaling for methane-air mixture at $\phi = 0.9$	38
Figure 9. Schematic of the experimental arrangement.	51
Figure 10. Geometrical parameters for the impellers used in this study.	52

Figure 11. (a) Instantaneous velocity field (b) Mean velocity field for prototype 1. d. ...	57
Figure 12. Velocity PDFs for all prototypes: (a) Prototype #1 (b) Prototype #3- Higher number of blades (c) greater pitch angle.	59
Figure 13. (a) x_2 -Homogeneity map (b) Isotropy map for prototype #1.	62
Figure 14. CDFs of the spatial plots of (a) x_1 -Homogeneity (H_{x1}) (b) x_2 -Homogeneity (H_{x2}) (c) Isotropy (I) ratios for the various prototypes..	65
Figure 15. Correlation coefficients of the impellers in the longitudinal and lateral directions.....	66
Figure 16. Energy spectra for all prototypes.	69
Figure 17. 2-point velocity longitudinal correlations extrapolated to reach zero crossing	75
Figure 18. Aluminum laminar flame bomb at Texas A&M University.....	81
Figure 19. Laminar flame speeds of C1-C3 hydrocarbons in air over a wide range of equivalence ratios.	82
Figure 20. Fan-stirred flame speed vessel. (a) SOLIDWORKS model (b) photograph of the facility.....	83
Figure 21. Detailed views of the impeller assembly..	85
Figure 22. Sample images from a typical turbulent flame speed experiment.	86
Figure 23. (a) Flame radius evolution for laminar and turbulent conditions. (b) Turbulent flame speeds with (curve) and without (symbols) the smoothing	

filter. (c) Global displacement speeds from three different separate trials (symbols). (d) A good collapse of $ST, 0.1$ from four different trials can be seen at various u_k' 89

Figure 24. Histogram of the experimental scatter estimated from three different trials at each condition for methane-air mixtures at different equivalence ratios..... 91

Figure 25. Experimental scatter for turbulent flame speed experiments..... 91

Figure 26. Turbulent radii-history (a) methane (b) ethane (c) propane. All three repeats are shown for (b) and (c). Only two repeats are shown for (a) for clarity. Good repeatability is evident for all the cases. (d) Density ratios of the mixtures at different equivalence ratios..... 97

Figure 27. (a) Laminar flame speeds of alkane-air mixtures. (b-d) Turbulent flame speeds of C1-C3 alkanes/air mixtures as a function of the effective turbulence intensity..... 98

Figure 28. (a) Turbulent radius growth for NG2 mixtures. (b) Displacement speeds of NG2/air premixtures. 100

Figure 29. Turbulent flame radii evolution for (a) H₂/air (b) Syngas (50:50 H₂:CO) (c) 50:50 H₂:CH₄ (d) 75:25 NG₂: H₂ (e) 50:50 NG₂: H₂ 103

Figure 30. Global displacement speeds of (a) H₂/air (b) Syngas (50:50 H₂:CO) (c) 50:50 H₂:CH₄ (d) 75:25 NG₂: H₂ (e) 50:50 NG₂: H₂..... 104

Figure 31. Borghi diagram showing the different regimes of turbulent flame propagation. 106

Figure 32. Comparison of turbulent flame speeds of NG₂ and methane mixtures. 109

Figure 33. Displacement speeds of alkanes and NG₂ at (a) fuel-lean (b) stoichiometric (c) fuel-rich conditions..... 110

Figure 34. (a) Laminar flame speeds (curves are model predictions) of NG2 and CH4 with varying levels of H2. (b) Turbulent displacement speed for these mixtures measured herein.....	111
Figure 35. Variations of typical longitudinal and lateral correlation functions with separation distance.....	129
Figure 36. Energy-spectrum function normalized by the Kolmogorov length scale at $R_\lambda = 500$	132
Figure 37. Dissipation spectrum (solid line) at $R_\lambda = 600$. The cumulative dissipation is also shown (dashed line).....	133
Figure 38. Energy spectra at various Re scaled with the integral scale in (a) and with the Kolmogorov scale in (b).	134

LIST OF TABLES

	Page
Table 1. Radii and burning velocity ratios of different measurement surfaces with respect to the schlieren surface as measured by Bradley et al. [15].	31
Table 2. Facility survey of spherically expanding turbulent flames	49
Table 3. Prototype specifications used in this study.	53
Table 4. Mean, Spatial RMS and higher order moments- skewness and kurtosis for all prototypes	58
Table 5. Turbulence statistics for all prototypes	73
Table 6. Integral length scale computations. The values are in millimeters	76
Table 7. Integral length scales inside a typical gas turbine	77
Table 8. Various turbulence parameters for the turbulent flame speed experiments.....	94
Table 9. Properties of hydrogen- and C1-C3 alkane-air mixtures studied herein.....	96
Table 10. Properties of NG2-air mixtures studied herein	99
Table 11. Properties of blends containing hydrogen.....	102

CHAPTER I

INTRODUCTION

Significant progress has been achieved in the accurate measurements of flame propagation rates under laminar conditions. The laminar flame speed is a fundamental property of a combustible mixture that depends solely on the system pressure, temperature, and equivalence ratio. The measured laminar flame speed (corrected for geometry-induced and flame-stretch effects) can be used to validate chemical kinetics mechanisms. Another application of laminar flame speeds is to predict turbulent flame propagation rates using correlations which are mostly fitted to a specific experimental database. Hence, such propagation rates, unlike the laminar case, cannot be unambiguously defined.

Nevertheless, with the advent of laser imaging, several definitions of turbulent burning rates have been identified [1]. Recently, a self-similar scaling of spherically expanding flames has been successfully derived [2], and a unified scaling factor has been demonstrated using data from several fan-stirred bombs (including data from the rig developed herein). Such results are promising and aid in systematically compiling a comprehensive database of turbulent propagation rates of common and potential fuels of interest to gas turbines and IC engines alike.

The main objective of this dissertation was to extend the capability of an existing, high-pressure laminar flame bomb at the author's laboratory to measure turbulent flame speeds.

Typically, mixing fans are installed inside such flame bombs to generate the desired levels of turbulence. A logical approach was followed to achieve this objective. Five major tasks were identified and are described below.

1. Utilize existing infrastructure- the primary objective was to upgrade the existing facility in a cost-effective manner and with minimal modification to the original apparatus. Care was taken to ensure that the structural integrity of the vessel was not comprised under post-combustion pressures and temperatures.
2. Optimize fan geometry- fan designs were optimized to generate uniform turbulent conditions inside the flame bomb. Subsequently, the flow fields generated by the fans were accurately quantified.
3. Develop flexibility to vary turbulence parameters- Turbulent conditions inside such flame bombs are described using the intensity level and the integral length scale. Consequentially, flame speed correlations developed from fan-stirred data are affected by such geometric factors. To address this issue, the flexibility to independently vary the intensity levels and the length scale of turbulence was added.
4. Establish the measurement technique for turbulent flame speeds- various diagnostic techniques associated with fan-stirred bombs cited in the literature were reviewed. Schlieren imaging is not only convenient but also provides well-defined flame propagation rates. Automated image-analysis and post-processing procedures were developed exclusively for turbulent combustion.

5. Conduct turbulent flame speed experiments- preliminary measurements of alkane-hydrogen blends were measured over a wide range of conditions, and the rig capability was successfully demonstrated.

This dissertation discusses each of these tasks in detail and is organized as follows. The theory of premixed turbulent combustion is discussed in detail in Chapter II. A primer on the fundamentals of turbulent flow is given in Appendix-A. The advantages and challenges associated with fan-stirred bombs are elaborated in Chapter III. These chapters together provide a comprehensive review of the background information needed for measurements of turbulent flame speeds. An extensive survey of fan-stirred facilities reported in the literature is presented in the impeller design study in Chapter IV. The flow field characteristics of the optimized fans are then analyzed in detail. The features of the newly developed turbulent flame speed vessel are described in Chapter V. The post-processing procedure used to estimate turbulent flame speeds is also explained. Turbulent flame speed results of alkanes, natural gas blends, and several hydrogen-based mixtures measured using the newly developed flame bomb are reported in Chapter VI. Finally, recommendations for future work are suggested in Chapter VII.

CHAPTER II

PREMIXED TURBULENT COMBUSTION

Premixed turbulent combustion is a significantly complex and is not completely understood. Comparison of turbulent flame speeds of two fuels at two different turbulent conditions remains challenging to this day [3]. Nevertheless, significant progress has been made in determining the general characteristics of premixed turbulent flame propagation. Lipatnikov and Chomiak [4] provide a critical assessment of the state-of-the-art experimental databases on turbulent flame speeds (S_T). Some important trends from that review paper and others are summarized below.

1. Turbulent flame speeds (S_T) are higher than laminar flame speeds due to surface area increase from the wrinkling by turbulent eddies. This phenomenon is called turbulent-stretching. Turbulent-stretching or vortex-stretching results in the energy cascade between the large scale and small-scale eddies, and subsequently leads to an exponential increase in material surface area increase (through wrinkling) ([5], [6]). However, self-propagation effects wherein wrinkled laminar flamelets coalesce partially limits the surface area created by turbulent stretching.
2. Turbulent flame speeds show a non-linear behavior with turbulent intensity. S_T initially increases as the turbulent intensity levels are increased, attains a maximum, and decreases beyond it (bending effect) eventually resulting in flame quenching by

excessive turbulence. The intensity level associated with the maximum is highly dependent on the fuel and the apparatus and cannot be generalized.

3. Effect of turbulent length scales on S_T is not well understood, and contrasting viewpoints are present in the literature (see Chapter IV for further discussion). This discordance is mainly due to the scarcity of datasets focusing on the effect of turbulent length scale on S_T .
4. The effect of pressure on S_T is also controversial. Kobayashi et al. [7] showed that S_T increased with pressure due to the decrease in mixture thermal-diffusivity thereby promoting flame-instability through a subsequent reduction in flame thickness. Recently, Liu et al. [8] suggested that the enhancement of turbulent flame speeds with pressure is a manifestation of the enhancement of turbulent Reynolds number (Re) with pressure. They showed that S_T decreased with pressure similar to laminar flame speeds at constant Reynolds number in a fan-stirred bomb. But, they achieved constant Re by changing the intensity levels and the integral length scale at elevated pressures. So the observed reduction in S_T with pressure can also be related to the reduction in u' .
5. Higher values of S_T are associated with mixtures characterized by Lewis numbers (Le -defined as the ratio of the mixture thermal diffusivity to the mass diffusivity of the deficient species into the diluent) less than unity than for those with $Le > 1$. The local burning rates of stretched flamelets (laminar flame segments in a turbulent flow) are significantly enhanced for mixtures with $Le < 1$ which result in higher values of S_T . More-detailed discussion is presented in Chapter VI.

As evident, isolating the sensitivity of S_T to any one particular parameter is extremely challenging in addition to the highly non-linear behavior of S_T . A main objective of this study was to develop an apparatus in which the turbulent intensity and integral length scale can be independently varied. As a good starting point, this chapter introduces the various terminologies used in premixed turbulent combustion and is organized as follows. First, a brief introduction to laminar flames is presented. The turbulent flame brush is defined, and it is then used to classify the different flame geometries commonly used in premixed turbulent combustion research. The concept of reaction progress variable is discussed in detail, and the various flame surfaces based on different diagnostics are identified. The ambiguity in clearly defining turbulent propagation rates (definition-dependency) is then clarified. Finally, various regimes of turbulent combustion (Borghi diagram) are discussed in detail.

1. Laminar flames

This discussion is restricted to spherically expanding flames due to their direct relevance to this study. Other geometries and methods associated with laminar flame speed measurements are discussed in detail by de Vries [9]. A spherically expanding flame is one of the canonical geometries for measuring laminar propagation rates. The experimental apparatus consists of a closed cylindrical or spherical chamber with a provision for central spark-ignition. Once initiated, a spherical flame propagates under near-constant-pressure conditions followed by a significant pressure rise (typically 10

times the initial pressure). Flame propagation rates are estimated by optically tracking the radius growth and/or using a thermodynamic model applied to the dynamic pressure trace of the combustion process.

Two types of velocity can be measured in flame bombs [10]. First is associated with the propagation speed of the leading edge (any other surface inside the flame can be chosen depending on the diagnostics) of the flame into an unburnt mixture. Such a quantity is called an entrainment or engulfment velocity or displacement speed, and denotes the rate at which unburnt gases are consumed at the flame front. Another type of velocity which when multiplied by the burnt-gas density yields the rate of production of burnt gases can be estimated using the pressure trace from a dynamic pressure transducer inside the flame bomb. Such a velocity is referred to as the laminar burning velocity. Flame speeds are of direct relevance to IC engine designers who are interested in the distance transversed by a flame upon ignition. The latter quantity (burning velocity) is particularly useful in safety applications to estimate the pressure-rise from explosions. The two velocities are equal for planar (stretch-free) flames.

2. Turbulent flame brush

A laminar flame front can be defined as a high-temperature zone (thin wave) moving into a combustible mixture at the laminar flame speed. On the contrary, a turbulent flame brush (δ_t) is comparatively thicker than the laminar flame. The laminar flame structure may be

retained depending on the turbulence level in the flow (discussed in detail in section 5). The flame brush can be defined as the combustion zone with burnt and unburnt gas as boundaries. The various flame geometries commonly used in premixed turbulent combustion can be classified based on the turbulent flame brush into two major categories, namely, (a) developing or growing flame brush, and (b) fully developed flame brush [5]. Bunsen burner, v-flame, and fan-stirred bombs fall into the first category, while twin counter-flows, stagnation flows, and low-swirl flames belong to the latter (see Fig. 1).

For the Bunsen flame, a fluctuating flame with a spatially varying flame brush is stabilized at the burner rim. The thickness of the flame brush increases with distance from the flame holder. A v-flame is established by placing a rod at the center of the burner exit. This results in an inverted conical v-flame stabilized by recirculation zones behind the rod. The flame brush thickness increases in the axial direction away from the burner for the v-flame as well. In the case of a fan-stirred bomb, the brush thickness grows (temporally) as the flame expands spherically outwards. The growth of the turbulent flame brush is attributed to the random advection of the flame surface by turbulent eddies [5]. In such a framework, the growth of the flame brush is similar to the growth of the mixing layer which is governed by Taylor's law of turbulent diffusion. Subsequently, the growth of brush thickness can be modeled as [11],

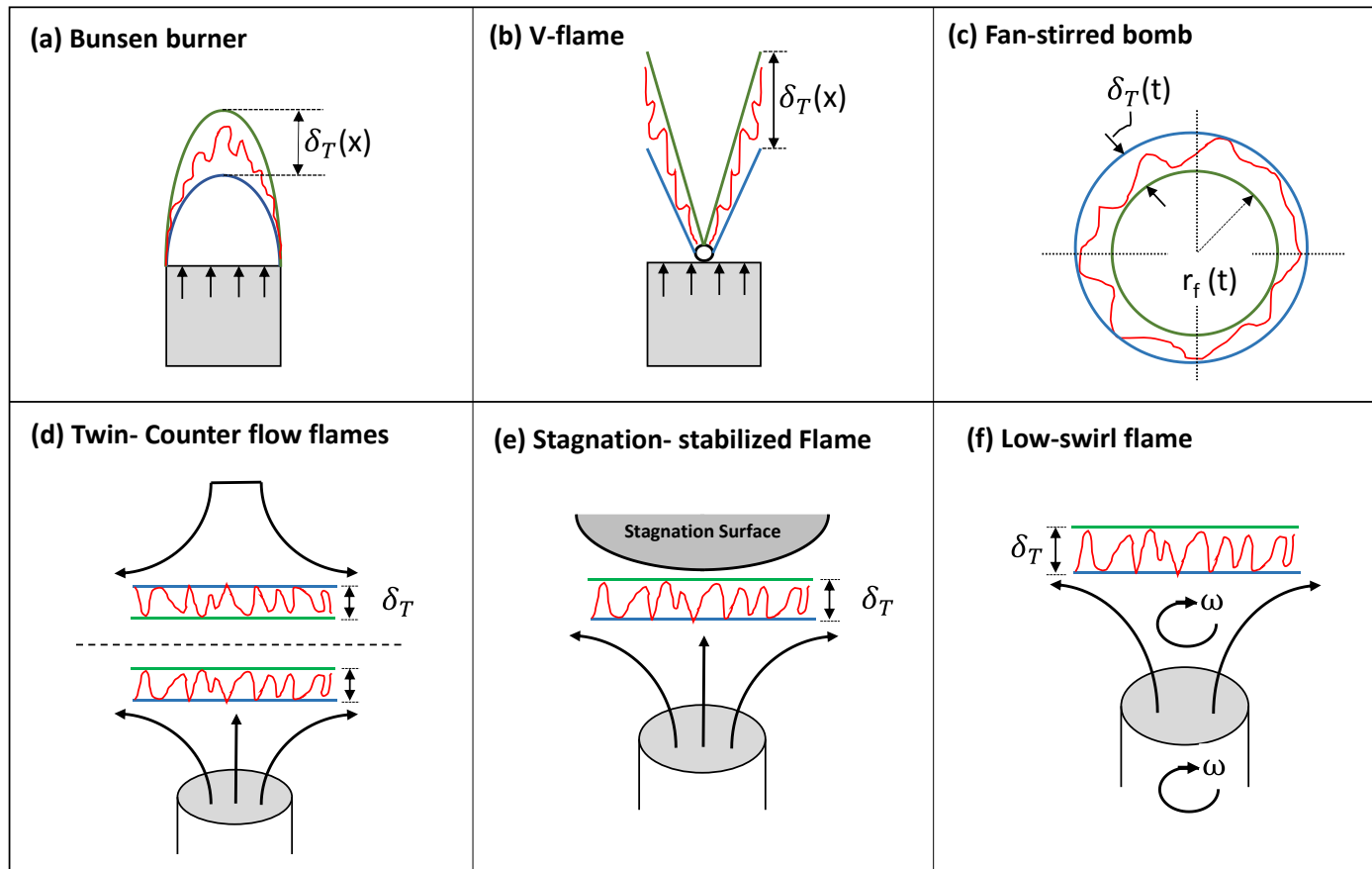


Figure 1. Turbulent flame brush thickness. Developing flame brush (brush thickness varies spatially or temporally) - (a) Bunsen burner (b) v-flame (c) fan-stirred bomb. Fully developed flame brush (characterized by constant brush thickness) (d) stagnation flow burner (e) low-swirl burner.

$$\delta_t = \sqrt{2\pi} L'_0 \left\{ 2t' \left[1 - \frac{1}{t'} (1 - e^{-t'}) \right] \right\}^{0.5} \quad (1)$$

Where,

$$L'_0 = L_T / (1 + S_L^0 / 2u') \quad (2)$$

$$\tau'_T = L'_0 / u' \text{ and } t' = t / \tau'_T \quad (3)$$

Statistically stationary flame brushes can also be achieved in premixed turbulent combustion. For twin-counterflow, stagnation, and low-swirl flames, the mean brush thickness is constant after the initial ignition-transient. Nevertheless, the principle governing the brush-growth for these flames is different from the developing flames discussed earlier. Here, for the fully developed brush case, the mean flow is decelerating away from the burner. For example, the velocity fields of a stagnation flame can be modeled as, $u_x = U - a_t x$ and $u_r = a_t r / 2$ for the axial and radial velocities respectively (x is the distance from the burner exit) [5]. The random advection of the flame by turbulent eddies is counter convected by the strong mean flow gradient (a_t - mean strain-rate) as we move away from the stagnation surface. The mean strain-rate then limits the fluctuations of the flame brush. The same principle can be extended to twin-counter flow and low-swirl stabilized flames which are also characterized by divergent mean flows (decelerating from the burner exit). While this class of flames is convenient for determining the properties of fully developed turbulent flames, practical flames (IC engines and gas

turbines) are developing in nature and take significantly longer to become fully developed ($\sim \tau_t S_L^2$) [5].

3. Reaction progress variable

Different surfaces can be identified inside the turbulent flame brush, and each of them can be uniquely identified by using a scalar called the reaction progress variable $\langle c \rangle$ which defines the extent of completion of combustion. It is typically defined as the normalized temperature, density (Eq. 4), or some species fraction (Ex. mass fraction of oxygen). $\langle c \rangle$ varies from 0 (unburnt gas) to 1 (burnt products) within the flame brush.

$$\langle c \rangle = \frac{\bar{T} - T_u}{T_b - T_u} = \frac{\bar{\rho} - \rho_u}{\rho_b - \rho_u} \quad (4)$$

Where, for Eq. 4, \bar{T} and $\bar{\rho}$ are the average temperature and density of the gases up to that surface inside the flame brush.

The reaction progress variable can be estimated for all canonical turbulent flame geometries. For a burner-type apparatus, the intensity variations from flame chemiluminescence are used to identify the various surfaces with the mean flame surface (usually $\langle c \rangle = 0.5$) having the maximum intensity [12]. When using laser-sheet imaging, for example OH-PLIF, wherein the reaction zone of the flame is detected, the instantaneous flame images are binarized into burnt or unburned gas. Ensemble averaging over several images is done at each pixel inside the imaging plane to identify its average $\langle c \rangle$. The locus of pixels with $\langle c \rangle = \text{constant}$ represent the flame surface corresponding to that $\langle c \rangle$ [13]. For stagnation flows, twin counter-flow, and low-swirl burners, the various $\langle c \rangle$ contours are horizontal planes along the axial direction [14]. Figure 2 shows the various $\langle c \rangle$ contours for different flame configurations. It is evident that measured turbulent flame speed is highly dependent on the surface at which it was measured (for example, the cone angles in Fig. 2c decrease significantly with $\langle c \rangle$).

In fan-stirred bombs, the profiles of $\langle c \rangle$ are dependent on the diagnostic technique. Optical techniques such as schlieren imaging and indirect methods, namely, the pressure-trace method are frequently used in fan-stirred bombs. The mean flame surfaces identified by the two techniques have different $\langle c \rangle$. Bradley et al. [1] found that the schlieren edge statistically coincided with a flame surface having an average $\langle c \rangle \approx 0.1$. Also, in the same study, they determined that the $\langle c \rangle = 0.6$ flame surface directly correlated with the radii deduced from the dynamic pressure trace.

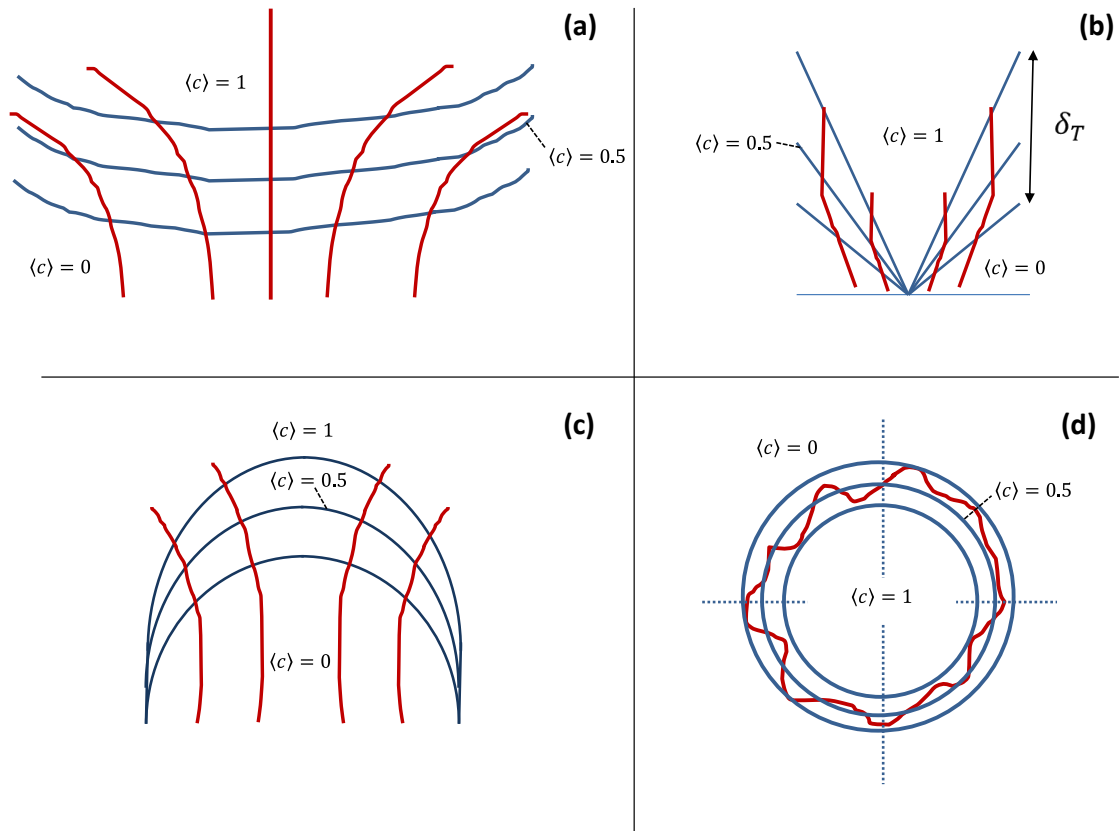


Figure 2. $\langle c \rangle$ Isocontours for various flame configurations- (a) stagnation flow-stabilized burner (b) V-Flame (c) Bunsen burner (d) spherically (statistical) expanding flame. The various isocontours in spherical flames are identified by their corresponding radii.

4. Turbulent propagation rates- definition dependency

Two definitions of turbulent burning rates, namely, global consumption ($U_{T,c}$) and displacement speeds ($S_{T,c}$), are prevalently used in the literature [15]. Global consumption speed is equal to the mass burning rate over a mean flame surface divided by the product of its surface area and the unburned gas density. Displacement speeds (or entrainment

speed or engulfment speeds) can be defined as the difference between the observed wave speed and the velocity of the unburned gas normal to the flame. $U_{T,c}$ is typically estimated at the center of the flame brush characterized by $\langle c \rangle = 0.5$, while $S_{T,c}$ is measured at the leading edge of the flame with $\langle c \rangle \approx 0.05 - 0.1$. When the net consumption (formation) rate of reactants (products) is desired, $U_{T,c}$ can be used. To determine how fast the leading edge of the flame will transverse a certain distance (for example- inside an engine) $S_{T,c}$ is appropriate. It is imperative to note that consumption and displacement speeds should not be directly compared. Only flame speeds within each category can be compared between various flame geometries.

The difference in the two definitions can be demonstrated using the simple case of a planar turbulent flame with a growing flame brush. Different isosurfaces of $\langle c \rangle$ can be identified within the brush with each surface moving at different speeds but having equal areas (A). The difference between the speeds of the surfaces with $\langle c \rangle \rightarrow 0$ and $\langle c \rangle \rightarrow 1$ is proportional to $d\delta_T/dt$ for spherical flames and $U \frac{d\delta_T}{dx}$ for burner flames stabilized at the flame holder (U is the mean flow velocity, and x is the axial distance from the flame holder) [4]. Each surface is then characterized by its own displacement speed. Thus the displacement speed cannot be unambiguously defined for a planar case and varies with $\langle c \rangle$ within the flame brush. The total burning rate over the flame brush, $\frac{d}{dt} \left(\int_{-\infty}^{\infty} \bar{\rho} \langle \widetilde{c} \rangle A dx \right)$, when divided by $\rho_u A$, yields the global consumption speed for the planar turbulent flame

[4]. U_T is independent of $\langle c \rangle$ and is well-defined (single value) for the simple planar geometry.

Real flames encountered in practical applications are nonetheless curved, and are characterized with a growing flame brush. The earlier argument can be invoked to show that a single value of $S_{T,c}$ cannot be uniquely determined for the curved flames. Furthermore, $U_{T,c}$ is also dependent on the isosurface used to estimate it as the areas of the various isosurfaces are different due to flame curvature. The displacement speeds and consumptions differ significantly due to streamline divergence based on the flame geometry [16]. If the streamlines are diverging as in low-swirl burners or fan-stirred bombs, displacement speeds exceed consumption speeds. On the contrary, Bunsen burner flames show the opposite trend due to the negative-stretch configuration (concave towards unburnt gas) [15].

5. Turbulent combustion regime diagram

Damköhler proposed that turbulent flame propagation can be classified into two different regimes, namely, large-scale and small-scale turbulence [17]. In large-scale turbulence, the interaction between the wrinkled flame front and the turbulent flow field is purely kinematic and is independent of length scales. By equating the mass flux of unburnt gas of a wrinkled flame surface burning at the laminar flame speed to that of a mean flame front burning with the turbulent burning velocity, he obtained an expression for the ratio

of turbulent to laminar burning velocities in terms of the turbulent intensity u' and S_L (Eq. 5 [18]- with $n, C = 1$). In the small-scale regime, he showed that this ratio is proportional to the ratio of turbulent to molecular diffusivities (Eq. 6) as turbulence modified the reaction zone and the unburnt reactants. It is evident that regardless of the regime of turbulence, the turbulent burning velocity is always higher than the laminar flame speed.

For large-scale turbulence,
$$\frac{s_T}{s_L} = \left(1 + C \left(\frac{u'}{s_L} \right)^n \right)^{1/n} \quad (5)$$

For small-scale turbulence,
$$\frac{s_T}{s_L} = \left(\frac{D_t}{D} \right)^{1/2} = \left(\frac{u' L_T}{s_L \delta} \right)^{1/2} \quad (6)$$

Where, L_T and δ are the integral length scale of turbulence and the laminar flame thickness, respectively.

Since the classical Damköhler formulation, several regimes of turbulent combustion have been identified and are classified in the Borghi Diagram (Fig. 3) [19]. Re , Da , and Ka (based on the macroscale dimensions- See Appendix-A for definitions) form the various boundaries of the Borghi diagram, which is a log-log plot of the normalized intensity (u'/S_L) and the normalized turbulence length scale (L_T / δ). The region below $Re_T = 1$ demarcates laminar flame propagation. In the region bounded by $1 < Re_T < 100$, a weak turbulent subregime can be identified where the turbulent field does not follow the classical Kolmogorov-scaling. The various turbulent combustion regimes considered

herein are characterized by $Re \gg 1$. The well-stirred reactor regime corresponds to $Da < 1$ when chemical timescales are longer than the turbulent time scales.

The flamelet mode of turbulent flame propagation is present for $Ka < 1$ and $Da > 1$. In the flamelet mode, the laminar flame structure consisting of the reaction and the preheat zones are undisturbed, and the flame front propagates as laminar flame segments wrinkled by the superimposed turbulent field. In the flamelet regime, the smallest eddy present in the turbulent flow is larger than the laminar flame thickness, and the increase in turbulent burning rate is controlled by two competing processes, namely, creation of flame surface area through wrinkling by turbulent eddies, and the destruction of flame surface area by self-propagation of the leading edge of the flame brush, with the former dominating over the latter [5]. The flamelet mode can be subdivided into the wrinkled and corrugated flamelet regimes (weak- and moderate- turbulence respectively), and $u'/S_L = 1$ separates the two regimes. $Ka=1$ (Klimov-Williams limit) demarcates the flamelet from the distributed-reaction-zone regime ($Ka > 1$ and $Da > 1$) of turbulent combustion.

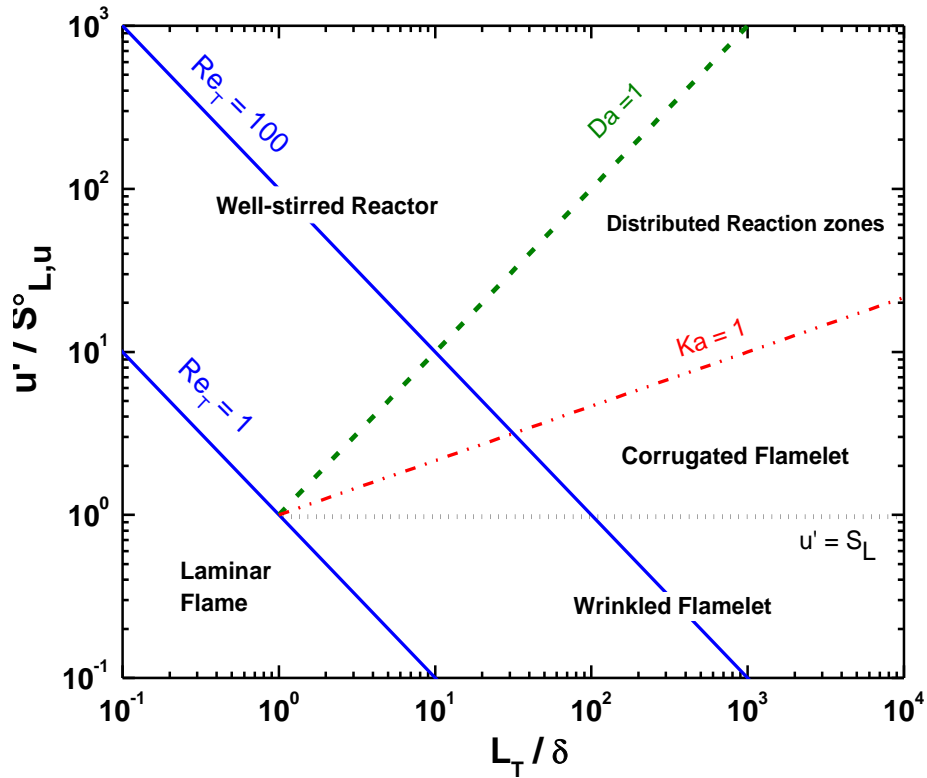


Figure 3. Classical turbulent combustion regime diagram (Borghi diagram).

Peters [17] modified the classical Borghi diagram based on the Karlovitz number, and identified the thin-reaction zones ($1 < Ka < 100$; when $Ka=100$, $Ka_{\delta} = 1$ where $Ka_{\delta} = \delta^2 Ka$; $\delta=0.1$ (laminar flame thickness) for most hydrocarbon flames) wherein the size of the smallest eddy is smaller than the preheat zone thickness and can penetrate into it, thus augmenting heat and mass transfer (radical transport) (see Fig. 4). Nevertheless, the reaction zone thickness is unaffected as it is still smaller than the smallest eddy in the turbulent flow. Broken-reaction-zones or thickened-flames are present for $Ka \geq 100$ with eddies penetrating into both preheat and the reaction zones, and the laminar flame structure is completely disrupted. Greater heat loss to the preheat zone results in temperature

decrease followed by loss of radicals due to broken chemistry, eventually leading to extinction in the broken reaction zone. Recent DNS data [20] showed that a correction to account for gas expansion (density ratio: $\sigma = \rho_u/\rho_b$) was still necessary to the Peters limit (modified Ka, $Ka' = \sigma^{-1.5}Ka$), and that Ka' predicted the transition to the broken reaction zones better and was consistent with DNS predictions.

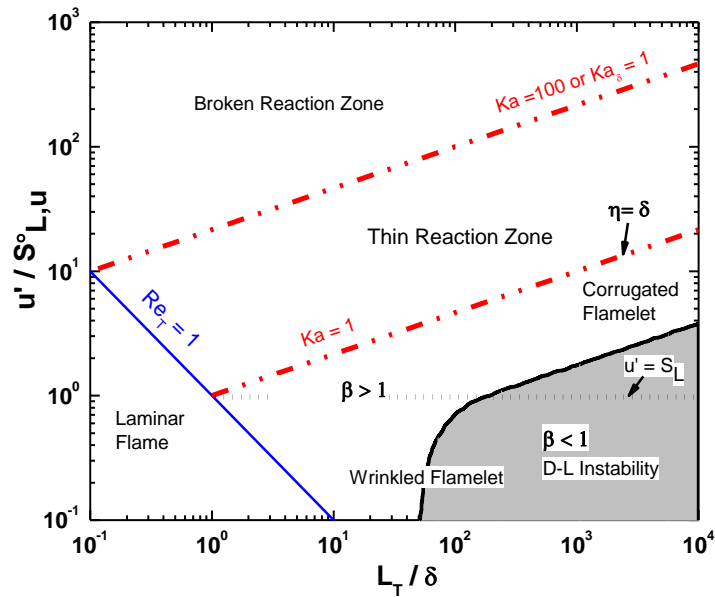


Figure 4. Modified Borghi diagram as described by Peters [17] showing the thin-reaction zone. Darrius-Landau (hydrodynamic instability) instability affected regime [22] is also shown.

Furthermore, mixing length- and time-scales can be derived to better understand the flame-turbulence interaction in the corrugated flamelet and thin reaction zone regimes [21]. In the corrugated flamelet regime, the interaction between the flame and the turbulent eddies is purely kinematic. Thus for $Re \gg 1$ and $Ka < 1$, the size of the eddy that will

affect the advancing flame front must have a velocity equal to the local laminar flame speed, S_L . Thus, the Gibson length scale can be defined as (ε is the turbulent kinetic energy dissipation rate),

$$l_G = S_L^3 / \varepsilon \quad (7)$$

Eddies larger than l_G simply wrinkle the flame front as if it were a passive surface, while smaller eddies cannot wrinkle the flame front as their actions are masked by eddies of size l_G . When S_L is equal to the macro-turbulent intensity level, then the $l_G = L_T$ and forms the boundary between the wrinkled and the corrugated regimes. This condition is called the lower cut-off scale of the scalar spectrum function. When S_L is equal to the Kolmogorov velocity, Gibson and Kolmogorov scales are identical (stronger diffusive cut-off: Obukhov-Corrsin scale).

In the thin reaction zone, $l_G < \eta$ and η is greater than the preheat zone thickness of the flame. Thus an appropriate mixing length-scale based on the chemical time-scale of the flame (time required to transport over the preheat zone thickness) can be defined as,

$$l_m = (\varepsilon \tau_c)^{1/2} \quad (8)$$

Eddies with $l < l_m$ will also be able to transport preheated material to the flame, but their actions are masked by eddies having size of l_m . Larger eddies ($l < l_m$) will only wrinkle the broadened flame structure.

Recently, Chaudhuri et al. [22] proposed a boundary for the growth of Darrius-Landau (D-L) instability in the presence of turbulence. D-L instability caused by the thermal expansion (density jump) across the flame is suppressed when the integral length scale of turbulence is less than a cut-off wavelength, $\lambda_c \approx 20 \delta$, for the case of a flame with finite thickness. The instability leads to corrugated (wrinkled) flames for intermediate scales, $\lambda_c < L_T < 4\lambda_c$, and fractal-like, self-similar structures for large wavelengths $L_T \geq 4\lambda_c$. They defined a stability parameter, β , that can be used to demarcate the region affected by D-L instability on a Borghi diagram (Fig. 4- Eq. 9). For $\beta > 1$, the instability is suppressed in the presence of turbulence. The D-L instability affected region is shown in the Borghi diagram in Fig. 4. They concluded that D-L instability persisted only at low-levels of turbulence ($u' \approx S_L$).

$$\beta = \begin{cases} \frac{u'}{X S_L} \left(1 - \frac{\lambda_c}{L_T}\right)^{-1} ; & \lambda_c < L_T < 4\lambda_c \\ \frac{4^{4/3} u'}{3X S_L} \left(\frac{\lambda_c}{L_T}\right)^{1/3} & ; \quad L_T \geq 4\lambda_c \end{cases} \quad (9)$$

Where, $X(\sigma) = \frac{\sigma}{\sigma+1} [(\sigma + 1 - \sigma^{-1})^{1/2} - 1]$; $\sigma = \frac{\rho_u}{\rho_b}$. Typically, $X=1.25-1.75$ for $\sigma = 5 - 8$.

Similar to the classical Borghi diagram, spectral regime diagrams are also used (flame-vortex interaction), where the vortex speed and size form the relevant turbulent scales. Regime diagrams for large eddy simulations (LES) with the subfilter size and corresponding subfilter velocity fluctuations can also be constructed [23].

6. Summary

The various terminologies used in premixed turbulent combustion that are relevant to this study were discussed in detail. As a flame is wrinkled by eddies in a turbulent flow, it results in a thick zone characterized with density fluctuations and heat-release based on the concentration of the unburnt gas. Such thick zones are characteristic of premixed turbulent combustion and are referred to as the turbulent flame brush. The various geometrical configurations of premixed turbulent combustion were categorized into growing and fully developed flame brushes. Bunsen burner, V-flame, and spherically expanding flames showed varying brush thickness. The brush thickness broadened in the axial direction away from the burner exit for Bunsen burner and V-flames (spatially varying), and increased as the flame expanded for fan-stirred bombs (temporally varying). Flow deceleration away from the burner exit in twin-counterflow, stagnation flow, and low-swirl-stabilized burners allowed the brush to adjust to flow perturbations resulting in near-constant thickness or fully developed flame brush. Also, the increase in flame brush thickness can be modeled using Taylor's law of diffusion, and that flames inside practical

combustion systems such as gas turbines and internal-combustion engines are also characterized by developing flame brush.

Various flame surfaces inside the flame brush were identified using the reaction progress variable whose value varied from 0 (for reactants) to 1 (products). The propagation rates varied based on the choice of the reaction progress variable for all geometries. In fan-stirred bombs, the reaction progress variables ($\langle c \rangle$) were defined at different radii within the flame brush and their associated flame surfaces grew at different rates. Two most commonly used diagnostic techniques in fan-stirred bombs, namely, schlieren imaging and pressure-trace method had $\langle c \rangle$ of 0.1 and 0.6 respectively.

Two definitions of turbulent burning rates were explained in detail. Global consumption speeds related to the rate of production of burnt gases, while global displacement speeds referred to the rate at which a turbulent flame front propagated into an unburnt mixture. Streamline divergence resulted in difference between the two rates. While consumption speeds can be unambiguously defined for planar turbulent flames, neither propagation rate is well-defined for curved flames. Also, within each category, the rates varied based on the choice of the flame surface (reaction progress variable).

Finally, the classical turbulent combustion regime diagram (Borghi diagram) was discussed. The flamelet mode wherein the laminar flame structure is unperturbed, and the thin reaction zone regime wherein turbulent eddies penetrate into the preheat zone and

alter radical transport were identified. The boundaries separating the wrinkled and corrugated flamelets, thin reaction zones, and well-stirred reaction regimes were defined using the non-dimensional parameters, namely, Reynolds, Damköhler, and Karlovitz numbers. Laminar-flamelet instability (Darrius-Landau) persisted only at low-levels of turbulence ($u' \leq S_L$), and the instability-affected region was also shown on the Borghi diagram.

CHAPTER III

FAN-STIRRED BOMBS

Fan-stirred bombs are identified as one of the categories of premixed turbulent flame geometry. Such vessels provide a convenient method to measure flame propagation rates under turbulent conditions. A wide range of intensity levels can be achieved, and the intensity variations are well-controlled. This feature is especially advantageous when compared to a burner-type setup due to the fact that the latter requires a corresponding increase in axial flow rate to increase the turbulence intensity levels. At high flow rates, stabilizing mechanisms such as a pilot flame, recirculation zones, or bluff body may be required to prevent flame blow-out. Also, the minimum intensity levels in burners are dictated by the laminar flame speed of the fuel to prevent flashback. Nevertheless, fan-stirred vessels are expensive to build and may not offer the flexibility for laser-based planar measurements such as burners.

This chapter discusses the major issues associated with fan-stirred bombs, and is organized as follows. First, the diagnostic techniques used in fan-stirred vessels are reviewed in detail. Various dependencies of turbulent flame speeds (definition, technique and geometric) are then discussed. Turbulent kernels in fan-stirred bombs are accelerating by nature, and fan-stirred bombs provide flame speeds over a wide range of intensities in a single experiment. This phenomenon of turbulent flame-acceleration is elaborated in detail.

1. Measurement techniques

This section provides a critical overview of the various diagnostic techniques used in fan-stirred bombs. Schlieren imaging is used extensively for laminar flame speed measurements and can also be used for turbulent combustion studies. For the laminar case, a spherical flame propagates outwards after ignition (although at large flame radii, $r_{sch}/r_{wall} > 0.4$, wall-effects induced anisotropy results in deviation from near-sphericity [24]). Thus the flame propagation can predominantly be assumed to be one-dimensional, and the schlieren technique, despite being an integrated line-of-sight method can be conveniently applied to such a geometric configuration. In the case of a turbulent flame, flame wrinkling is highly anisotropic even in a well-controlled environment (near-HIT conditions) as in a fan-stirred vessel. As a result, the propagation speeds in the radial (in-plane) and axial (out-of-plane) directions for any planar slice of the kernel are not the same. Nevertheless, it was shown by Bradley et al. [15] that the average radius estimated based on the kernel area inside the schlieren silhouette statistically agreed with a flame contour with a reaction progress variable, $\langle c \rangle \approx 0.1$. This value is consistent with an earlier investigation from the same group wherein they showed that the isotherm corresponding to the schlieren radius was close to the unburned gas temperature [10].

The second most common diagnostic technique used in constant-volume flame bombs is the use of high-frequency, dynamic pressure traces. Such a technique is inexpensive and does not require any optical access ports. In constant-volume bombs, there is a constant-pressure period followed by isentropic compression of the unburnt gas ahead of the flame

which results in a pressure rise. Furthermore, significant pressure rise is not seen until the flame has grown to a large diameter. Three major difficulties arise from such a setup. First, the spherical shape of the flame cannot be maintained at large radii due to chamber-confinement effects. Second, the turbulent conditions may no longer be uniform at large flame radii (closer to the fans). Third, the unburned gas is isentropically compressed resulting in a subsequent increase in pressure and temperature. Thus the pressure trace does not yield flame speeds at the initial, unburnt premixture conditions. Furthermore, lack of flame visualization makes pressure-based techniques unattractive.

2D (planar), single-sheet laser imaging techniques are also used to determine the instantaneous flame surfaces for burning velocity measurements. Nevertheless, there are several drawbacks associated with them. First, the main assumption that the in-plane propagation rates are the same as the out-of-plane rates is questionable for turbulent flames. Furthermore, the ignition spark may be randomly convected from the vessel center by large eddies, which subsequently results in kernel displacement away from the imaging plane. As a result, the exact location of the laser sheet relative to the kernel-center cannot be accurately predicted. Harker et al. [25] conducted 3D flame surface measurements using a rotating mirror setup in a fan-stirred bomb. In that study, six laser sheets were swept through the kernel volume to determine its instantaneous shape. However, such simultaneous imaging techniques require the sheet transverse speed to be faster than the flame propagation rates. This requirement limits its applicability to fuels characterized with faster burning rates (high-hydrogen-content fuels) that are of topical interest to gas

turbine manufacturers. Furthermore, variations in the estimated flame diameters were as high as 23% for that study despite the advanced diagnostics employed. This shot-to-shot or cyclic variability explains the significant scatter associated with the measurements.

Laser-sheet techniques are very attractive as they help understand the flame front characteristics such as its curvature and fractal-cutoff scales. However, they are extremely cost-prohibitive (require multiple optical access ports and related instrumentation-cameras, lasers, etc.) when compared to the schlieren technique. Given the experimental scatter associated with fan-stirred bombs (and turbulent flame propagation in general), schlieren photography provides flame propagation rates with similar accuracy as any laser-based technique. Hence schlieren photography was chosen for this study.

2. Dependencies of turbulent flame speeds

As discussed in chapter II, two different burning rates can be determined from fan-stirred bombs. Displacement speeds ($S_{T,\langle c \rangle}$) correspond to a propagation rate of the flame front into an unburnt mixture. Such a rate is typically associated with the leading edge of the flame brush. Consumption speeds ($u_{T,\langle c \rangle}$) provide a rate at which reactants are consumed (rate of generation of products) and is typically measured at center of the flame brush corresponding to a mean flame surface with $\langle c \rangle = 0.5$.

Three major difficulties impede the development of a unified database of turbulent flame speeds from fan-stirred bombs. First, a lack of understanding of the two definitions of

burning rates (*definition dependency*) may result in displacement speeds being misconstrued for consumption speeds (and vice versa). Second, the burning rates within each category vary significantly based on the mean flame surface determined by the diagnostic technique used (*technique dependency*). Finally, geometric factors (turbulent length scale dependence) also affect the measured burning rates (*rig dependency*). These factors discussed so far should not be confused with the scatter associated with turbulent burning rates. The data scatter is due to the *shot-to-shot* or *cyclic variability* [25] discussed earlier. Nevertheless, addressing the three major dependencies will certainly lead to a better understanding of the burning characteristics (trends) of various fuels under turbulent conditions.

Use of advanced laser-sheet diagnostics enabled systematic analysis of various databases of turbulent flame speed (mostly from fan-stirred bombs). Bradley et al. [1] used laser Mie-scattering of tobacco smoke in fan-stirred explosions to identify the various flame surfaces of methane- and propane-air flames over a wide range of turbulent conditions. The radii corresponding to different reaction progress variables were determined based on the proportion of the circumference (at a particular radius) occupied by unburnt and burnt gases. Schlieren images were captured simultaneously. The schlieren radius estimated based on the area of the circle having an equivalent area as the schlieren flame silhouette correlated with a mean flame surface having $\langle c \rangle = 0.1$. This result is consistent with the fact that the schlieren flame edge would be expected to be closer to the leading edge of the flame brush (where the density gradient is the largest). Furthermore, they identified a

spherical volume wherein the volume of burned gas inside it was equal to the volume of unburned gas outside it. Such a radius had a value of $\langle c \rangle \approx 0.34$. Additionally, the consumption and displacement speeds were equal at that radius and can be correlated with the schlieren radius (Eq. 10-11). This finding has significant impact in correlating data from various rigs and allows conversion between the burning rate definitions, thus eliminating definition dependency. Hence,

$$u_{T,0.34} = (\rho_b/\rho_u) \frac{dr_{0.34}}{dt} = S_{T,0.34} = \left(\frac{1}{1.11}\right) S_{T,0.1} \quad (10)$$

Where,

$$S_{T,0.1} = (\rho_b/\rho_u) \frac{dr_{sch}}{dt} \quad (11)$$

The consumption speeds at various flame surfaces inside the flame brush can be related through mass conservation relations [15], thereby eliminating the technique dependency of turbulent flame speeds.

$$\frac{u_{T,c2}}{u_{T,c1}} = \left(\frac{r_{\bar{c}_1}}{r_{\bar{c}_2}}\right)^2 \quad (12)$$

Table 1 shows various radius ratios for the various flame surfaces relative to the mean flame surface with $\langle c \rangle = 0.5$. Thus the consumption speeds at points inside the flame brush can be estimated from the measured schlieren radius history using Eqs. 10-12 as,

$$u_{T,c} = u_{T,0.34} \left[\left(\frac{r_c}{r_{0.5}} \right) \left(\frac{r_{0.5}}{r_{0.34}} \right) \right]^{-2} = \left(\frac{1}{1.11} \right) \left[(\rho_b / \rho_u) \frac{dr_{sch}}{dt} \right] \left[\left(\frac{r_c}{r_{0.5}} \right) \left(\frac{r_{0.5}}{r_{0.34}} \right) \right]^{-2} \quad (13)$$

Table 1. Radii and burning velocity ratios of different measurement surfaces with respect to the schlieren surface as measured by Bradley et al. [15].

Measurement Technique	$\langle c \rangle$	$r_{\langle c \rangle} / r_{0.5}$
OH PLIF	0.05	1.44
Schlieren	0.1	1.34
Equal Volume Method	0.34	1.1
Equal Area Method	0.4	1.05
Mean Flame (Cone angle method)	0.5	1
Pressure Trace/ Mass rate of burning	0.6	0.95

3. Acceleration of spherical turbulent kernels

The flame speeds of statistically spherical turbulent flames increase as they expand. Several physical mechanisms explaining this accelerating behavior are proposed in the literature. Ashurst [26] claimed that the gas expansion occurring at the flame front can be a source of flame acceleration. DNS studies [27] have shown that integral-scale eddies are strong enough to suppress the gas-dynamic instabilities induced by thermal expansion at the smaller scales. It was concluded that the effect of thermal expansion on the turbulent burning velocity was minimal even at low-intensity levels ($u' < S_L$). Leisenheimer and

Leukel [28] attributed such accelerations to the flame-generated turbulence. They suggested that the effective intensity level experienced by the flame is the combined effect of fan-generated and combustion-induced turbulence. Nevertheless, the study was validated over a narrow range of experimental conditions, and so the proposed mechanism cannot be generalized.

The Leeds group ([29], [30]) proposed a developing spectrum theory to explain the accelerating nature of turbulent flames. In this framework, there is a size restriction on the eddy that can wrinkle the flame front, and the developing kernel is not perturbed by the entire spectrum of eddies (all eddy sizes). Only eddies smaller than the flame (diameter) wrinkle it, while larger eddies simply convect the flame front like a passive surface. They derived an effective turbulent intensity level experienced by the expanding flame by integrating the non-dimensional spectral density function (Eq. 14) between the wavenumbers corresponding to the flame diameter (lower wavenumber cutoff) and the Gibson scale (higher cutoff) (Eq. 15). This formulation is widely accepted in the literature and will be used in processing results measured as a part of this study.

A correlation was developed [30] to model the universal, non-dimensional power spectral density (scaled based on the Kolmogorov scale) and is given as,

$$\bar{S}(\overline{k_\eta}) = \frac{0.01668R_\lambda^{2.5} + 3.74R_\lambda^{0.9} - 70R_\lambda^{-0.1}}{1 + (0.127R_\lambda^{1.5}\overline{k_\eta})^{5/3} + (1.15R_\lambda^{0.622}\overline{k_\eta})^4 + (1.27R_\lambda^{0.357}\overline{k_\eta})^7} \quad (14)$$

where,

R_λ is the Taylor-scale-based Reynolds number that can be estimated from the turbulent Reynolds number (based on L_T) using $R_\lambda = 4Re_T^{0.5}$

\overline{k}_η is the dimensionless wavenumber obtained by multiplying $2\pi/\text{wavelength}$ with the Kolmogorov length scale, η .

The non-dimensional spectra at various R_λ are shown in Fig. 5. The universal $5/3$ decay slope in the inertial subrange is evident at higher R_λ . Furthermore, the separation of scales broadens (extension of the inertial subrange) with increase in Reynolds number and is consistent with Kolmogorov's second hypothesis (see Appendix-A). According to that hypothesis, with Reynolds number increase, intermediate scales appear in the range separating the large-scale, energy-containing eddies and the small-scale, dissipative eddies. Since the spectra are scaled with respect to the Kolmogorov scale, the inertial subrange extends to large scales (lower wavenumbers) as the Reynolds number is increased.

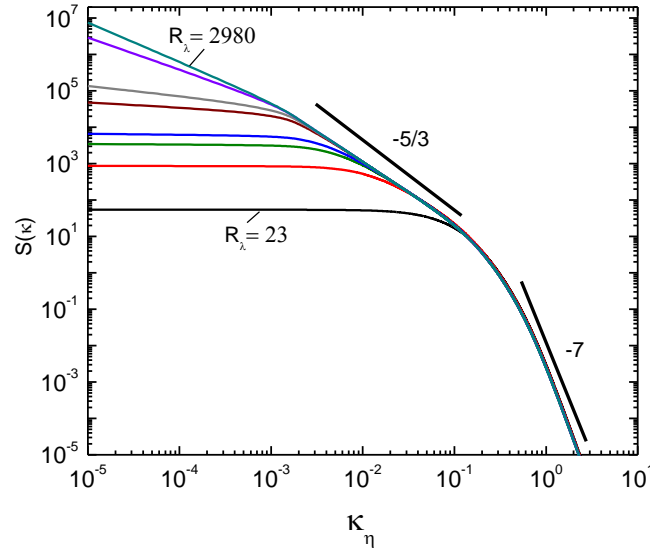


Figure 5. Non-dimensional power spectral density function normalized by the Kolmogorov scale. Curves are correlation predictions (Eq. 14) at various Taylor Reynolds number. The characteristics slopes namely, $-5/3$ and -7 are evident in the inertial subrange and dissipation range of the kinetic energy spectra.

The effective turbulence intensity (u'_k) acting on the flame can then be obtained as,

$$\frac{u'_k}{u'} = \left[\frac{\sqrt{15}}{R_\lambda} \int_{\overline{k_{\eta 1}}}^{\overline{k_{\eta 2}}} \overline{S(k_\eta)} d\overline{k_\eta} \right]^{0.5} \quad (15)$$

where,

$\overline{k_{\eta 1}}$ – is the lower cutoff wavenumber based on the flame diameter

$\overline{k_{\eta 2}}$ – is the upper cutoff wavenumber based on the Gibson scale

A general wavenumber for (length scale k) can be defined as,

$$\overline{k_{\eta k}} = \frac{2\pi}{n_k L_T} \quad (16)$$

With,

$$n_1 = \frac{2r_{sch}}{L_T}; \quad n_2 = n_G = 0.133 \left(\frac{u'}{S_{L,u}} \right)^{-3} \quad (17)$$

Figure 6 shows the variations in u'_k for stoichiometric ethane-air obtained using the present facility. The flame experiences progressively increasing intensity levels as it propagates outwards. It should be noted that the flame may not attain the full spectrum of turbulent intensity ($u' \sim 1.5$ m/s) during the usable part of the experiment (when the flame grows to the viewing window size- 12.7 cm diameter). Experimentally measured flame radii are related to the effective intensity levels by cubic-spline interpolation, and are also included in Fig. 6. Similar trends were obtained for all mixtures from this study.

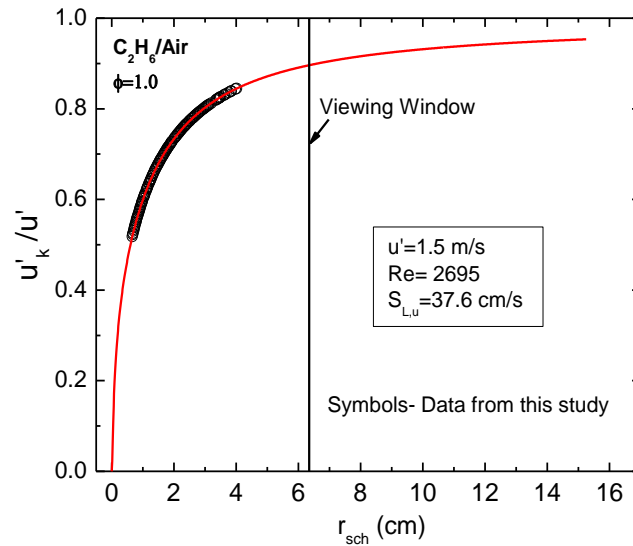


Figure.6. Effective turbulent intensity (Eq. 15) seen by the flame (u'_k) normalized by the fan-generated intensity level ($u' \sim 1.5$ m/s) for a stoichiometric ethane-air mixture (shown as the curve). The intensity levels at various flame radii (measured herein) are estimated using cubic-spline interpolation (shown as symbols).

4. Self-similar scaling of turbulent flames

Chaudhuri et al. [2] proposed a different mechanism for turbulent flame acceleration based on the integration of the global average flame dissipation rate (terms inside the integral in Eq. 18). The smallest wavenumber decreases due to turbulent stretching as the flame expands (or increase in largest flame relevant scale- i.e., flame radius). This phenomenon increases the area under the flame surface dissipation spectrum (Fig. 7) resulting in increasing turbulent flame speeds (Eq. 18) as the flame grows. Furthermore, with increase in pressure, the flame thickness reduces (small-scale effect) and leads to extension of the spectrum to higher wavenumbers. Higher wavenumbers (smaller scales) are now accessible for turbulent wrinkling. Such a behavior explains an increase in turbulent flame speed with increase in system pressure contrary to laminar flames whose propagation rates typically decrease with pressure.

$$S_T/S_L \sim [1 + \int_0^\infty k^2 \Gamma(k) dk]^{1/2} \quad (18)$$

Subsequently they showed that a spherically expanding flame showed self-similar behavior, and its radius growth scaled as $Re_{\langle R \rangle}^{0.5}$ (Eq. 19, where $Re_{\langle R \rangle}$ is the Reynolds number based on the flame radius). They found that the experimentally measured data collapsed well with an exponent close to 0.54 for methane/air mixture ($\phi = 0.9$; $Le \sim 1$). The proposed scaling was tested with the measurements from this study for the same mixture and a power-law exponent close to 0.56 ± 0.08 was obtained (Fig. 8).

Nevertheless, such a scaling is valid only for fuel-air mixtures with positive Markstein length, and its applicability to high-hydrogen-content fuels (HHC) that are of topical interest to gas-turbine manufacturers and DoE is limited. This limited applicability to HHC fuels is primarily due to the fact that flame surface area increase is affected not only by the turbulent eddies (stretching and wrinkling) but also by thermo-diffusive instabilities for lean HHC fuels (negative Markstein lengths).

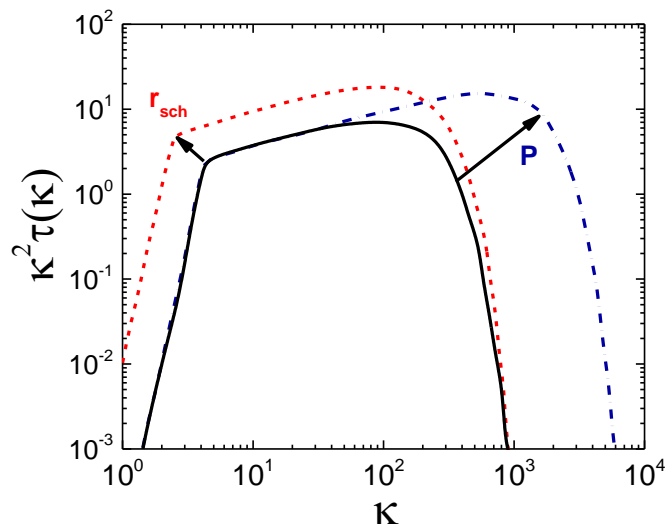


Figure.7. Flame surface dissipation spectrum as described by Chaudhuri et al. [2]. The area inside the spectrum is directly proportional to the ratio of turbulent to laminar flame speed. As the flame grows, the largest scale (smallest wavenumber) increases (decreases) and leads to an increase in turbulent flame speeds, further providing evidence for flame acceleration commonly observed in spherically expanding turbulent kernels. An increase in system pressure extends the spectrum to higher wavenumbers (reduction in smaller scales- flame thickness) which results in higher turbulent flame speed at elevated pressures.

$$(S_{L,b})^{-1} d\langle R \rangle / dt = O(1) Re_{\langle R \rangle}^{0.5} = O(1) [(u' / S_{L,u}) (\langle R \rangle / \delta_L)]^{1/2} \quad (19)$$

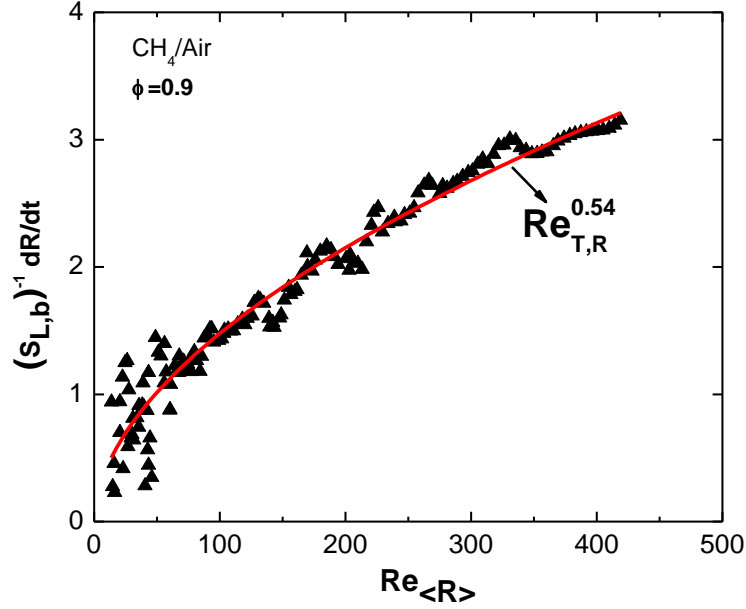


Figure 8. Self-similar scaling for methane-air mixture at $\phi= 0.9$. A power-law exponent close to 0.54 was obtained (shown as curve) as a function of the flame-radius based Reynolds number, and is in good agreement with Chaudhuri et al. [2]. Symbols are measurements from this study.

5. Summary

Four major issues associated with fan-stirred bombs were discussed. First, the various measurement techniques were reviewed. Schlieren imaging offers a convenient and cost-effective method to image turbulent kernels. Pressure-based techniques are affected by chamber-confinement effects and non-uniform turbulent flows. Single-sheet laser measurements do not account for anisotropic out-of-plane propagation of developing

turbulent kernels. Multiple (simultaneous) sheet techniques do not have this limitation, but are often difficult to set up and are not suited for fast-burning mixtures. Schlieren measurements are typically used to provide global displacement speeds of a flame surface near the leading edge of the flame brush. It was shown that various consumption speeds inside the curved flame brush can be estimated from the schlieren radius-growth history.

Three major dependencies of spherically expanding turbulent flames namely, definition-, technique- and rig-dependency were elaborated. Definition dependency is associated with whether the measured burning rate is a consumption speed or a displacement speed. Only propagation rates within each category should be compared. The measured flame speeds are also dependent on the diagnostic technique adopted to identify the instantaneous flame surface (technique dependency). Rig dependency corresponds to the influence of geometric parameters of the experimental apparatus, such as length scale effects on the measured flame speeds. These difficulties are further compounded by the shot-to-shot or cyclic variability of turbulent kernels which lead to greater data scatter.

The physical mechanisms of turbulent flame acceleration were reviewed. The concept of developing spectrum proposed by Bradley et al. [30] was explained in detail. Within that framework, developing flames are affected by increasing sizes of eddies but with a size-restriction. Only eddies smaller than the flame ball can wrinkle it, while larger eddies simply convect it. Thus the flame may not experience the full spectrum of turbulent intensity generated by the fans. An effective intensity level (u'_k) was estimated by integrating the universal, non-dimensional spectral power density function between the

hydrodynamic scale (flame diameter) and the smallest flame-relevant scale (Gibson's scale). Spline-interpolation was then used to estimate u'_k corresponding to the measured radius for each test mixture studied herein.

Finally, the theory of self-similar scaling of developing turbulent kernels was explained. Spherically expanding turbulent flames with positive Markstein length exhibit self-similar or hierarchical behavior. Subsequently, the radius growth rates (normalized by the burnt, unstretched laminar flame speed) show power-law dependence with flame-radius-based turbulent Reynolds numbers. A power-law exponent of 0.54 was obtained for lean methane-air mixtures ($Le = 1$) and agreed with the theoretically derived value of 0.5.

CHAPTER IV
IMPELLER DESIGN STUDY*

1. Introduction

Speed-controlled impellers were installed inside an existing, high-pressure cylindrical flame speed vessel originally designed for measuring the flame speeds of spherically expanding flames under quiescent (laminar) conditions. A symmetrically opposed placement of impellers induces a turbulent flow field without a mean velocity. Furthermore, the stochastic nature of turbulence is greatly simplified by creating a homogeneous and isotropic turbulent field (HIT). These flow constraints entail good repeatability of flow conditions over several experiments as well as precise control and quantification of the levels of turbulence. As a first step in the upgrade of the existing infrastructure, it was necessary to arrive at the best impeller design feasible for establishing near-HIT conditions.

To the authors' knowledge, no study exists in the literature that provides guidelines for such impeller designs used to achieve HIT conditions inside a confined volume. So, presented in this chapter is an experimental study to assess the impact of impeller geometry on the turbulent flow field inside the closed cylinder.

*Reprinted with permission from "Analysis of the Impact of Impeller Geometry On The Turbulent Statistics Inside A Fan-Stirred Cylindrical Flame Speed Vessel using PIV" by S. Ravi, S.J. Peltier, E.L. Petersen, 2013. *Exp. Fluids*, 54, 1424-1440, Copyright 2013 by Springer-Verlag, Berlin.

The flow field characterization results of three different impeller prototypes are discussed herein, and the chapter is organized as follows. First, a survey of HIT studies reported in the literature is conducted. The impeller design methodology and the experimental setup are then explained. For each impeller, all relevant turbulence statistics are estimated from their measured velocity data. Using these results, the design of the turbulent flame speed vessel with the capability to control the turbulent parameters is discussed.

2. Background literature

a. HIT inside a confined volume

HIT with no mean flow inside a confined volume is a subject of active research in both experimental [31] and computational [32] fields. While perfectly isotropic turbulence represents an ideal case, nonetheless, close approximations can be achieved at the laboratory scale. The properties of such flow fields include: negligible mean flow ($< 10\%$ RMS); near-Gaussian velocity probability density functions (PDFs); spatial uniformity or homogeneity of velocity and equality or isotropy of its components; near-zero Reynolds shear stresses; and the characteristic $5/3$ decay slope of the energy spectrum in the inertial subrange at high enough Reynolds Numbers. Though challenging to achieve experimentally, the simplification HIT yields makes it convenient to study a variety of complex phenomena such as particle modulation of turbulence ([33], [34]), droplet evaporation in isotropic turbulence [35], HIT decay theories [31] and turbulent

combustion [15]. For brevity, we restrict this background survey to two experimental studies on box-type HIT that are supported by substantial characterization results.

Birouk et al. [37] demonstrated HIT in air inside a spherical region at the center of a 40-cm cubic aluminum chamber with eight speed-controlled fans mounted at each corner of the box. The facility was designed to study low Reynolds Number flows (based on RMS turbulent intensity u' and Taylor microscale λ), $45 \leq Re_\lambda \leq 92$. They had employed two-component laser Doppler anemometry (LDA) to measure the two orthogonal velocities at 17 discrete locations spanning a 20-mm radius in the midplane of the box. A linear increase in u' with fan speeds was observed, and turbulent kinetic energies between 0.1 and $1.45 \text{ m}^2/\text{s}^2$ were achieved. The instantaneous velocity PDFs exhibited zero skewness and a kurtosis of three at all fan speeds, further indicative of Gaussian velocity PDFs. The spatial uniformities and directional equalities of the velocity fields were assessed by computing the homogeneity and isotropy ratios, respectively. Both remained within $\pm 5\%$ of the ideal value of unity for perfectly HIT conditions. The integral time scale (or temporal integral scale), τ , was obtained from the Eulerian autocorrelation coefficients of velocity and decayed as $12q^{-0.5}$ with increasing fan speeds. The integral length scale was found by integrating the lateral spatial correlation coefficient curve (8.6 mm), which remained independent of fan speed. The inertial subrange with a $-5/3$ decay exponent as prescribed by the Kolmogorov theory was not observed for any of the power spectra in the Re_λ range that were attained.

Hwang and Eaton [31] had developed a similar Plexiglas chamber to study particle modulation in HIT conditions under microgravity. The chamber was designed with no moving parts, and the fans were replaced with eight synthetic, pulsed-jet actuation systems which were forced at precisely controlled rates. The actuator consisted of a cone woofer used in combination with an ejector tube fitted with galvanized steel, woven-wire cloth at the end. The woofers directed the jets towards the center of the chamber, and produced a ϕ 40-mm spherical region with fairly HIT conditions, characterized using 2D digital particle image velocimetry (PIV). The out-of-plane component of velocity was measured separately using LDA and was found to be within 2% of the in-plane components. The study was conducted at only one condition at $u' \approx 0.85$ m/s ($Re_\lambda = 218$) with mean velocities within $\pm 0.1u'$. Spatial maps of isotropy and homogeneity ratios inside a 40×40 mm² area in the chamber midplane were generated. The isotropy ratios varied between 0.88 and 1.24, and the homogeneity ratios in the two directions remained within $\pm 10\%$ of their corresponding spatially averaged values. A large eddy simulation (LES) analogy was used to estimate the turbulent kinetic energy dissipation rate, and subsequently other turbulence statistics (Euler, Taylor, and Kolmogorov scales). Large spatial variations in the various scales were observed due to errors in estimating the velocity derivatives. This yielded an approximate integral length scale of 56 mm with a spatial variation of 66-149%. Also, several properties of isotropic turbulence were further validated using spectral analysis and by two-point velocity correlations in the longitudinal and lateral directions for both the measured orthogonal velocities.

These detailed characterization results are encouraging for the present scenario, which also involves HIT generation within a closed cylinder to study turbulent flame speeds. Given the severity of the current application, impellers or mixing fans were deemed to be robust enough to achieve the desired flow conditions inside the flame bomb.

b. Spherically expanding turbulent flames

Measurement of turbulent flame speeds (S_T) inside a fan-stirred vessel was first demonstrated by Semenov [38]. Subsequently, several research groups have developed similar apparatus. The flame kernel is initiated at the center of the vessel and grows radially outwards while subjected to a zero-mean, uniform turbulence. High-speed schlieren imaging, laser tomography, and pressure trace measurements are the commonly employed measurement techniques used to track the flame propagation rate. This configuration offers several advantages over a burner-type setup wherein high mean flow velocities are required to achieve strong intensity levels and to stabilize high S_L flames on the burner. Moreover, the uniformity of the flow field is difficult to control in a burner and is affected by the downstream decay of turbulence due to boundary layer interference [15]. A fan-stirred vessel eliminates such disadvantages associated with a flowing system and enables flame speed measurements in HIT conditions even at large values of u' . However, turbulent explosion vessels are extremely challenging to design and are highly cost prohibitive to build. Additionally, the problem of unsteady flame propagation is compounded by the lack of a well-defined surface that can be used to tag the measured

burning velocity. Nevertheless, recent studies ([1], [15]) have shown these difficulties can be circumvented through appropriate assumptions. Table 2 surveys some of the existing facilities developed to study spherically expanding, turbulent flames. Some cells in the table are left blank as data were not provided in the literature.

The two parameters that are commonly used to describe such flow fields are the turbulence intensity (u') and the integral length scale (L_T). There is sufficient clarity on the effect of u' on turbulent flame speeds. S_T initially increases with u' , reaches a maximum and then decreases until flame quenching is observed. At low-intensity turbulence ($u' < S_L$), flame propagation dominates the flame wrinkling caused by turbulence, and this regime is not of relevance to industrial systems. However, at higher intensity levels ($u' > S_L$), marked intensification of flame speeds due to the enhanced heat and mass transfer rates is effected by turbulent diffusion. The turbulence intensity inside a fan-stirred vessel is typically varied by adjusting the rotational speeds of the fans. The mean velocity is negligible at the center of the vessel and gradually increases as the fans are approached. A majority of the facilities listed in Table 1 report a uniform velocity field in a spherical region at the center of the vessel with the exception of two studies. Leisenheimer and Leuckel [28] and Weiß et al. [39] have indicated the existence of a non-linear, radial velocity distribution inside a spherical flame speed vessel. The former stated that u' increased from 1.4 m/s at the center of the vessel to 2.4 m/s at $r/R = 0.5$ (ratio of the radial location to the vessel radius, R), followed by a decrease in intensity level, thus resulting in an inhomogeneous flow field. The latter observed a similar increase in intensity levels up to $r/R = 0.68$, and the radial

velocity profile became more pronounced at higher fan speeds. These observed anomalies could be facility specific; nonetheless, it is imperative that HIT conditions be maintained at least inside the spherical volume having a radius equal to the maximum flame size used for measurement.

The integral length scale (L_T) remains constant at all fan speeds and is also spatially uniform. Kwon [40] changed the pitch angle of the impellers from 45° (originally used by Fansler and Groff in [41]) to 30° and reported a 50% decrement in L_T despite the fact that the turbulent intensity levels did not change between the two designs. It was concluded that the geometry of the impeller affects the way turbulent eddies are shed from the impeller tip thereby influencing the integral length scale. In a later publication [42], it was stated that the misalignment of the impellers inside the vessel were also corrected, which eliminated the mean flow (previously $\sim 0.3\text{-}0.6 u'$) making it almost negligible ($0.1u'$). This mean velocity correction reduced the errors in the recurrence-rate correlations from the hot-wire data, which in turn caused a drastic reduction in τ by a factor of two. Since L_T was defined as the product of τ and u' , a reduction in τ led to a corresponding decrease in the length scale. It is therefore inconclusive whether the reduction in L_T was brought about by the change in the pitch angle or due to a measurement error.

Leisenheimer and Leuckel [28] used two vessels of different sizes ($\Phi 50$ cm and $\Phi 130$ cm) to vary L_T and predicted that the integral length scale was dependent on the vessel dimensions rather than the impeller geometry. Additionally, the size of the impellers and

their numbers used were also changed in that study. They also proposed a relationship between L_T and the vessel radius (R), $L_T = 1/27R$, which, as evident from Table 2, is not universal. Nevertheless, larger values of L_T are associated with larger R . Shy et al. [43] used perforated plates in front of the mixing fans in an attempt to break down large vortices shed from the impellers, thereby promoting rapid mixing. Liu et al. ([44], [45]) extensively studied the effect of the geometry of such plates on the downstream turbulent flow field inside a wind tunnel. They concluded that both u' and L_T can be changed independently by varying the orifice size and the solidity ratios (area fraction of the solid portion of the plate). Though Shy et al. [43] investigated the effect of solidity ratio on the uniformity (homogeneity) of the flow field; its impact on L_T was not analyzed. Although a homogeneous field was generated, they observed appreciable anisotropy having a spatially averaged value of 1.25.

These existing facilities have reported flame speed measurements at different turbulent intensities but lack the ability to change the integral length scale within the same vessel. To compare the data from different rigs using the spherical bomb method, it is necessary that the influence of these governing parameters on S_T be fully understood. This capability to independently change the turbulence parameters will provide new insights into the geometrical or rig dependencies associated with S_T , thus leading to better correlation amongst data from various rigs.

Table 2. Facility survey of spherically expanding turbulent flames

	Leeds-I	Michigan		Leisenheimer and Leuckel	Brutscher	Kitigawa	Kido	Weiß	Shy	Leeds-II	Current Facility
Reference	Abdel-Gayed et al. (1984)	Fansler and Groff 1990	Kwon et al. 1992	Leisenheimer and Leuckel (1996)	Brutscher et al. (2002)	Smallbone et al. (2006)	Nakahara and Kido (2008)	Weiß et al. (2008)	Shy et al. 2000; Liu et al. 2011	Bradley et al. (2011)	de Vries (2009)
Vessel Shape	Cylindrical	Cylindrical	Cylindrical	Spherical	Cylindrical	Intersection of three 26.5cm ϕ cylinders	Quasi-Spherical	Cuboid with spherical cavity at center	Intersection of two cylinders	Spherical	Cylindrical
ID (cm)	30.5	26	26	Vessel 1(V1): d=50	4.2L	Equivalent Sphere 40.6 ϕ	12	11.8	Cubic volume of 15x15x15 cm ³	38	30.5
IL (cm)	30.5	26	26	Vessel 2(V2): d=130.2			12	11.8		38	35.6
No. Optical Ports	2	2	2+2 laser ports	2	2	2	2	4	4	3	2
Optical Port Size (cm)	15	9.2 (8cm Max Flame dia)	9.2; 10mm	-	-	16	8	10	10	15	12.7
Meas. Technique[#]	a	a	a,c	b	b	a	b	b	c	a,b	a,b
No of Fans	4	4	4	V1: 2,4,8; V2: 4	2	2	4	8	2	4	4
Fan Dia (cm)	10	13.5	13.5	V1: 25; V2:42	-	-	-	4.5	11.6	-	7.62
Fan Blades	8	8		-	-	-	-	6	8	8	3
Pitch Angle (Degrees)	30°	45°	30°	-	-	-	-	22.5°	-	-	20°
FanWidth (cm)	2.5	2.3		-	-	-	-	0.6	4	-	3.8
Turb. Char. Tech.	LDV	LDV	LDV	5-hole Pitot probe and HWA	LDA	PIV	HWA	LDV/PIV	LDV/PIV	LDV	PIV
Max u' (m/s)	16	2		V1: 1.54 m/s; V2: 2.4 m/s	3	3.5	3.7	~3.7	4.5	12	3.5
Longitudinal L_r(mm)	38-42	25mm w/ u'; 40mm using 3D Gaussian u'	12.5; 19.15mm with 3D Gaussian u'	V1: 9 \pm 1mm; V2: 24 \pm 2mm	4.1	1.2	3.3 \pm 0.3	3.9	15 to 48	20	50
Comments		U _{mean} = 0.3u' at center increasing to (0.6 \pm 0.2)u' at r=40mm; 20% Homogeneous; 12% Isotropic; Velocity PDF: Sk=0 \pm 0.1; K=3.1 \pm 0.3	HIT region upto r= 30mm from center of vessel; 10% Homogeneous and Isotropic	The flow field was not homogenous and a radial velocity profile was observed	Measured Radial velocity profile	PIV ROI: 44x34mm; Deviation from Isotropy at higher fan speeds	ϕ 10cm Perforated Plates in front of fans	U _{mean} = 0.2u'	Perforated Plates; Isotropy Ratio =1.25		

#- a: Schlieren; b: Pressure Trace; c: Laser Tomography

3. Experimental setup and impeller design methodology

The existing laminar flame speed vessel is a thick-walled aluminum cylinder (AL 7075-T6) with dimensions 30.5 cm ID \times 35.6 cm L (described in detail in [9]). It is also equipped with a pair of 12.7-cm optical quality quartz viewing windows at the ends of the symmetric axis. The growth of the spherically expanding flame ball under isobaric conditions is optically tracked using high-speed schlieren photography. This vessel will be modified to

accommodate mixing fans to induce an HIT-type field at its center. To better understand the control mechanism for u' and L_T , a parametric study to ascertain the effects of impeller geometry on turbulent statistics was conducted. The aim of this impeller study was twofold: (1) to develop an acceptable impeller design capable of generating near-HIT conditions inside the cylinder; and, (2) to check whether the turbulence parameters can be varied independently by changing the geometrical features of the impeller.

A Plexiglas (clear acrylic) model of the flame speed vessel was fabricated in an attempt to gain a quantitative understanding of the flow fields generated by various impellers without any modification to the existing flame speed vessel. The model had a 33 cm ID \times 30.5 cm L making it almost a 1:1 scale with the aluminum bomb. Four impellers were arranged symmetrically along the central circumference, as shown in Fig. 9. The separation distances between two opposing impellers in the vertical and the horizontal directions were kept constant at 20.32 cm. The rotational speeds of all four motors turning the impellers were set to 8300 ± 100 RPM. Two-dimensional digital particle image velocimetry was used to characterize the flow field within a rectangular field-of-view (FOV) in the mid-axial plane of the rig. The intent here was to quantify the turbulence parameters u' and L_T as well as the flow field characteristics such as homogeneity and isotropy ratios within the measurement area for the different fan designs.

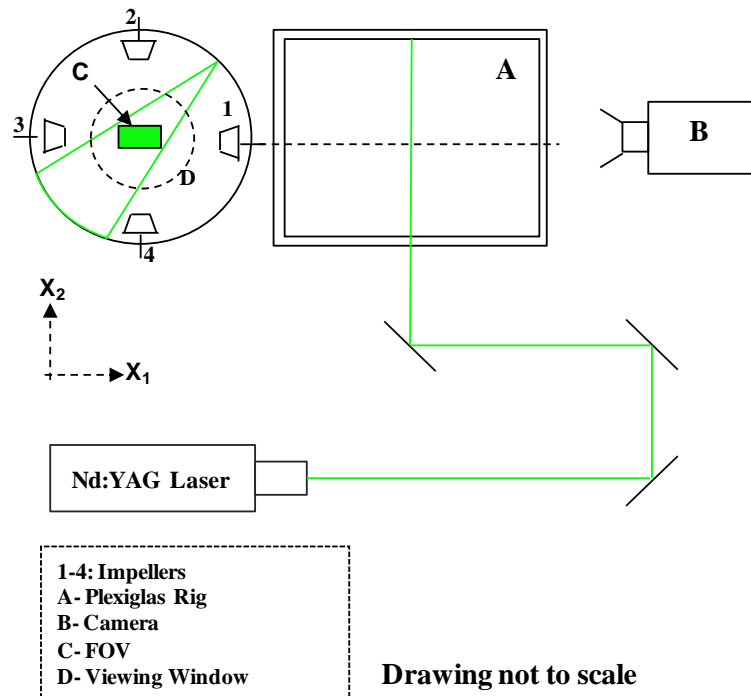


Figure 9. Schematic of the experimental arrangement. The Plexiglas rig with four impellers mounted circumferentially around the central plane is shown. The laser sheet enters through the top right corner at 45° from the vertical. A CCD camera is mounted on fine adjustment stages to provide a rectangular field-of-view, at the center in the mid-axial plane. The FOV coincides with the center of the viewing window of the existing flame speed vessel.

The impellers used in this study were radial-type fans that directed the flow towards the walls of the vessel instead of directing it towards the center of the vessel, as this configuration was found to yield higher values of turbulence intensities [41]. Radial-type blade design was chosen over axial impellers as the former is used extensively for high-shear (mixing) applications in chemical reactor designs. The effect of the geometric parameters, namely the pitch angle of the fan blade (degrees) and the number of blades on

the impeller, were investigated in the present study (shown in Fig. 10). Prototypes with wide variations of the two parameters were fabricated.

The extreme values for each parameter were 20° and 60° (for blade pitch angle), and 3 and 6 for the number of blades on the impeller wheel. The axial length of the impellers was kept constant at 3.8 cm (1.5 inches). The rationale behind this fixed axial length is to enable measurement of burning velocity from the pressure trace without any interference from the impellers for flames whose sizes exceed the viewing window diameter. Hence, much variation of the impeller axial length was not possible. The specifications of the prototypes tested are listed in Table 3. Four sets of each prototype were fabricated by laser sintering using Nylon GF.

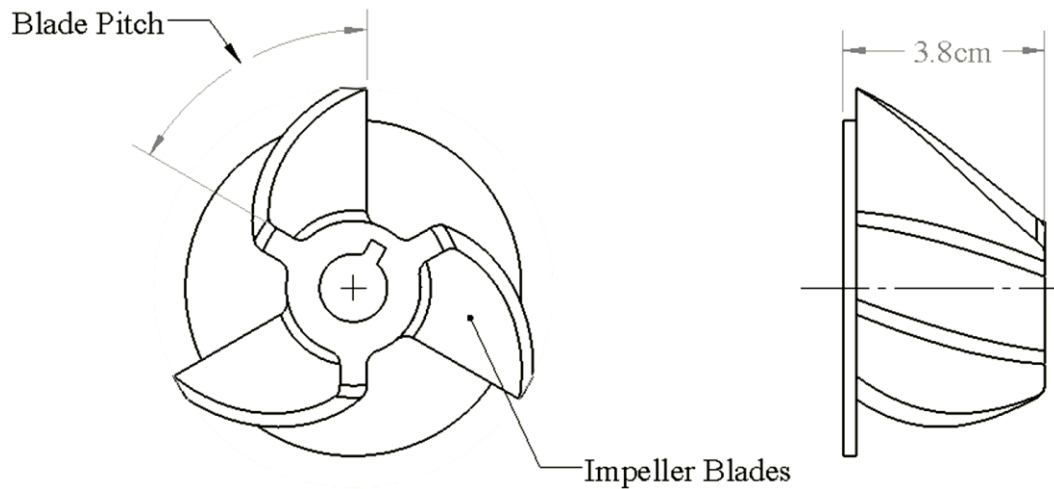


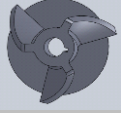


Figure 10. Geometrical parameters for the impellers used in this study. The axial length of the impeller (3.8 cm) was kept constant and the remaining parameters were varied.

Table 3. Prototype specifications used in this study.

Prototype	Fan OD (cm)	No of Blades	Blade Pitch (Degrees)	CAD Rendering
#1	7.6	3	20	
#2	7.6	6	20	
#3	7.6	3	60	

4. Particle image velocimetry system

The flow was illuminated using a New Wave Solo XT 120 dual-head Nd:YAG laser (energy of 120 mJ/pulse at 532 nm wavelength with a pulse duration of 4 ns). The time separation between consecutive pulses was set to 200 μ s. This pulse timing yielded a nominal instantaneous displacement of approximately 15 pixels with the fans running, based upon the root mean square (RMS) of the fluctuating velocity described in Section 5.1 and Table 3. An initial laser beam, 10 mm in diameter, was shaped into a thin sheet using a combination of cylindrical and spherical lenses. The beam entered perpendicular to the cylindrical surface at an angle of 45° downwards from the vertical as shown in Fig. 9. A knife-edge filter was used to remove the low-energy fringes of the laser sheet prior to entering the rig, producing a sheet thickness of approximately 1 mm (estimated from the knife-edge separation). This configuration resulted in a near-top-hat light intensity distribution and provided better control over the light sheet thickness. Prior to data

collection, a calibration plate was placed at the center of the field-of-view (FOV), which allowed the laser sheet to be aligned with the center plane of the vessel, and in parallel with the camera image plane. The digital resolution of approximately 45 pixels/mm was calculated from the known grid spacing on the calibration plate. The flow was imaged using a 14-bit, Peltier-cooled, Cooke PCO 1600 charge-coupled display (CCD) camera, with a 1600×1200 pixel sensor (7.4 μm pixel size). The camera was equipped with a Nikon f/2.8 60 mm lens set at f-number, $f_{\#}=11$, in combination with a 36-mm extension ring. Furthermore, translation stages enabled fine adjustment of the focal plane and the FOV. This arrangement provided a FOV of approximately $36 \times 26 \text{ mm}^2$ with a digital resolution approximately 45 pixels/mm, yielding a linear magnification of 0.33 in the two orthogonal directions as defined in Fig. 9.

Titanium dioxide (TiO_2) particles (40 nm manufacturer's quoted mean diameter) were used for seeding. The authors anticipated that particle agglomeration would produce an effective diameter several times larger than the nominal particle size. However, given the relatively low flow velocities in this study, the resulting particle slip is minimal. Seeded air was flowed into the test cell and was allowed to reach a quasi-stationary state. Once the fans were activated, the data acquisition process was initiated, and particle image pairs were recorded at 10 Hz. Three sets of 345 image pairs were collected totaling 1035 image pairs for each prototype. The velocity vector fields were obtained by means of cross-correlation of the particle images using DaVis 8.0 (LaVision[®]). An adaptive, multi-pass process with increasingly smaller interrogation window sizes was implemented.

Interrogation windows were successively reduced from a 128×128 pixels window to a final window size of 64×64 pixels with a 50% overlap factor. The final vector spacing was 0.72 mm which resulted in a 50×38 vector grid. Vector validation was achieved by the median test. Spurious vectors were found to be less than 2% and were replaced using linear interpolants from the neighboring vectors. Post-processing of the velocity vector fields included a two standard deviation filter to obtain the time-averaged flow field based on an ensemble size of $N=1035$ images. The statistical uncertainty of the streamwise velocity component due to a finite number of samples was calculated using the estimator variance, σ_u/\sqrt{N} . This calculation returned an uncertainty on the mean streamwise velocity of ± 0.1 m/s with a 95% confidence level. The same result was obtained for the vertical velocity component as well.

5. Turbulence statistics

a. Mean flow, RMS intensity, and velocity PDF

The instantaneous velocity vectors, $u_i(x_1, x_2)$, were ensemble averaged over all 1035 vector maps to yield the mean velocity field, $U_i(x_1, x_2)$, for each prototype. The mean velocities were then subtracted from the instantaneous vectors to obtain the velocity fluctuations $u_i'(x_1, x_2)$ from which the RMS values of the turbulent intensities were computed. Table 4 summarizes the mean and the spatially averaged RMS velocities in the two orthogonal directions for all prototypes. As evident, the mean flow was negligible (at most $0.1u'$) for all prototypes. Figs. 11(a) and 11(b) show a sample snapshot of the

instantaneous velocity map and the resultant mean velocity field respectively for prototype #1. It should be noted that the reference vector in Fig. 11(b) is scaled up by a factor of five relative to Fig. 11(a) for better visual clarity. A vortex near the center of the vessel was evident from the mean flow field. The streamline topology (not shown here for conciseness) showed spiraling streamlines, thereby suggesting that the flow was three-dimensional. This observed mean flow could be attributed to the non-symmetric nature of the vessel or due to a slight misalignment of the fans or a slight variability in the fan speeds. Regardless, the fluctuation statistics indicated that this slight mean flow bias was not a significant issue since the mean flow was still negligible when compared to the turbulent intensities. Further, the RMS turbulent intensities showed no appreciable variation with impeller geometry. The prototypes tested had the same fan OD and were turning at approximately the same rotational speeds. Additionally, their moments of inertia were nearly equal. Hence the rotational kinetic energies supplied to the confined volume were the same irrespective of the prototypes, which could explain the near-equal intensity levels that were measured. This result is an indicator that the blade tip velocities (defined as the product of the fan radius and the rotational speed) of the impellers control the intensity levels attained inside the vessel. So, an increase in the fan RPM will effect an increase in the intensity level. This trend is consistent with what is commonly observed in the literature.

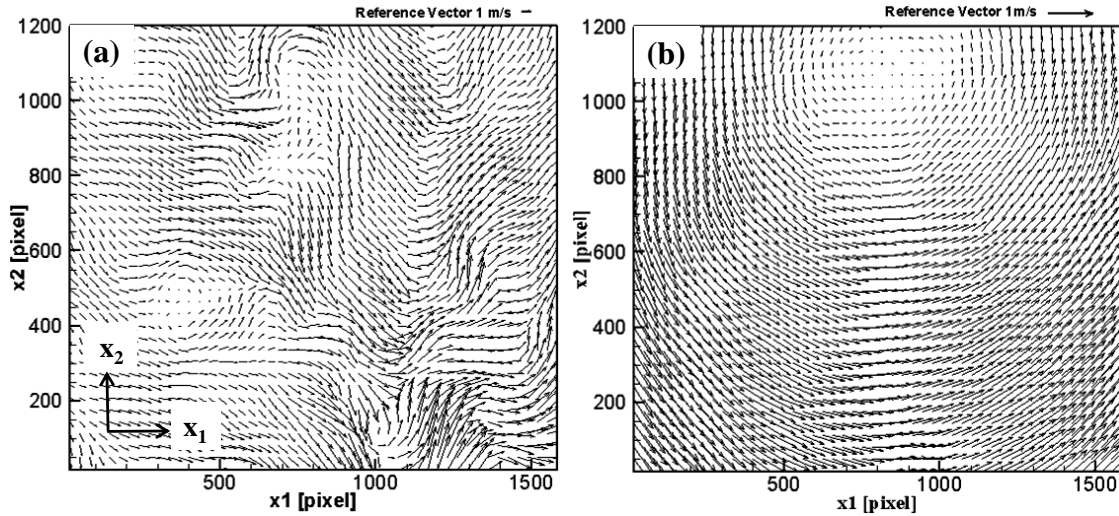


Figure 11. (a) Instantaneous velocity field (b) Mean velocity field for prototype 1. The reference vector in Fig 11(b) is scaled up by factor of five to clearly display the negligible mean velocity field in contrast to the fluctuating field.

The PDFs were estimated for the normalized fluctuating fields (instantaneous field/local RMS), $u_i'(x_1, x_2)/u_{i,rms}(x_1, x_2)$. These are shown in Fig. 12. To check for the Gaussianity of the PDFs, higher-order standardized moments, namely skewness (Sk) and kurtosis (flatness) (K), were computed for all three prototypes and are shown in Table 4. The skewness factors of all prototypes are near-zero, indicating no biasing of the velocity fields. The velocity PDFs exhibit slightly peaked profiles as evident from the flatness factors. This effect is amplified for prototype #2 (higher number of blades). Such peaked profiles are commonly observed in fan-stirred vessels ([36], [41]). This result can be attributed to the lack of an auxiliary device such as a perforated plate in front of the impellers that assists in the introduction of the intermediate scales using the vortex breakdown principle. However, Abdel Gayed et al. [36] showed that with an increase in

the turbulence intensity levels, relaxation of the peaks occurs, and the PDFs assume near-Gaussian-like profiles. This observation is a direct consequence of the widening of the attainable range of velocity scales at higher intensities. It should also be noted that numerical values of higher-order moments can be unreliable due to the sensitivity to noise in the PDF wings [41].

Table 4. Mean, Spatial RMS and higher order moments- skewness and kurtosis for all prototypes

	U_i (m/s)	u'	Sk	K
Prototype 1: Baseline Case				
x_1	0.03	1.48	0.04	3.5
x_2	-0.01	1.49	0.03	3.5
Prototype 2: Higher No of Blades				
x_1	0.05	1.17	-0.02	3.9
x_2	0.00	1.39	0.04	3.7
Prototype 3: Higher Pitch Angle				
x_1	0.14	1.57	0.05	3.6
x_2	-0.04	1.67	0.10	3.7

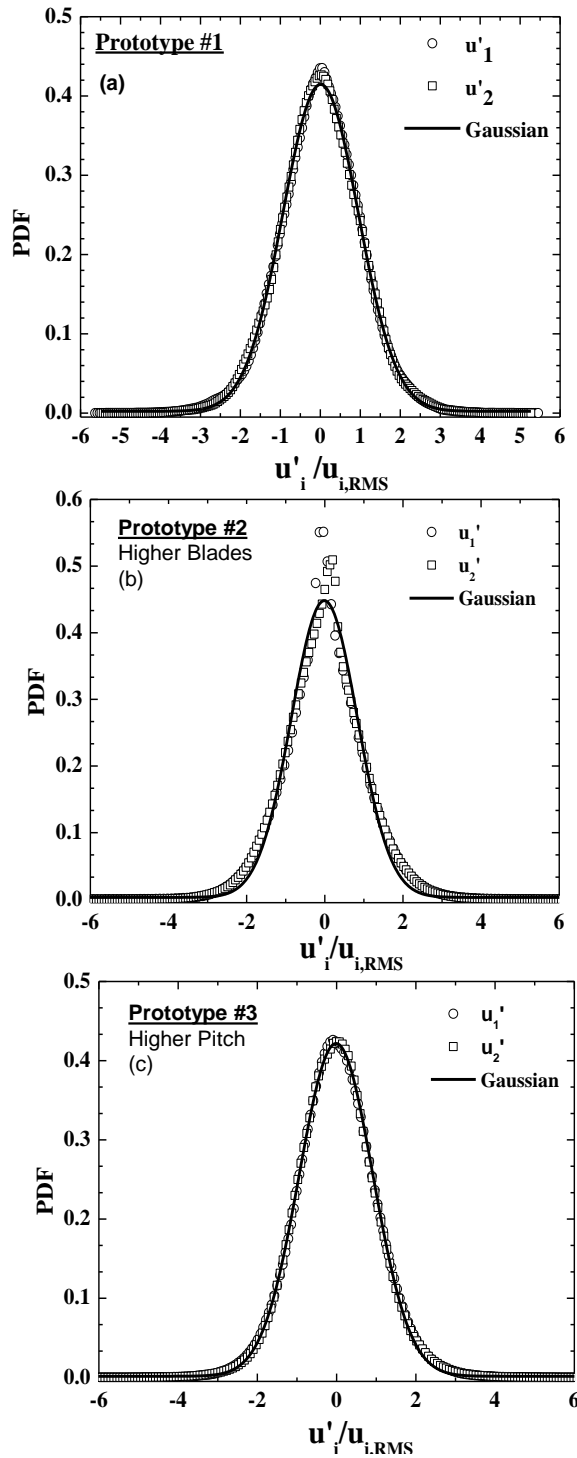


Figure 12. Velocity PDFs for all prototypes: (a) Prototype #1 (b) Prototype #3- Higher number of blades (c) greater pitch angle. Gaussian curves are also included.

b. Homogeneity and isotropy ratios

Homogeneous turbulence implies that the flow field is statistically independent of the shift of the coordinate system [50]. Homogeneity (H_{xi}) ratio quantifies the uniformity of the flow field and is computed as the ratio of the local RMS velocity to the spatially averaged RMS velocity in the same direction (Eq. 20).

$$H_{xi}(x_1, x_2) = u_{i,rms}(x_1, x_2) / \overline{u_{i,rms}(x_1, x_2)} \quad (20)$$

Isotropic turbulence can be defined as statistical invariance of the flow field to rotation and reflections of the coordinate system. Isotropy (I) ratio is estimated from the ratio of the local RMS values in the two directions and is given by (Eq. 21),

$$I(x_1, x_2) = u_{1,rms}(x_1, x_2) / u_{2,rms}(x_1, x_2) \quad (21)$$

These ratios become unity for perfectly homogeneous and isotropic turbulent flow. An HIT flow field can then be fully described by merely a single RMS intensity value which is representative of all velocity components as well as their spatial variations. For a flame speed experiment, this simplification translates to perturbation of the growing flame ball by external disturbances acting uniformly and equally in all directions. Spatial maps of

homogeneity and isotropy ratios were generated from the measured vector fields. One such map is shown in Fig. 13 (for prototype # 1). The intensity levels in the spatial map directly correspond to the magnitudes of the homogeneity and isotropy ratios. Additionally, the histograms of the spatial maps as well as the cumulative distribution functions (CDF) for the histograms were generated to provide a detailed quantitative assessment. Any point on the CDF curve corresponds to the fraction of the grid points in the characterization region that lie below a certain homogeneity or isotropy limit. The CDF profiles in Fig. 13 reveal that the homogeneity and isotropy ratios for the majority of the grid points (> 95%) fall within a narrow band (0.9-1.1) close to unity, thus indicating near-HIT conditions.

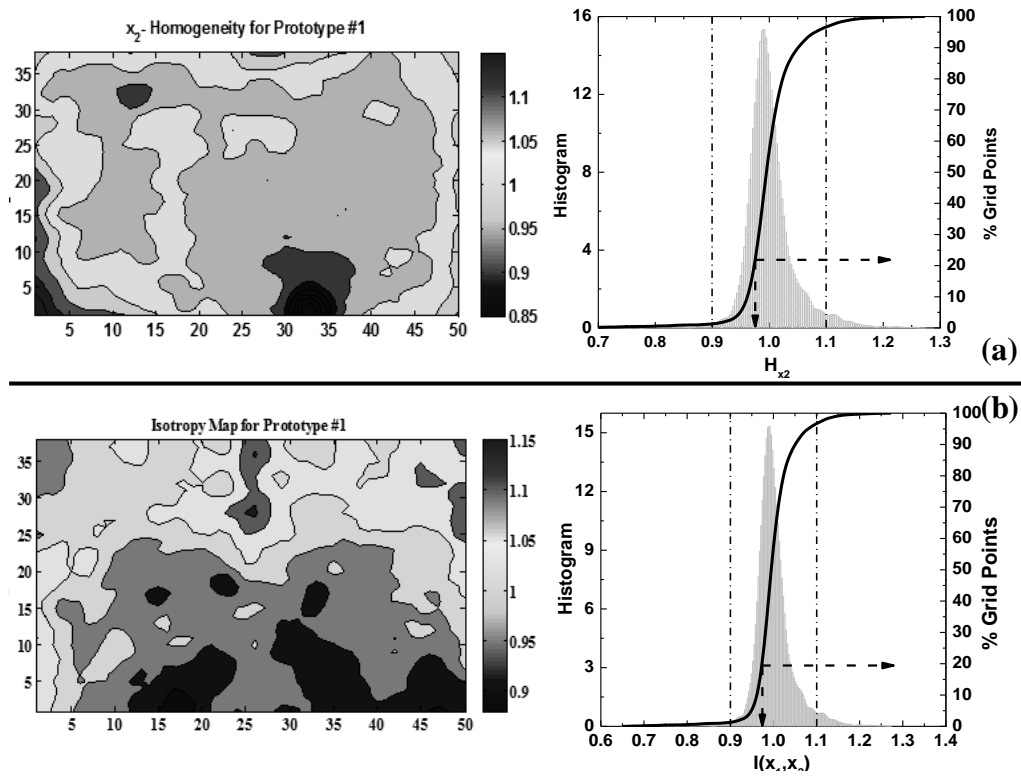


Figure 13. (a) x_2 -Homogeneity map (b) Isotropy map for prototype #1. The histograms (vertical bars) of the spatial maps are shown on the right indicating near-ideal ($\pm 10\%$) conditions. These are further supported by the cumulative distribution functions profile (curve) of the histogram

CDFs facilitate the comparison of the spatial variations in homogeneity and isotropy of the velocity fields generated by different prototypes. These are shown in Fig. 14. As evident from the CDF profiles, the homogeneity of the flow field is not sensitive to the blade pitch angle, and the homogeneity ratios in both the directions remained within the qualification bands ($\pm 10\%$) for the two prototypes. The horizontal homogeneity increased to $\pm 30\%$ for the prototype with the higher number of blades. Nevertheless, the spatial averages of the homogeneities in both the directions were still close to unity regardless of

the impeller geometry. On the contrary, a clear deviation from isotropy can be seen for the prototype with a higher number of blades, thus highlighting the strong sensitivity of the isotropy ratio to changes in the impeller geometry. The spatial average of the isotropy ratio remained near unity for prototype #1 and for the higher pitch angle case (#3), but increased to 1.2 for the impeller with a higher number of blades (#2). To understand the driving mechanisms behind these observations, analysis of the impeller wakes is necessary. This additional work is however outside the scope of this study.

6. Two-point velocity correlations

Two-point velocity correlations in the two orthogonal directions were computed from the fluctuating fields following the same procedure as Hwang and Eaton [31].

The longitudinal correlation coefficients were defined as,

$$F_{11}(r) = \overline{\langle u'_1(x_1, x_2)u'_1(x_1 + r, x_2) \rangle} / \overline{u_{1,RMS}^2} \quad (22)$$

$$F_{22}(r) = \overline{\langle u'_2(x_1, x_2)u'_2(x_1, x_2 + r) \rangle} / \overline{u_{2,RMS}^2} \quad (23)$$

And the lateral correlation coefficients were estimated as,

$$G_{11}(r) = \overline{\langle u'_1(x_1, x_2)u'_1(x_1, x_2 + r) \rangle} / \overline{u_{1,RMS}}^2 \quad (24)$$

$$G_{22}(r) = \overline{\langle u'_2(x_1, x_2)u'_2(x_1 + r, x_2) \rangle} / \overline{u_{2,RMS}}^2 \quad (25)$$

where $\overline{\langle \rangle}$ indicate spatial and ensemble averages, and r is the separation distance.

Furthermore, for isotropic turbulence, the correlation coefficients are related by,

$$G(r) = F(r) + \frac{r}{2} \frac{\partial F(r)}{\partial r} \quad (26)$$

The correlation coefficients are plotted for all prototypes in Fig. 15. Also shown are the calculated lateral coefficients determined using Eq. 26. The computed lateral coefficient matches closely with the measured values for prototypes #1 and #3 indicating the existence of isotropic fields. However, there is a disagreement between the measured and predicted values for the prototype with the higher number of blades. Thus it can be concluded that the prototype with the higher number of blades generated anisotropic flow fields. These results on the isotropic nature of the flow fields are consistent with the conclusions that were drawn directly based on the velocity maps.

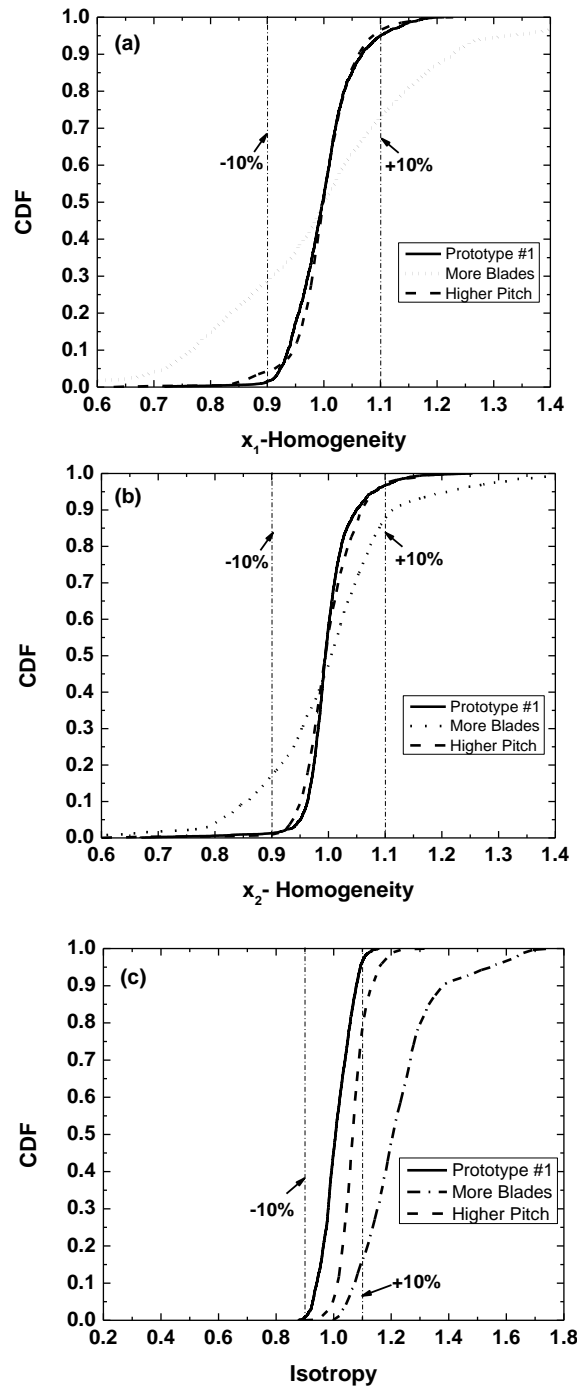


Figure 14. CDFs of the spatial plots of (a) x_1 -Homogeneity (H_{x1}) (b) x_2 -Homogeneity (H_{x2}) (c) Isotropy (I) ratios for the various prototypes. Acceptable limits were set between 0.9 and 1.1 for all cases representative of HIT conditions.

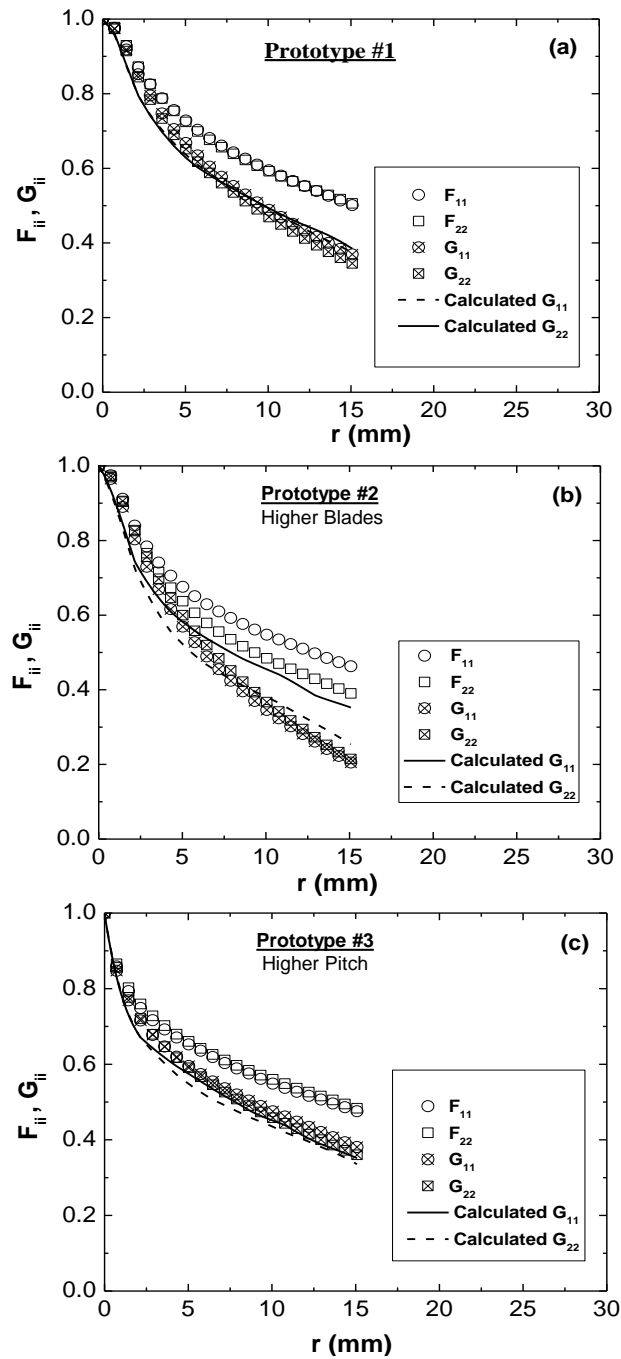


Figure 15. Correlation coefficients of the impellers in the longitudinal and lateral directions. There is good agreement between the measured and computed lateral coefficients for prototypes #1 and #3 indicating isotropy. Anisotropy is evident for prototype #2

7. Energy spectra

One-dimensional spatial energy spectra were computed for all prototypes using a procedure similar to the one outlined in Doron et al. [51]. The spectral energy density is then estimated as,

$$E_{ii}(\kappa_i, x_j) = \frac{L}{2\pi N^2} \sum_n F_i(\kappa_i, x_j) F_i^*(\kappa_i, x_j); i \neq j \quad (27)$$

where,

F_i is the fast Fourier transform (FFT) of the fluctuating velocity in the i^{th} direction and is defined as,

$$F_i(\kappa_i, x_j) = \sum_n u'_i(x_n, x_j) \exp(-i\kappa_i x_n); i \neq j \quad (28)$$

F_i^* denotes the complex conjugate of the FFT

κ_i is the wavenumber in the i^{th} direction

L is the domain length

N is the number of vectors in the fields

The subscript j is fixed for the specific operation. The spectral densities were averaged over all rows or columns within each velocity map, and then ensemble averaged over all

images. The energy spectra of all prototypes are plotted in Fig. 16. Also shown are the lower significant (κ_{\min}) and the cutoff (κ_c) wave numbers [52]. The lower significant wavenumber, $\kappa_{\min}= 175$ rad/m, corresponds to the physical length of the field-of-view. The cutoff wavenumber which demarcates the resolved scales from the unresolved scales was estimated as, $\kappa_c= 1971$ rad/m (using Eq. 29).

$$\kappa_c = 2.8/\Delta \quad (29)$$

where,

Δ : final PIV interrogation window size

Additionally, the relation between the transverse and longitudinal spectra for isotropic turbulence (Eq. 30) was also verified for all cases [50].

$$E_{\alpha\alpha}(\kappa_\alpha) = \frac{3}{4}E_{\beta\beta}(\kappa_\alpha) \quad (30)$$

Similar to the two-point correlations, a consensus between the energy spectra and the direct evaluation method with regard to the isotropic nature of the various flow fields was observed.

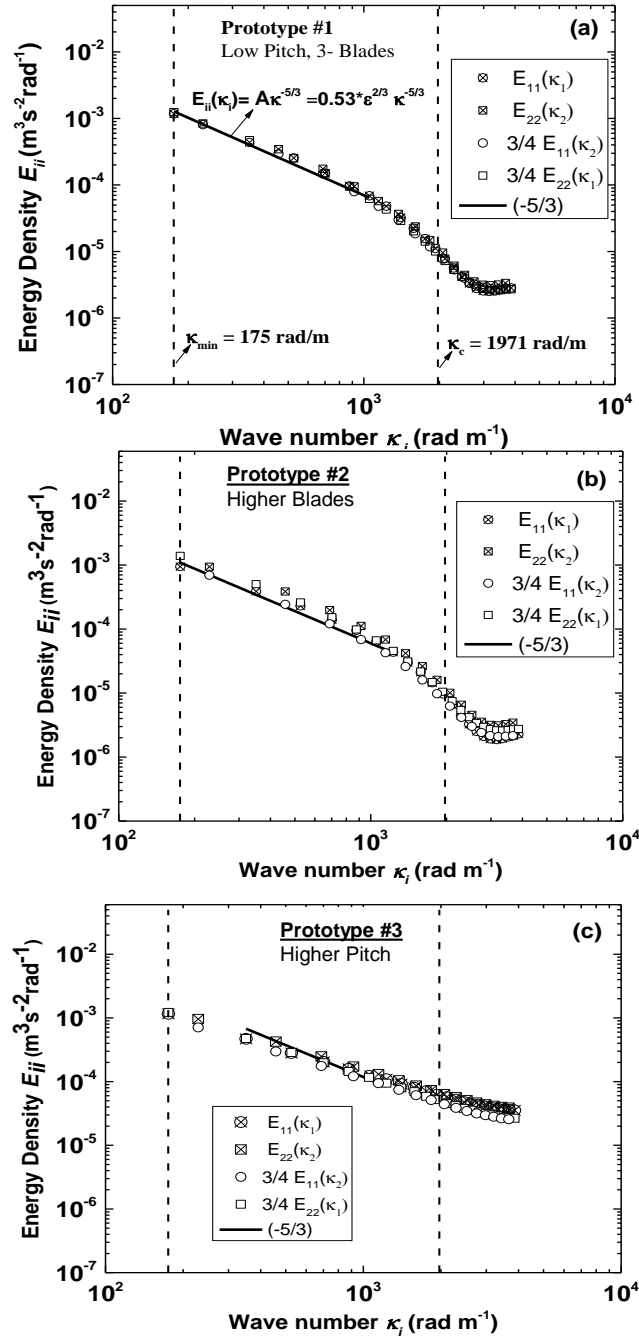


Figure 16. Energy spectra for all prototypes. (-5/3) linear fits in the inertial subrange were used to estimate the dissipation rate from the spectra. The lower significant wavenumber, $k_{\min}=175 \text{ rad/m}$ and the cutoff wavenumber, $k_c=1971 \text{ rad/m}$ are shown as vertical dashed lines. Isotropy criterion was also verified for each case

8. Turbulent kinetic energy dissipation rate and turbulence statistics

a. Dissipation rate (ε)

Turbulent kinetic energy dissipation rate (ε) is required to estimate the different length scales such as the Euler (integral), Taylor, and Kolmogorov scales. The dissipation rate is defined as the ensemble average of the square of the strain rate tensor (s_{ij}) and is given by Eq. 31 [50]. To measure the dissipation rate directly from the PIV velocity data, the spatial resolution (Δ) must be as small as the Kolmogorov scales (η) to accurately compute the spatial velocity derivatives [53]. For example, Hwang and Eaton [31] reported spatial variations as high as 69-154% for dissipation rates which they attributed to the errors in estimating the spatial velocity derivatives due to insufficient spatial resolution ($\Delta/\eta \approx 4.8$). As a result, indirect methods are often used to estimate the dissipation rate. These methods include spectral and structure function fitting, LES analogy, and dimensional scaling [54].

$$\varepsilon = 2\nu \langle s_{ij}s_{ij} \rangle = \nu \left\langle \frac{\partial u_i}{\partial x_j} \frac{\partial u_i}{\partial x_j} + \frac{\partial u_i}{\partial x_j} \frac{\partial u_i}{\partial x_j} \right\rangle; \nu \text{ is the kinematic viscosity} \quad (31)$$

The dissipation rates (ε) for all the prototypes were estimated using the spectral fitting method. The inertial subrange was observed in the spectra for all prototypes. The dissipation rate can then be estimated by fitting a line with a $-5/3$ slope in the inertial subrange. The pre-multiplication factor (A) in Eq. 32 is adjusted to closely fit the

measured data yielding the dissipation rates. The statistical r^2 goodness of fit value was 0.99 for all cases.

$$E_{ii}(\kappa_i) = A \kappa^{-5/3} = 0.53 \varepsilon^{2/3} \kappa^{-5/3} \quad (32)$$

b. Turbulent statistics

Prior to computing the different scales, modified turbulent kinetic energies (TKE), (q^2), were estimated for all prototypes using Eq. 33 [31]. This estimate assumes that the turbulent intensity in the out-of-plane direction is equal to those measured in-plane. The actual turbulent kinetic energy is given by $\frac{1}{2} q^2$.

$$q^2(x_1, x_2) = u_{i,RMS}(x_1, x_2)u_{i,RMS}(x_1, x_2) \cong 3 \frac{u_{1,RMS}^2(x_1, x_2) + u_{2,RMS}^2(x_1, x_2)}{2} \quad (33)$$

The integral length (L_T) and time (τ_E) scales (Euler time macroscale/ eddy turnover time) were then computed using Eqs. 34 and 35, respectively,

$$\text{The integral length scale: } L_T \cong \overline{\left(\frac{(q^2/3)^{3/2}}{\varepsilon}\right)} \quad (34)$$

$$\text{Eulerian time macro scale (eddy turnover time): } \tau_E \cong \overline{\left(\frac{q^2/2}{\varepsilon}\right)} \quad (35)$$

The Taylor microscale (Eq. 36) and the corresponding Reynolds Number (Eq. 37) were calculated using,

$$\text{Taylor Microscale: } \lambda \cong \left(\frac{5\nu q^2}{\varepsilon} \right)^{1/2} \quad (36)$$

$$\text{Taylor Reynolds No: } \text{Re}_\lambda \cong \frac{\lambda(q^2/3)^{1/2}}{\nu} \quad (37)$$

Where, $\nu = 1.57 \times 10^{-5} \text{ m}^2/\text{s}$ is the kinematic viscosity of air at 300 K, 1 atm.

The Kolmogorov scales (Eqs. 38 and 39) were estimated as,

$$\text{Time scale: } \tau_k \cong \left(\frac{\nu}{\varepsilon} \right)^{1/2} \quad (38)$$

$$\text{Length scale: } \eta \cong \left(\frac{\nu^3}{\varepsilon} \right)^{1/4} \quad (39)$$

Spatial averages of the above quantities are summarized in Table 5. It is evident from Table 5 that the impeller geometry influences the integral length scales. L_T changed with the prototype having the higher number of blades as well as with the greater pitch angle

case. However, it was shown earlier that the flow became more anisotropic with a higher number of blades. Hence changing the blade pitch angle will effect a change in L_T while still maintaining HIT conditions. Given the velocity uncertainties and the spatial resolution of these experiments, the Kolmogorov scales shown here are only representative values.

Table 5. Turbulence statistics for all prototypes

Prototype	Mod. Kinetic Energy	Dissipation Rate	Integral Scales		Taylor Scales		Kolmogorov Scales	
	$\overline{q^2}$ [m ² /s ²]	$\overline{\epsilon}$ [m ² /s ³]	τ_ϵ (ms)	L_T (mm)	Re_λ	λ [mm]	τ_k (ms)	η (mm)
#1	6.6	59.7	55	54	277	2.9	0.5	0.1
Higher No of Blades #2	5.1	57.5	44	38	218	2.6	0.5	0.1
Higher Pitch Angle: #3	7.9	109.7	36	39	245	2.4	0.4	0.1

L_T can also be obtained by integrating the two-point velocity correlation curve (i.e., the area under the correlation curve up to the first zero crossing). However, the curves do not reach zero in the present study due to limited FOV size (see Fig. 15). In such situations, the correlation curves are extrapolated to zero using suitable fitting functions. The correlation curves with their respective extrapolations are shown in Fig. 17. It should also be noted that, unlike LDV or hot-wire anemometry, the two-point velocity correlations using PIV are estimated from the velocity maps instead of physically placing the probe at different separation distances and conducting high-frequency measurements. With increase in separation distance (r), the number of velocity samples in each bin decreases. Subsequently, the PIV correlation curves are affected by statistical noise at larger

separation distances [54]. Hence, extrapolating the correlation curves may not truly represent the correlation coefficients at large r . Nevertheless, the correlation curves can still be used to qualitatively assess the isotropic nature of the flow field from the collapse of the coefficients in the different directions (Eq. 26).

The integral length scales were estimated by integrating the extended correlation curves (shown in Table 6). L_T estimated from spectral-fitting (Eq. 15) were significantly larger when compared to those obtained by integrating the 2-point correlations. This discrepancy could be due to the assumption on the out-of-plane velocity component. To verify this argument, the correlation curve from Hwang and Eaton [31] was integrated after fitting a similar exponential function (Fig. 9d). This calculation returned $L_T \approx 19$ mm, which is markedly smaller when compared to $L_T = 56$ mm computed in that study (Eq. 34). It is imperative to note that the out-of-plane velocity was independently measured to be within 2% of the in-plane components in that study. These values of length scales are significantly different from each other despite accurate estimation of the turbulent kinetic energy. This ambiguity in L_T estimation can be explained by the normalized dissipation rate, C_ε , which should be applied to the scaling law, and Eq. 34 is modified as [55],

$$L_T \cong C_\varepsilon \left(\frac{\overline{(q^2/3)^{3/2}}}{\varepsilon} \right) \quad (40)$$

For stationary, homogeneous and isotropic turbulence with energy input at large scales, and with Taylor Reynolds number, $Re_\lambda \geq 200$, DNS studies show that C_ε is close to 0.5

([56]-[58]). The integral length scales were computed after accounting for the normalized dissipation rate ($C_\varepsilon = 0.5$ -Eq. 40) (shown in Table 6). There is now closer agreement between the length scales estimated from the correlation curves and those calculated using Eq. 40 for all cases. The integral length scales computed using Eq. 40 are used herein as no extrapolation was done when calculating them.

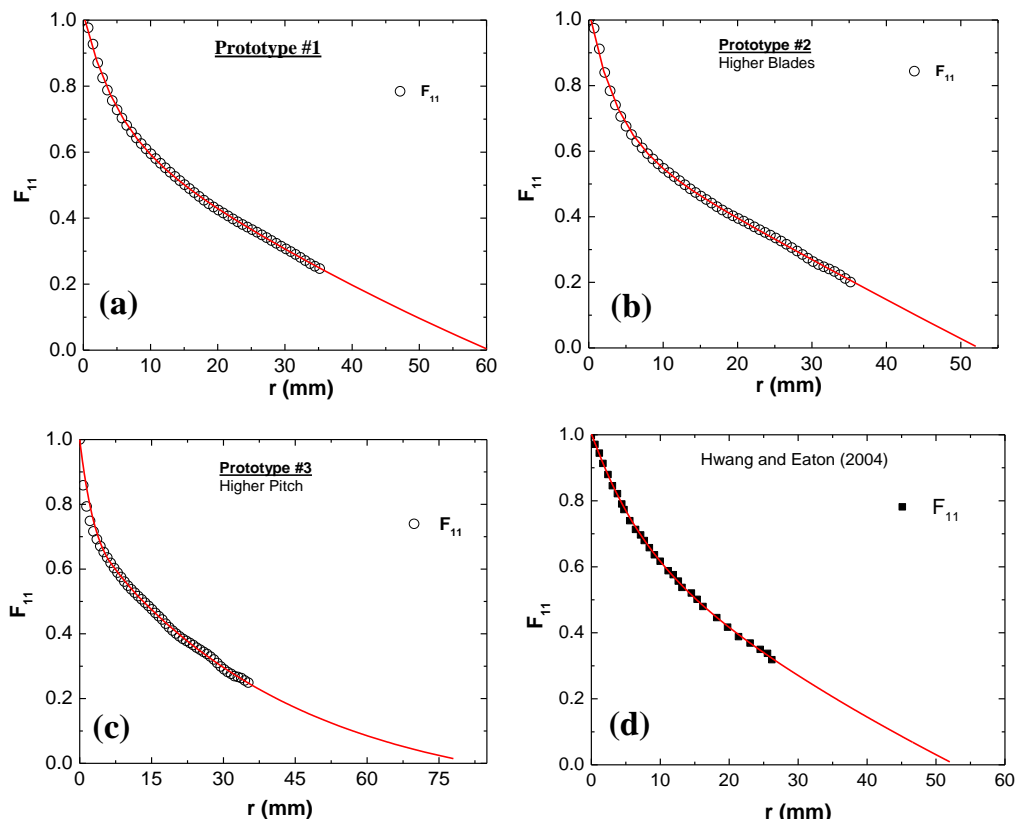


Figure 17. 2-point velocity longitudinal correlations extrapolated to reach zero crossing. Figures (a)-(c) are measurements from this study. (d) The correlation curve from Hwang and Eaton (2004). Symbols are measured correlation coefficients, and the curves are extrapolations extending to the first zero crossing.

Table 6. Integral length scale computations. The values are in millimeters

	Prototype #1	Prototype #2 Higher Blades	Prototype #3 Higher Pitch	Hwang and Eaton [31]
Eq. 15 ($C_\epsilon=1$)	54	38	39	56
Curve Fit F_{11}	21	18	21	19
Measured F_{11} (w/o extrapolation to zero)	18	16	16	15
Measured/ Fit F_{11} ratio	85%	88%	76%	79%
Eq. 21 ($C_\epsilon=0.5$)	27	19	20	28

9. Discussion

This study provided several important results that aid in the design of the impellers for the final turbulent flame speed vessel. Three-bladed impellers will be installed in the same central-symmetric configuration inside the flame bomb to generate HIT conditions inside the vessel. Changing the blade pitch of the impeller caused a change in the integral length scale of turbulence, though not appreciably. Nevertheless, even such small variations in length scale can significantly impact turbulent flame speeds, as in Venkateshwaran et al.[12]. In their study, two different L_T (12 and 20 mm) were employed in a Bunsen burner geometry, and large differences in the burning velocities were observed keeping all other parameters constant. Hence employing impellers with different pitch angles can provide valuable data that can be used to assess the length scale sensitivity of turbulent flame speed. Also, the integral length scales attained in the vessel correlates with those typically observed inside a gas turbine combustor flow field, as evident from Table 7.

As reviewed in the background literature section, guidelines for impeller design for fan-stirred vessels are not available. To generalize the results from this study so that they can

be directly transferred to vessels with different geometries, the geometrical features of the vessel should be taken into account as well, which adds another level of complexity. The objective of the current investigation was to arrive at an optimal impeller geometry that can produce uniform turbulence conditions with flexibility to change the turbulence parameters inside an existing flame bomb. Hence, variations in vessel geometry were not considered. While this paper provides useful flow field information of three different impeller geometries placed in a center-symmetric pattern inside a cylindrical vessel, the applicability of these results to vessels with different geometries cannot be determined from the study conducted here.

Table 7. Integral length scales inside a typical gas turbine

Gas Turbine Model	L_T (mm)	Reference
GE - LM6000	34	Kim and Menon [59]
HiP gas turbine combustor	100	Aldredge [60]
Simulated combustor	40-60	Ames and Moffat [61]
Can-type GT combustor	5.6-15.6	Moss [62]
P&W combustor simulator	60-108	Barringer [63]

10. Summary

A parametric study was conducted to determine the optimum impeller design capable of generating homogeneous and isotropic turbulence inside a closed, fan-stirred, cylindrical flame speed vessel. Additionally, the ability to control the turbulence parameters, u' and

L_T , through geometric modification of the impeller was also evaluated. A 1:1 scale Plexiglas model of the flame bomb was fabricated to allow non-intrusive optical flow field characterization. Four impellers were arranged symmetrically along the central circumference of the cylinder. The impact of blade pitch angle and the number of blades on the impeller were assessed. Digital PIV was used to accurately measure the turbulence statistics, and turbulent intensity levels between 1.2 and 1.7 m/s with negligible mean flow ($<10\% u'$) were attained. Much variation in the intensity levels was not observed for the different impellers. The velocity PDFs of the 3-bladed impellers closely followed a Gaussian profile. The acceptable ranges for homogeneity and isotropy ratios were set in a narrow range between 0.9 and 1.1 ($\pm 10\%$ ideal case). The homogeneity of the flow field showed only a slight dependency on the impeller geometry with the fans arranged in a central-symmetric configuration. However, the isotropy ratio was sensitive to the geometry, and a clear deviation from isotropic turbulence was observed for the prototype with higher number of blades (6-bladed fans).

Two-point velocity correlations in the longitudinal and lateral directions were also computed to further validate the isotropic nature of the flow fields. The inertial subrange with a $-5/3$ slope was observed in the energy spectra. The turbulent kinetic energy dissipation rates as estimated from the energy spectra were used to determine the integral length scales. The integral length scales computed from the scaling law agreed well with those obtained by integrating 2-point velocity correlation curves. It was concluded that

L_T can be changed by varying the blade pitch angle while still maintaining near-HIT conditions.

CHAPTER V

EXPERIMENTAL SETUP

An existing laminar flame speed bomb was upgraded to measure turbulent flame speeds as a part of this study. To that effect, mixing impellers were installed inside it to generate HIT conditions. The impeller geometry was optimized using PIV in a 1:1 scale Plexiglas model of the vessel, and the characterization results are presented in chapter IV. The objective of this chapter is to provide a complete description of the features of the upgraded flame bomb and the associated experimental procedure, and is organized as follows. First, the high-pressure, cylindrical laminar flame bomb is introduced. The features of the fan-stirred vessel are then described. For simplicity, schlieren photography was adopted as the diagnostic technique for both laminar and turbulent combustion studies. The post processing procedure used for laminar flame studies was modified for turbulent flames, and is explained finally.

1. Existing facility description

Laminar flame speeds have been measured at the author's laboratory using a high-pressure, constant-volume flame speed vessel. The flame bomb is a cylindrical chamber vessel made of aircraft-grade aluminum (Al 7075) with an internal diameter of 30.5 cm and an internal length of 35.5 cm. Optical-quality quartz windows on the end caps enable visual tracking of the expanding flame up to a maximum diameter of 12.7 cm under constant-pressure conditions and with negligible cylindrical-confinement effects (wall

effects). Flame speeds up to an initial pressure of 10 atm can be measured. Ignition is provided by means of a spark produced between two polished, stainless steel electrodes placed at the center of the vessel. Schlieren imaging is used in conjunction with a high-speed camera (Photron Fastcam SA 1.1) as the measurement technique. Typical initial temperatures inside the vessel are 298 ± 3 K. The vessel is connected to a rotary-vane vacuum pump to evacuate the products of combustion between experiments. Test mixtures are prepared by the method of partial pressures, and are filled into the vessel by means of an electro-pneumatic gas-fill system that can be remotely operated. The entire facility is isolated within blast-proof, steel-reinforced cinderblock walls as a precautionary safety measure. Figure 18 shows the original laminar flame bomb.

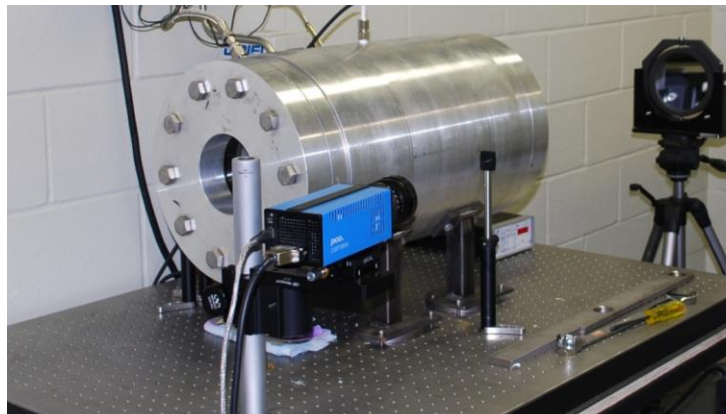


Figure 18. Aluminum laminar flame bomb at Texas A&M University. Flame speeds at initial pressures as high as 10 atm can be measured using schlieren imaging.

Laminar flame speeds of gas-turbine-relevant fuels such as hydrogen, hydrocarbons (C1-C3), di-methyl ether, and syngas-type blends (hydrogen and carbon monoxide mixtures) have been measured over a wide range of pressures, temperatures, and equivalence ratios, which then aid in the development of hierarchical chemical kinetics mechanisms (e.g. [64], [65]). The laminar flame speeds ($S_{L,u}$ or S_L) of C1-C3 hydrocarbons are shown in Fig. 19.

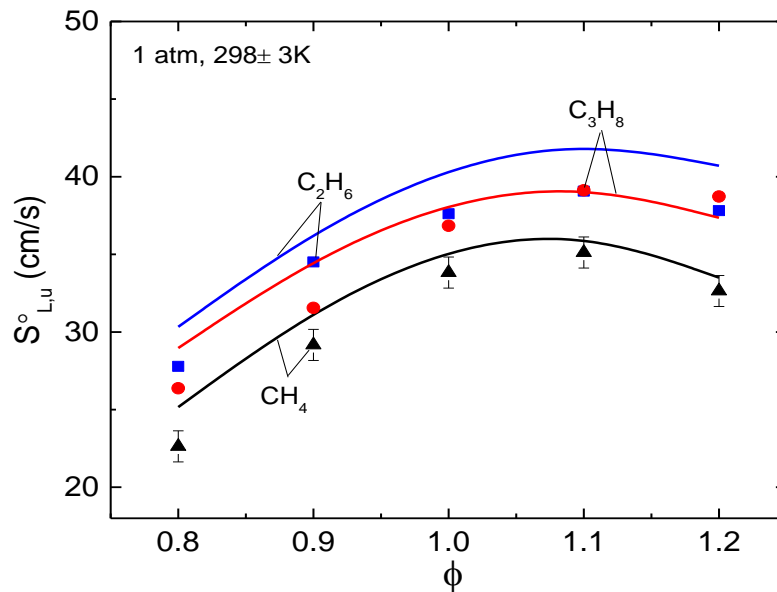


Figure 19. Laminar flame speeds of C1-C3 hydrocarbons in air over a wide range of equivalence ratios. The symbols are experimental measurements from the author's laboratory [64], and the curves are kinetics model predictions at those conditions using the C5 mechanism [66] from the National University of Ireland at Galway (Dr. Curran's Group).

2. Apparatus description

Four fans were recently installed symmetrically around the central circumference of the vessel to generate turbulence during the experiment (See Fig. 20). The fans are radial impellers with three backward-curved blades. They are made of aluminum (Al 6061-T6) with an outer diameter of 76.2 mm and a blade pitch angle of 20° . The fans are fitted on steel shafts (A2 tool steel) that are polished to an extremely high surface finish. The impeller and shaft assemblies are finely balanced to 18,000 rpm prior to installation.

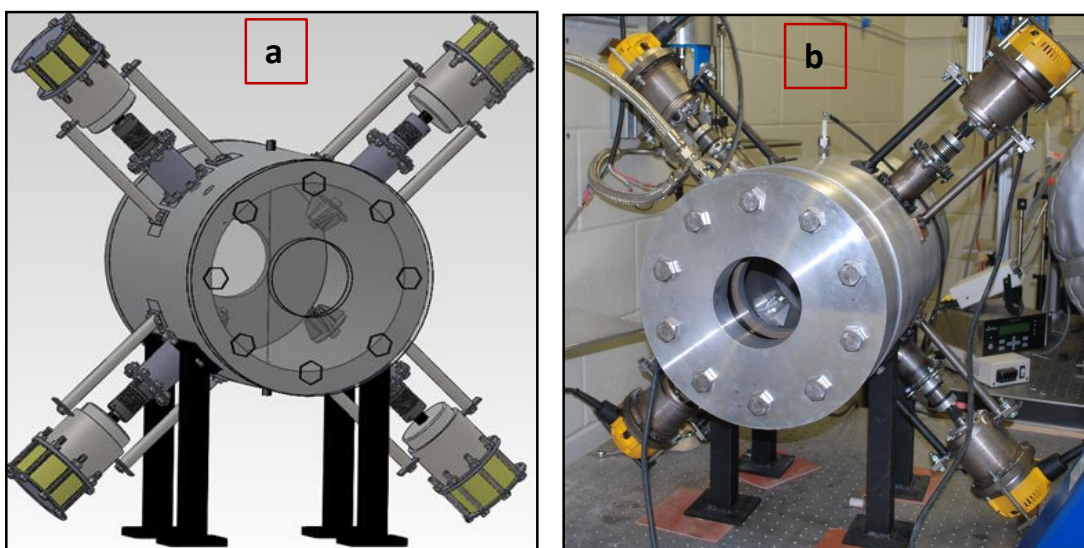


Figure 20. Fan-stirred flame speed vessel. (a) SOLIDWORKS model (b) photograph of the facility. Four fans were installed at the central circumference of the original laminar flame bomb to generate homogeneous and isotropic turbulence.

Shaft sealing is provided by means of custom-made lip seals made of PTFE-based polymer with molybdenum disulfide and fiberglass additives. They are encased in aluminum

casings which are press-fitted into prepared bores in the vessel. Unlike conventional lip seals, the sealing lips are not spring-energized, and this feature allows coolant-free operations even at very high surface speeds. High-speed angular contact bearings for the shafts are stacked inside cartridge housings that can be directly mounted onto the vessel. This setup is necessary to counteract the axial forces resulting from the combustion pressure rise and to add stiffness to the rotating shafts. Additionally, the bearings are sandwiched between grease-packed spacers (custom-designed) to prevent bearing-bearing contact when the shaft is turning, and also to serve as grease reservoirs for the bearings (Fig. 21). Each fan is turned by a 2.25-hp router motor whose rotational speeds can be varied between 8,000 and 24,000 rpm. The impeller shafts are connected to the motor shafts by means of flexible bellow couplings to compensate for any minor shaft misalignments.

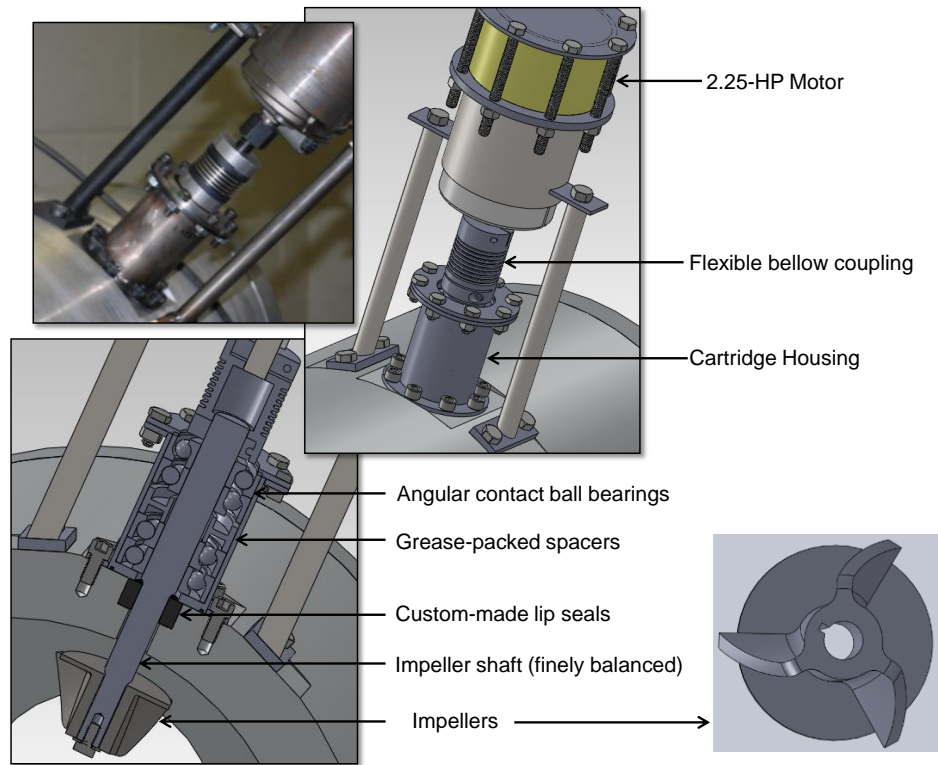


Figure 21. Detailed views of the impeller assembly. Various components namely, coupling, cartridge housing, bearings, spacers and seals are shown.

3. Experimental procedure and data analysis

Turbulent flame speed experiments follow the same basic procedure as the laminar flame speed experiment. A Z-type schlieren technique is used for the optical diagnostic, and the setup is described in detail in Krejci et al. [65]. All test mixtures are filled into the vessel and allowed to homogenize. The fans are activated prior to ignition, and the images are recorded upon ignition using the high-speed camera. Sample images from a typical turbulent flame speed experiment are shown in Fig. 22. The images are analyzed using a MATLAB-based code that was developed in-house. The program tracks the flame

boundary and estimates the area within the turbulent flame kernel for each frame (Fig. 22d). The enclosed area, $A(t)$, is then used to compute the radius of a circle with an equivalent area. This radius is defined as the schlieren radius, $r_{sch}(t) = \sqrt{A(t)/\pi}$.

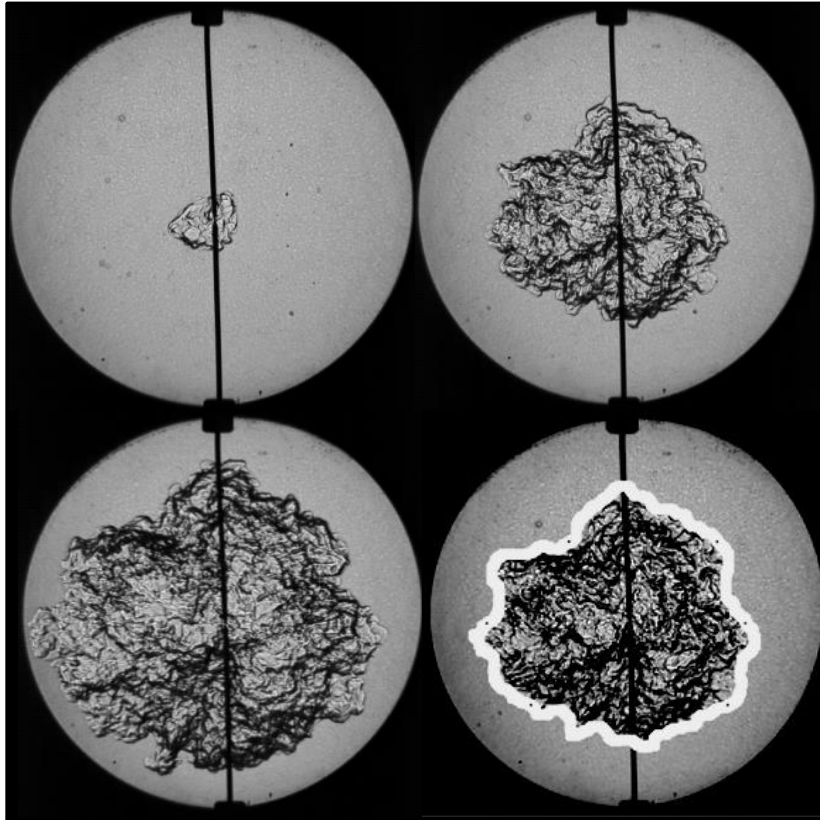


Figure 22. Sample images from a typical turbulent flame speed experiment. The image processing program estimates the flame radius by estimating the enclosed area within the kernel boundary (bottom-right), and calculating the radius of a circle with the same area; the white outline defining the flame edge is exaggerated in thickness in the last image for clarity.

Figure 23a shows the typical evolution of r_{sch} for stoichiometric methane in air at 1 atm, 298 K. Also included is the flame growth history of the same mixture for the laminar case. Whereas a perfectly linear slope that is indicative of constant flame speed (no flame acceleration) is evident in the latter, r_{sch} grows rapidly and nonlinearly for the turbulent cases (four repeats are shown in Fig. 23a), suggesting varying turbulent flame speeds with time. Also, the data density for the turbulent case was deliberately set to a higher value than typically used for laminar experiments by adjusting the framing rate of the camera. This improvement in temporal resolution reduces errors in the time-derivative estimates required for propagation rates. To determine the turbulent flame speed, the instantaneous turbulent flame speed is first computed by differentiating the radii time history using a central difference technique (Fig. 23b). A polynomial-regression-based smoothing filter (Savitzky-Golay) is used when computing the derivatives. This filter has been successfully applied to laminar flame speed measurements using high-frequency dynamic pressure traces without the loss of the experimental trend [67]. The turbulent flame speed, $S_{T,0.1}$, is then estimated by multiplying the instantaneous flame speed with the density ratio, (ρ_b/ρ_u) . The smallest flame size (diameter) that provides meaningful measurement (devoid of ignition-spark effects) is restricted to 2 cm (value determined based on noise in the derivatives at extremely small radii).

The propagation rate increases as the flame grows due to the fact that the developing kernel is affected by an increasing spectrum of velocity scales (symbols in Fig. 23c). Thus the spherically expanding flame bomb provides turbulent flame speeds over a range of

turbulence levels in a single shot. The effective turbulent intensities (u'_k) acting on the flame are also included in Fig 6c. A minimum of three trials is conducted for each test mixture, and a spline average of the displacement speeds over the range of u'_k is estimated from the repetitions to get a statistical estimate of the experimental scatter (Fig. 23d). Thus the spherically expanding flame bomb provides global displacement speeds over a range of turbulence levels. A majority of the databases from fan-stirred bombs report a single value for turbulent flame speed (at a particular radius) [4]. The choice of flame size is arbitrary and is typically a multiple of the integral length scale [15]. Also, the brush thickness is growing as the flame expands. A unified definition accounting for both these effects is yet to be determined. Displacement speeds measured herein are reported over the entire range of u'_k instead of at a particular flame size.

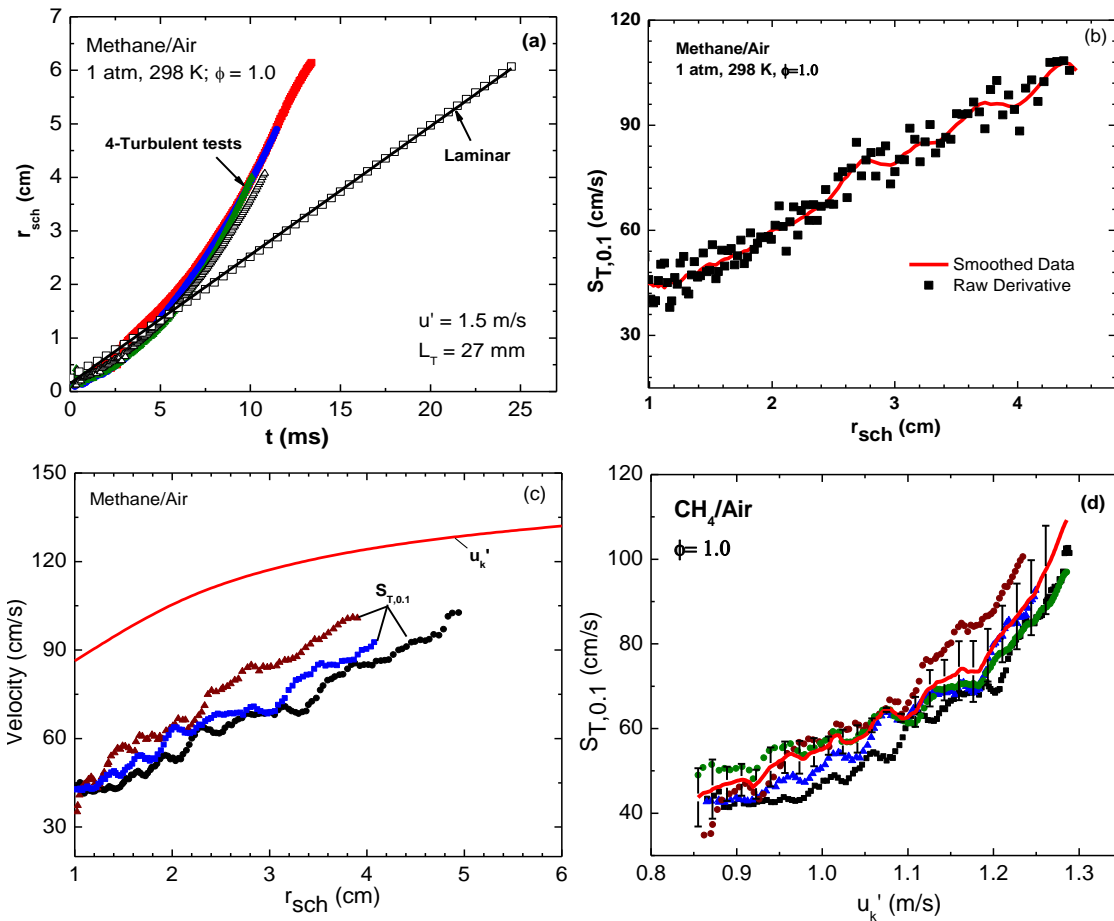


Figure 23. (a) Flame radius evolution for laminar and turbulent conditions. Near-linear flame growth is seen for the laminar case. The radii grow nonlinearly for the turbulent case due to flame acceleration. The radii from four different experiments collapse well, thus providing good repeatability. (b) Turbulent flame speeds with (curve) and without (symbols) the smoothing filter (only data from one of the trials are shown for clarity). (c) Global displacement speeds from three different separate trials (symbols). The flame speed increases as the flame grows as a result of the increasing effective turbulence intensities (u'_k) acting on it (shown as curve). (d) A good collapse of $S_{T,0.1}$ from four different trials can be seen at various u'_k . The solid curve is the spline average of the four measurements. Uncertainties associated with the average $S_{T,0.1}$ are also shown.

4. Measurement uncertainties

The measurement uncertainty for the laminar flame speed experiments of methane mixtures is on the order of 0.75 cm/s [64]. The experimental scatter is higher for the turbulent cases, so several repetitions of the same condition are needed to get a statistical estimate of the flame speeds. Figure 24 shows the histogram of the experimental scatter from three different realizations of each mixture. The scatter is unimodal following a normal distribution. The average scatter for methane was close to 10 cm/s (at 95% confidence-interval). Figure 25 compares the experimental scatter of methane measured herein with those from the Leeds group [68]. The maximum scatter (Δ) was 44 cm/s for the latter. Since the initial conditions were different, the data scatter was normalized by the respective peak flame speeds, $S_{T,max}$. This calculation yielded $\Delta/S_{T,max}$ of 0.13 and 0.30, respectively. Given the stochastic nature of these experiments, the observed data scatter here is in the same range as that estimated in other fan-stirred bombs. These values support the fact that though there is higher variability for the turbulent case, the scatter is still an order of magnitude lower than the flame speed estimates at each condition. It can thus be concluded that meaningful measurements of turbulent flame speeds are possible using the fan-stirred technique in the authors' laboratory.

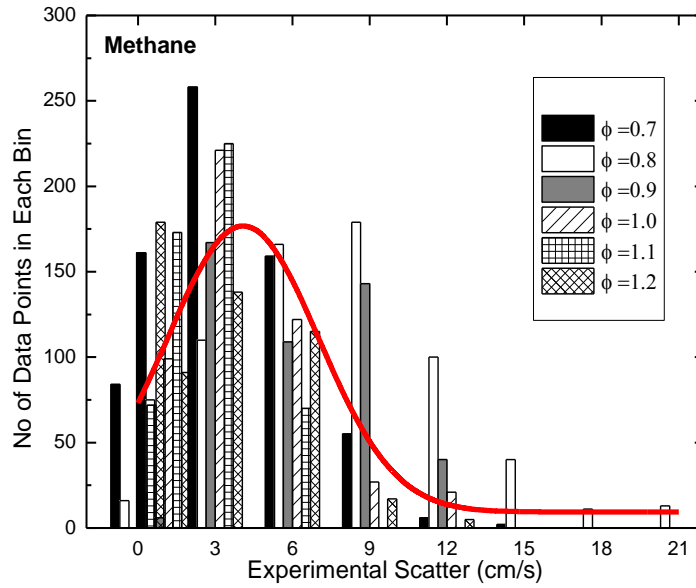


Figure 24. Histogram of the experimental scatter estimated from three different trials at each condition for methane-air mixtures at different equivalence ratios. The scatter is distributed near normally (shown as curve).

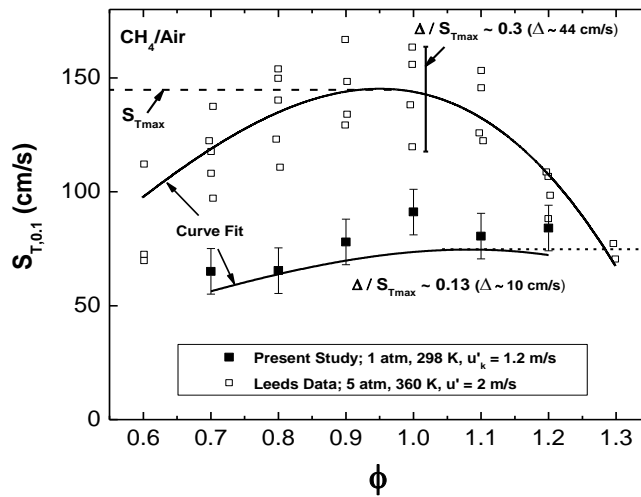


Figure 25. Experimental scatter for turbulent flame speed experiments. The scatter is estimated based on three different realizations of the same condition. Methane data from another fan-stirred bomb [68] are also shown. The scatter was normalized by the respective peak flame speeds, S_{Tmax} , for comparison.

5. Summary

An existing cylindrical laminar flame speed vessel was recently upgraded for conducting premixed turbulent combustion studies. Four fans were installed at the vessel central circumference, and the vessel features were described in detail. The impeller geometries were optimized to generate homogeneous and isotropic turbulence with no mean flow at the vessel center. Combustion is initiated by means of a spark at the center of the vessel, and the propagating flame ball is imaged using schlieren photography. The equivalent-circle-area method is used to estimate the flame radius. Global displacement speeds or turbulent flame speeds are then estimated by differentiating the radius history.

The radius history showed clear flame acceleration under turbulent conditions, while a near-linear radius growth (constant slope) was observed for the laminar case. Furthermore, the turbulent flame radii from different trials of the same mixture collapsed indicating good repeatability in the measurements. Following the concept of eddy-size restriction, the effective turbulent intensities (u'_k) that increased progressively (to the intensity levels generated by the fans) as the flame grew was estimated. Turbulent flame speeds were estimated as a function of u'_k . Each condition was repeated thrice, and the experimental scatter was on the same order as that reported in the literature (close to ± 10 cm/s here).

CHAPTER VI

RESULTS

Natural gas is the principal fuel for land-based, power-generation gas turbines. Furthermore, blending hydrogen with natural gas mixtures is of topical interest to combustor designers. These factors provide the necessary motivation to study the flame propagation characteristics of natural gas/hydrogen mixtures under engine-relevant conditions (turbulent). This chapter presents the results from turbulent flame speed experiments conducted in the newly developed facility. Flame speeds were derived using the procedure outlined in chapter V. Three repetitions of each mixture were carried out, and spline averages of the global displacement speeds were estimated as a function of the effective turbulent intensities acting on the growing kernel.

The objective of this study was to measure the turbulent displacement speeds of natural gas blends, and the study was divided into two parts. First, turbulent flame speeds of alkanes- methane, ethane and propane were measured. Since natural-gas composition varies depending on the fuel source, a natural-gas surrogate (NG2) has been utilized recently by the author's laboratory to aid chemical kinetics modeling using ignition delay time and laminar flame speed experiments [69]. Turbulent flame speeds of NG2 over a wide range of equivalence ratios ($\phi= 0.7-1.3$) are then presented. The second part of the study is related the effects of hydrogen addition to methane and NG2. Finally, a representative high-hydrogen-content syngas blend of 50:50 H₂:CO (by volume) was also

studied. The measurements were conducted at a fixed fan speed, and the relevant turbulent statistics attained in the fan-stirred bomb are summarized in Table 8.

Table 8. Various turbulence parameters for the turbulent flame speed experiments. The parameters were fixed for all mixtures from this study.

Turbulent Kinetic Energy, $\overline{q^2}$ [m^2/s^2]	6.6
Kinetic Energy Dissipation Rate, $\overline{\epsilon}$ [m^2/s^3]	59.7
Integral Scales	
Turbulent Intensity, u' (cm/s)	150
Integral Length Scale, L_T (mm)	27
Integral Time Scale, τ_ϵ (ms)	55
Taylor Microscales	
Taylor Length scale, λ [mm]	2.9
Taylor Reynolds Number (in air), Re_λ	277
Kolmogorov Scales	
Length scale, τ_k (ms)	0.5
Time Scale, η (mm)	0.1

1. Results

a. Pure-fuel flame speeds

Natural gas is a mixture of methane with significant amounts of higher-order hydrocarbons (>20%) [69]. As a first step towards understanding the combustion behavior of natural

gas, a systematic study on the burning properties of the parent hydrocarbons was conducted. Laminar flame speeds up to C3-alkanes have been measured at the author's laboratory, and have been validated against several chemical kinetics mechanisms elsewhere [64]. The AramcoMech 1.3 mechanism [66] was chosen as the kinetics model to estimate all laminar flame parameters for the present study. Turbulent displacement speeds for C1-C3 alkanes (in air) were measured in the newly developed fan-stirred bomb. Table 9 shows the various laminar flame parameters, namely, flame speed, $S_{L,u}$, and flame thickness, δ_L , for the different mixtures. Also, the three non-dimensional numbers used in the turbulent literature, Re , Da , and Ka , are also estimated for each mixture.

Figures 26 a-c show the radii history for the different fuels. Good repeatability is evident for different mixtures. The global displacement speed is the product of the radius growth rate and the density ratio. The variations in density ratios for the three fuels are shown in Fig. 26d. The density ratio shows a non-monotonic behavior with equivalence ratio with minima occurring at stoichiometric condition for all fuels. Additionally, the density ratio is higher for fuel-lean mixtures when compared to fuel-rich cases.

Prior to estimating the global displacement speeds, the effective intensity levels were computed for all mixtures. The global displacement speeds of the three fuels are plotted as functions of the effective intensity levels (Figs. 27 b-d). Only the spline-average (similar to Fig. 23d) at each condition is shown for clarity. The average scatter associated with each curve is around ± 10 cm/s. Clearly, all flames accelerate under turbulent

conditions. This behavior is a direct artifact of the developing nature of the flame geometry as explained earlier in Chapter III.

Table 9. Properties of hydrogen- and C1-C3 alkane-air mixtures studied herein

ϕ	$S_{L,u}$ (cm/s)	δ_L (μm)	Re	Da	Ka
CH₄/Air					
0.7	14.9	10.7	2552	25	2.02
0.8	22.7	7.0	2550	58	0.86
0.9	29.3	5.4	2547	97	0.52
1	34	4.7	2545	131	0.38
1.1	35.1	4.5	2543	140	0.36
1.2	32.6	4.9	2541	120	0.42
1.3	24.4	6.5	2538	67	0.75
C₂H₆/Air					
0.7	21.1	7.2	2660	53	0.98
1	37.6	4.0	2695	169	0.31
1.3	33.7	4.4	2730	138	0.38
C₃H₈/Air					
0.7	19.2	7.8	2699	44	1.18
1	36.8	4.0	2752	166	0.32
1.3	34.5	4.2	2805	148	0.36

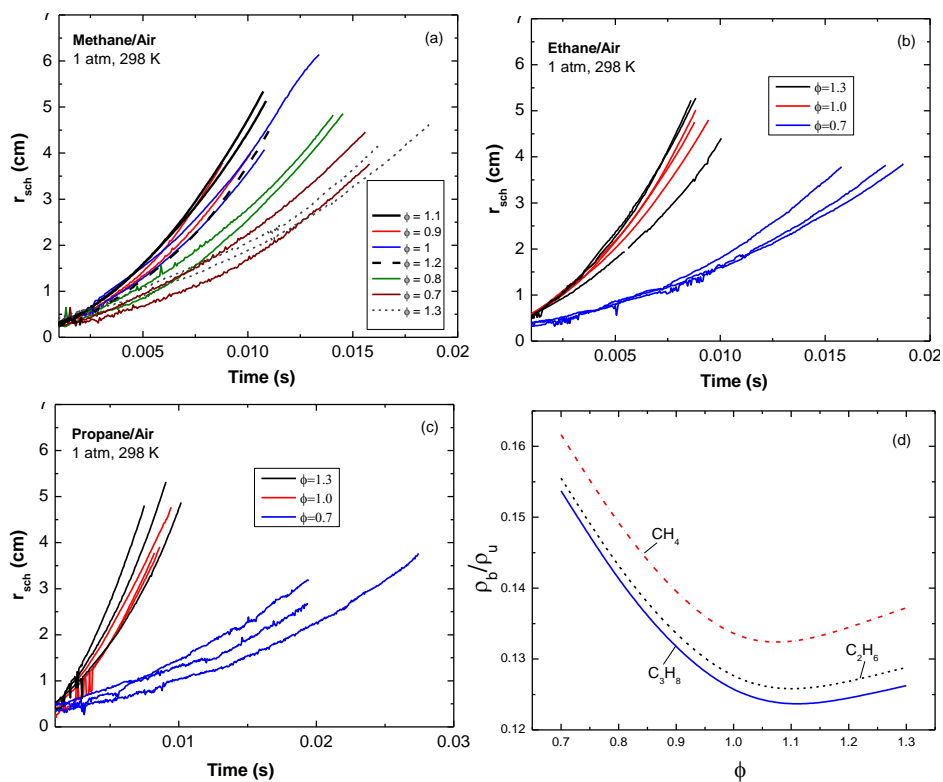


Figure 26. Turbulent radii-history (a) methane (b) ethane (c) propane. All three repeats are shown for (b) and (c). Only two repeats are shown for (a) for clarity. Good repeatability is evident for all the cases. (d) Density ratios of the mixtures at different equivalence ratios. The density ratios vary significantly from fuel-lean-to fuel-rich.

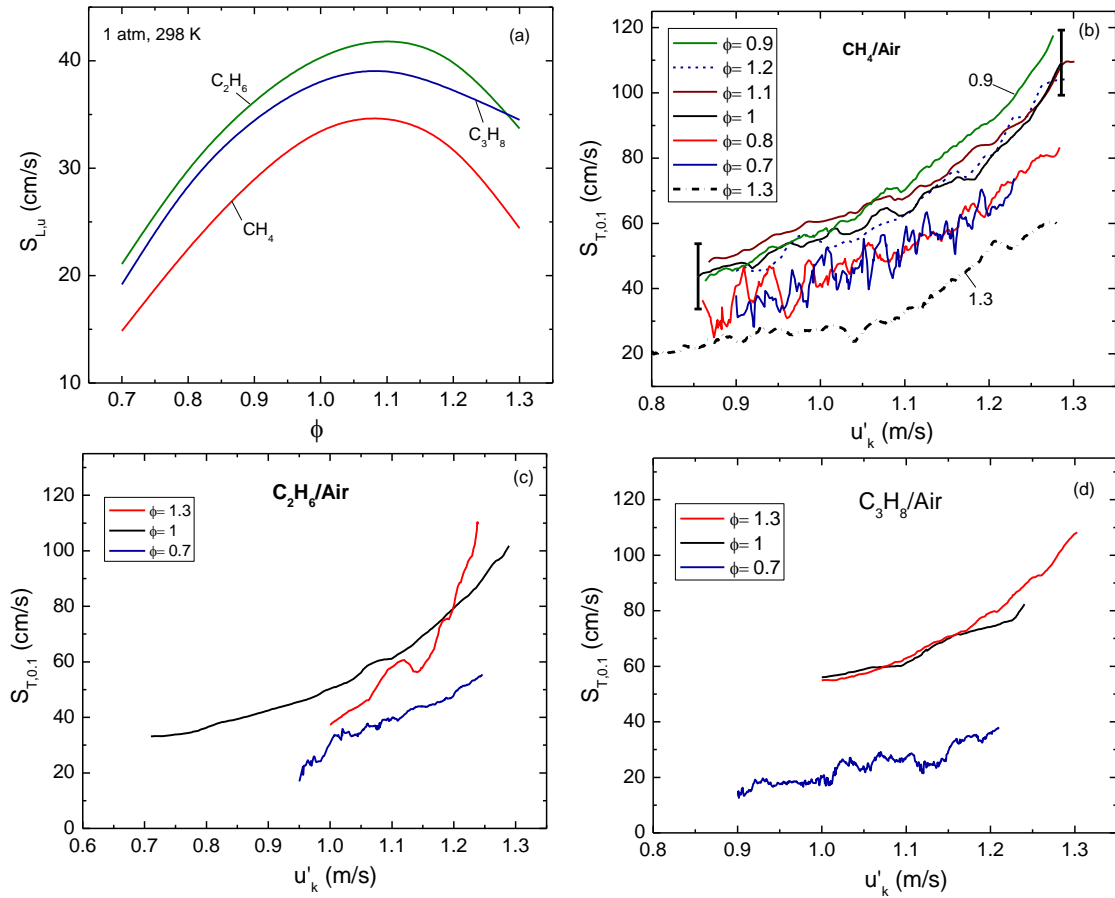


Figure 27. (a) Laminar flame speeds of alkane-air mixtures. Symbols are experimental data measurement at the author’s laboratory [70] and curves are kinetics model predictions. AramcoMech 1.3 [66] was used. Good agreement between the measurements and model predictions are seen for methane, though improvements are needed for ethane and propane. (b-d) Turbulent flame speeds of C1-C3 alkanes/air mixtures as a function of the effective turbulence intensity. The individual curves are the spline averages of three repetitions at each condition. The average scatter is estimated to be ± 10 cm/s.

b. Natural gas blends

Since natural gas composition varies depending on the fuel source, a natural gas surrogate (NG2: 81.25% CH₄ + 10% C₂H₆ + 5% C₃H₈ + 2.5% C₄H₁₀ + 1.25% n-C₅H₁₂ on a volumetric basis) has been utilized recently by the authors to aid chemical kinetics modeling using ignition delay times and laminar flame speed experiments ([69], [71]). Turbulent displacement speeds of NG2 in air were measured over a wide range of equivalence ratios (see Table 10). Figures 28 a,b show the radius growth profiles and displacement speeds of NG2 mixtures at turbulent conditions, respectively. Similar to the parent fuels, good agreement between several repeats is evident for NG2.

Table 10. Properties of NG2-air mixtures studied herein

ϕ	$S_{L,u}$ (cm/s)	δ_L (μm)	Re	Da	Ka
NG2/Air					
0.7	19.7	7.9	2598	45	1.14
0.8	27.4	5.7	2601	87	0.59
0.9	33.7	4.6	2605	132	0.39
1	37.8	4.1	2608	166	0.31
1.1	39.0	4.0	2611	177	0.29
1.2	36.3	4.3	2615	153	0.33
1.3	29.0	5.3	2618	98	0.52

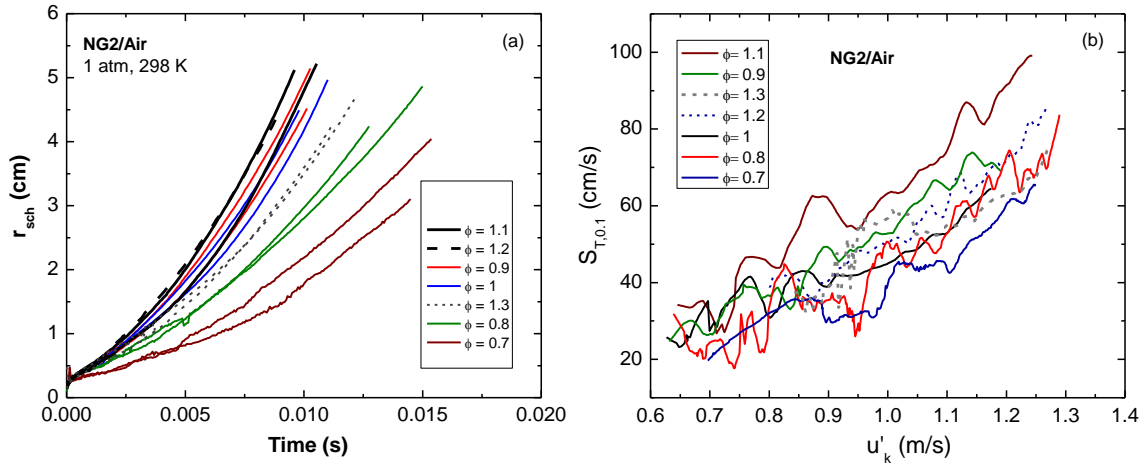


Figure 28. (a) Turbulent radius growth for NG2 mixtures. (b) Displacement speeds of NG2/air premixtures.

c. Effects of hydrogen addition on the displacement speeds

Blending hydrogen and hydrocarbon-based fuels is of immense interest to gas-turbine combustor designers. Such a hybrid mixture has the advantage of higher laminar flame speeds at ultra-lean conditions that are outside the lean-flammability limits of hydrocarbons. However, the propensity to auto-ignite or to flashback increases as the hydrogen fraction in the blend is increased due to the augmented laminar flame speeds (and hence turbulent flame speeds). These factors provide the motivation to study the combustion characteristics of high-hydrogen-content blends of hydrocarbon mixtures under turbulent conditions.

The primary mechanism of laminar flame speed augmentation of straight-chain alkanes with hydrogen addition is predominantly a kinetic effect through increased concentration of the highly diffusive hydrogen radical [72]. A mechanistic and experimental study on the improved laminar speeds with hydrogen addition to NG2 and CH₄ was conducted by the author's laboratory, and can be found elsewhere [73]. In that study, laminar flame speeds of methane/hydrogen and NG2/hydrogen mixtures were measured at elevated pressures and temperatures. The same problem is revisited herein, but under turbulent conditions. First, displacement speeds of pure hydrogen were measured. A 50:50 by volume blend of CH₄:H₂ was then studied. Finally, the effects of hydrogen addition on the turbulent flame speeds of NG2 (25/75 and 50/50 (by volume) blends of H₂/NG2) were investigated.

The laminar flame properties of the various hydrogen-based mixtures are shown in Table 11. Turbulent flame radii evolutions for pure hydrogen and H₂-based blends are shown in Fig. 29. Excellent repeatability is evident for all mixtures, and the results are consistent with the trends observed earlier with the pure alkanes. The global displacement speeds were computed and are shown in Fig. 30. These flame speeds are higher than the laminar flame speeds for all mixtures, thus highlighting the promoting effect of turbulence on the flame propagation at least at the intensity levels attained herein. Extension of this study to higher intensity levels and at different length scales is proposed for the future.

Table 11. Properties of blends containing hydrogen

ϕ	$S_{L,u}$ (cm/s)	δ_L (μm)	Re	Da	Ka
H₂/Air					
0.5	53.6	3.5	2169	277	0.17
0.6	89.2	2.2	2106	745	0.06
0.7	124.8	1.6	2047	1417	0.03
0.8	157.7	1.3	1993	2203	0.02
0.9	186.6	1.1	1942	3005	0.01
1	211.4	1.0	1893	3759	0.01
50:50 CH₄:H₂					
0.5	7.6	21.5	2470	6	7.75
0.6	17.6	9.4	2451	34	1.47
0.7	28.8	5.8	2434	90	0.55
0.8	39.8	4.2	2417	170	0.29
0.9	48.9	3.4	2400	255	0.19
1	55.4	3.1	2384	325	0.15
50:50 H₂:CO (Syngas)					
0.5	28.7	5.9	2373	87	0.56
0.6	45.8	3.8	2341	219	0.22
0.7	63.7	2.8	2312	416	0.12
0.8	80.9	2.2	2285	664	0.07
0.9	97.1	1.8	2259	946	0.05
1	111.9	1.6	2234	1243	0.04
75:25 NG₂:H₂					
0.7	22.7	7.0	2556	58	0.87
1	43.4	3.7	2549	214	0.24
1.3	35.4	4.5	2543	141	0.36
50:50 NG₂:H₂					
0.7	28.6	5.7	2488	91	0.55
1	53.9	3.1	2456	317	0.16
1.3	48.2	3.5	2427	250	0.20

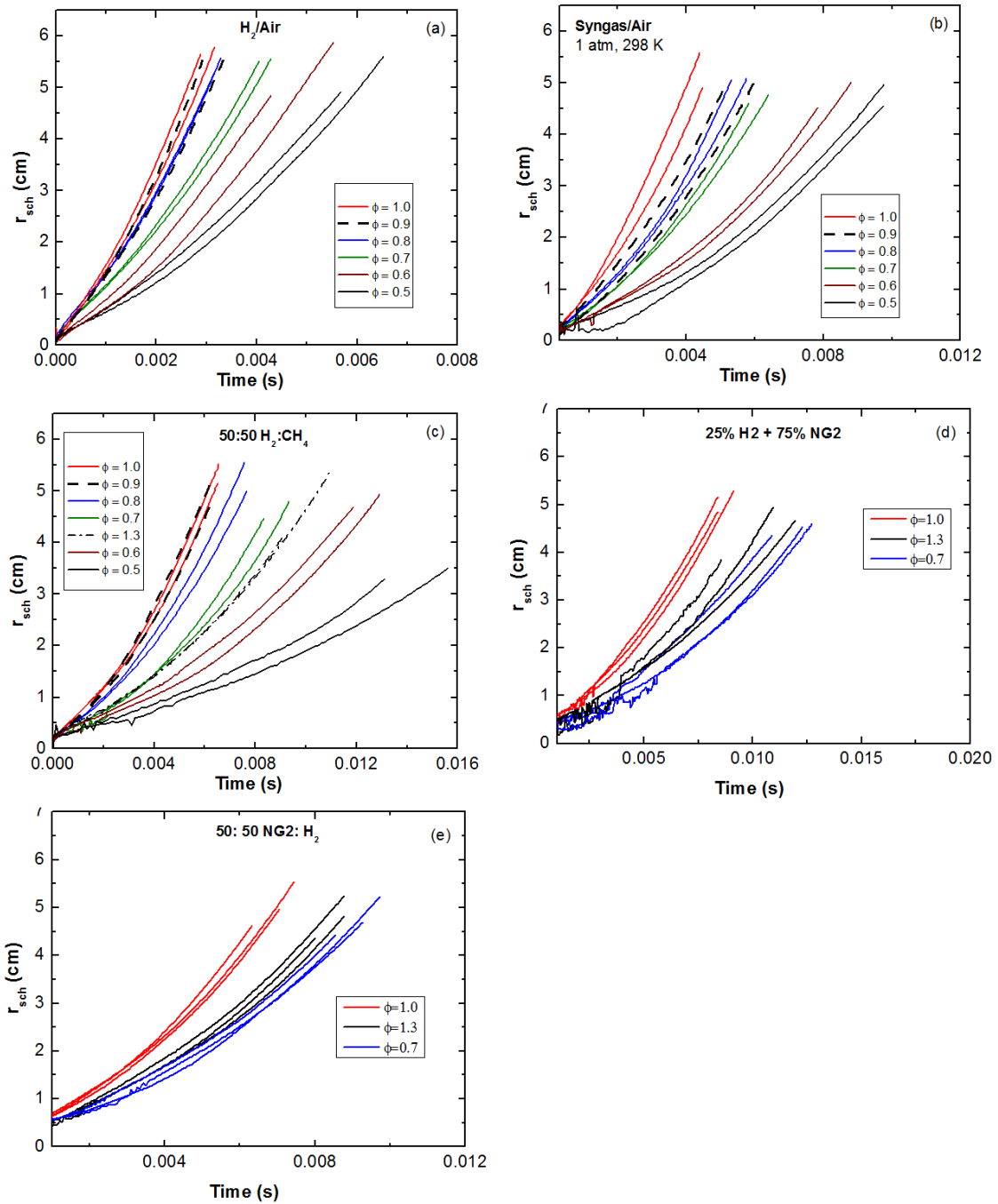


Figure 29. Turbulent flame radii evolution for (a) H₂/air (b) Syngas (50:50 H₂:CO) (c) 50:50 H₂:CH₄ (d) 75:25 NG₂: H₂ (e) 50:50 NG₂: H₂. Three repeats were conducted for each mixture. Only two repeats are shown in (a) - (c) for visual clarity. Similar to pure-alkanes and NG₂, good repeatability of the turbulent radii profiles are observed.

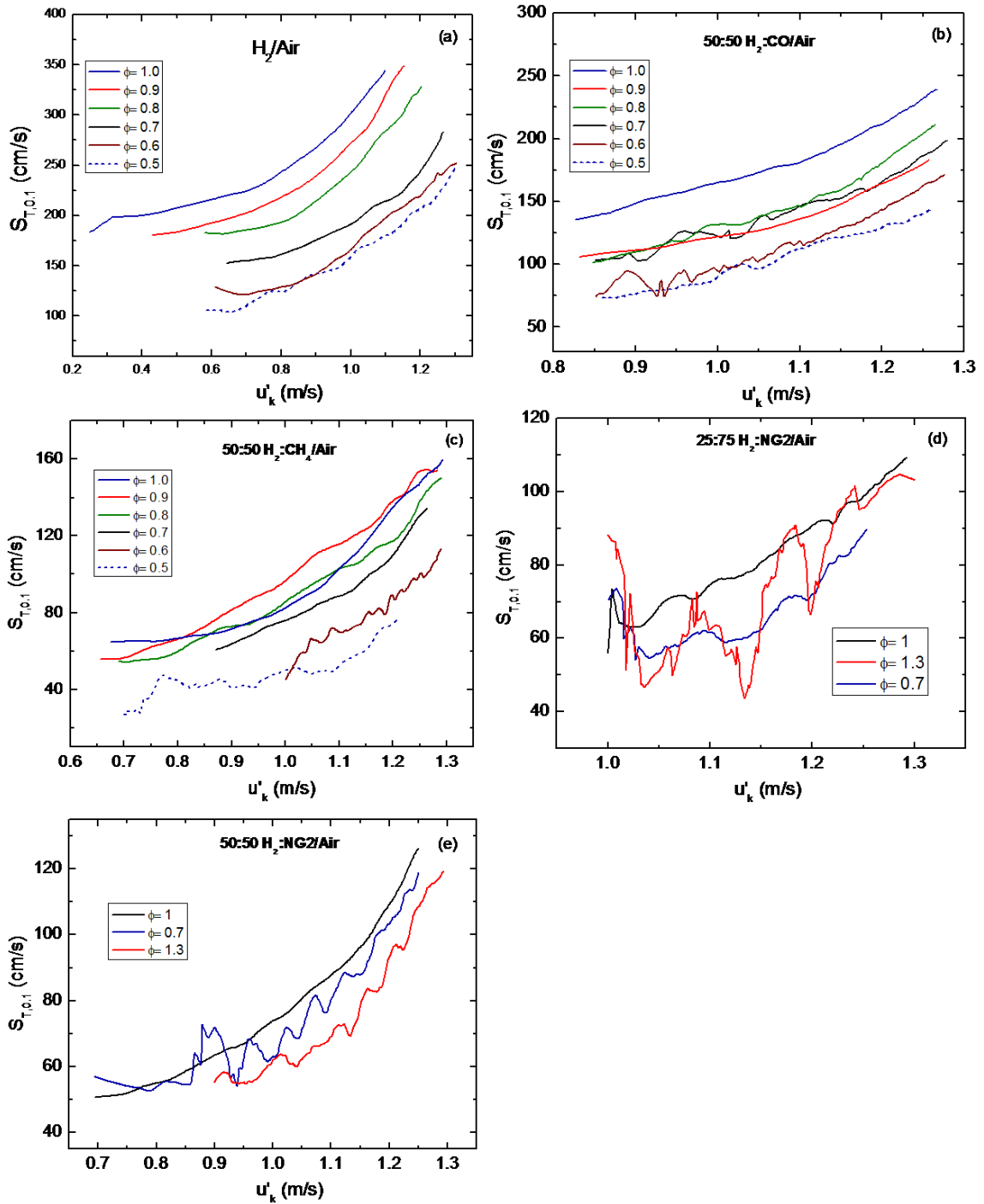


Figure 30. Global displacement speeds of (a) H_2/air (b) Syngas (50:50 $H_2:CO$) (c) 50:50 $H_2:CH_4$ (d) 75:25 $NG_2: H_2$ (e) 50:50 $NG_2: H_2$. The curves are cubic-spline averages of three repetitions.

2. Discussion

a. Borghi diagram

The measurement conditions explored in this study are plotted on a Borghi diagram (Fig. 31). A majority of the mixtures studied herein belong to the corrugated flamelet regime. Since the turbulence parameters were fixed, the different alkane blends follow a near-constant Reynolds number (Re) of 2500 ($Re = u' L_T / \nu$; ν is the kinematic viscosity and does not vary appreciably for alkane blends). Slightly lower Re was estimated for pure-hydrogen mixtures. Furthermore, the overall shapes of the flame were noticeably different for the various regimes. For the laminar case, the flame is near-spherical with a wrinkle-free surface (flame instabilities not considered here). The flame is still spherical although large-cell wrinkles appear on the surface in the wrinkled flamelet regime. In the corrugated flamelet regime, the flame shape starts to deviate from being spherical and is characterized by lamella-like corrugations. Finer structures appear in the thin reaction zone, and the sphericity of the growing flame ball is no longer observed. Chaudhuri et al. [74] measured turbulent flame speeds at elevated pressures in a fan-stirred bomb and concluded that the Markstein diffusivity also affects the cell size of the turbulent wrinkles. Dedicated efforts towards determining the correlation between the thermo-physical properties of the flame and the size of the turbulence-induced flame wrinkle is proposed for future work.

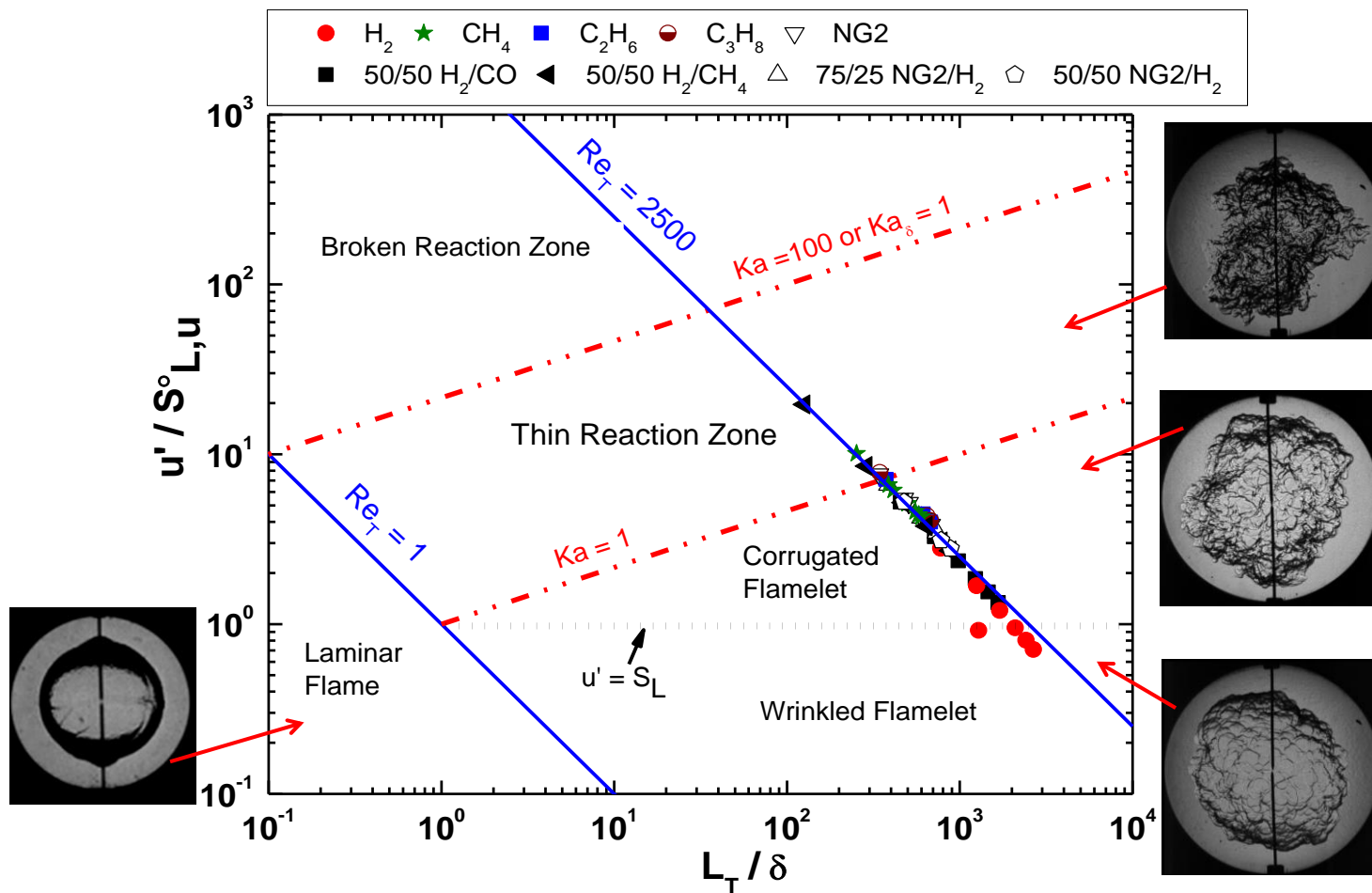


Figure 31. Borghi diagram showing the different regimes of turbulent flame propagation. Flame morphologies varied markedly for each regime (images shown as insets).

b. NG2-alkane comparison

Since NG2 is predominately methane, it is only logical to compare their displacement speeds. As evident from Figs. 32 a-g, the flame speeds of NG2 and methane are in close agreement (experimental scatter is ± 10 cm/s) with each other for all equivalence ratios. Close agreement between the laminar flame speeds of NG2 and CH₄ were observed when fuel lean, and noticeable differences arose only under fuel-rich conditions with NG2 characterized by higher flame speeds [69]. The same trends are preserved for the displacement speeds measured herein. This consensus between the two fuels serves as a good benchmark for validating the experimental procedure developed herein.

Figures 33 a-c compare the displacement speeds of NG2 with the parent hydrocarbons for fuel-lean, stoichiometric, and fuel-rich conditions, respectively. For $\phi=0.7$, the turbulent flame speeds of methane are higher than ethane and propane, with propane being the lowest. On the contrary, rich propane and ethane are characterized by higher displacement speeds when compared to rich methane. These trends can be attributed to the impact of Lewis number on turbulent flame propagation. Lewis number is defined as the ratio of the mixture thermal diffusivity to the mass diffusivity of the deficient species into the diluent. Non-unity Lewis numbers may enhance or negatively affect the local burning rate. When $Le < 1$ ($Le > 1$), the local burning velocity is enhanced (reduced) due to reduced (enhanced) heat loss in the positively curved sections [75]. The probability of finding positively stretched, curved flamelets (convex towards unburnt gas) is higher in a premixed turbulent reacting flow since the mean strain rate and mean curvature are both positive at the leading

edge of the flame [5]. Such stretching of laminar flamelets by the action of turbulent eddies results in significant deviation of the local burning rate from the unstretched laminar flame speed. As a result, for mixtures with $Le < 1$, the displacement speeds are not only augmented by increased flamelet surface area, but also by the increased local burning rate. These effects explain the higher turbulent flame speeds of lean methane (or rich ethane and rich propane) which is characterized by $Le < 1$. Such trends have been documented by Weiß et al. [39], Kido et al. [76], Karpov and Sevrin (see references in [5]) all in fan-stirred bombs, and in Bunsen burner experiments of lean-hydrogen/air mixtures [77] and in DNS investigations [78].

Furthermore, the effects of hydrogen addition on the turbulent displacement speeds are compared for methane and NG2 in Fig. 34. No noticeable difference in the laminar flame speeds (Fig. 34a) can be observed between CH_4 and NG2 for the high-hydrogen-content (50% H_2). Similar trends are evident for the turbulent flames as well. Also, it should be pointed out that spherical flames were not observed for the fuel-rich NG2 mixture with 25% H_2 , and resulted in larger experimental scatter relative to other mixtures investigated herein.

The results presented herein have significant implications for gas-turbine combustion which operate in lean, premixed configurations. Turbulent flame speeds of NG2 and CH_4 were identical for the lean mixtures despite the fact that the former contains large amounts of heavier hydrocarbons. Though auto-ignition times are affected by C_2+ addition ([69],

[71]), laminar and turbulent flame speeds seem to be insensitive to these additives at the levels of turbulent intensities attained herein.

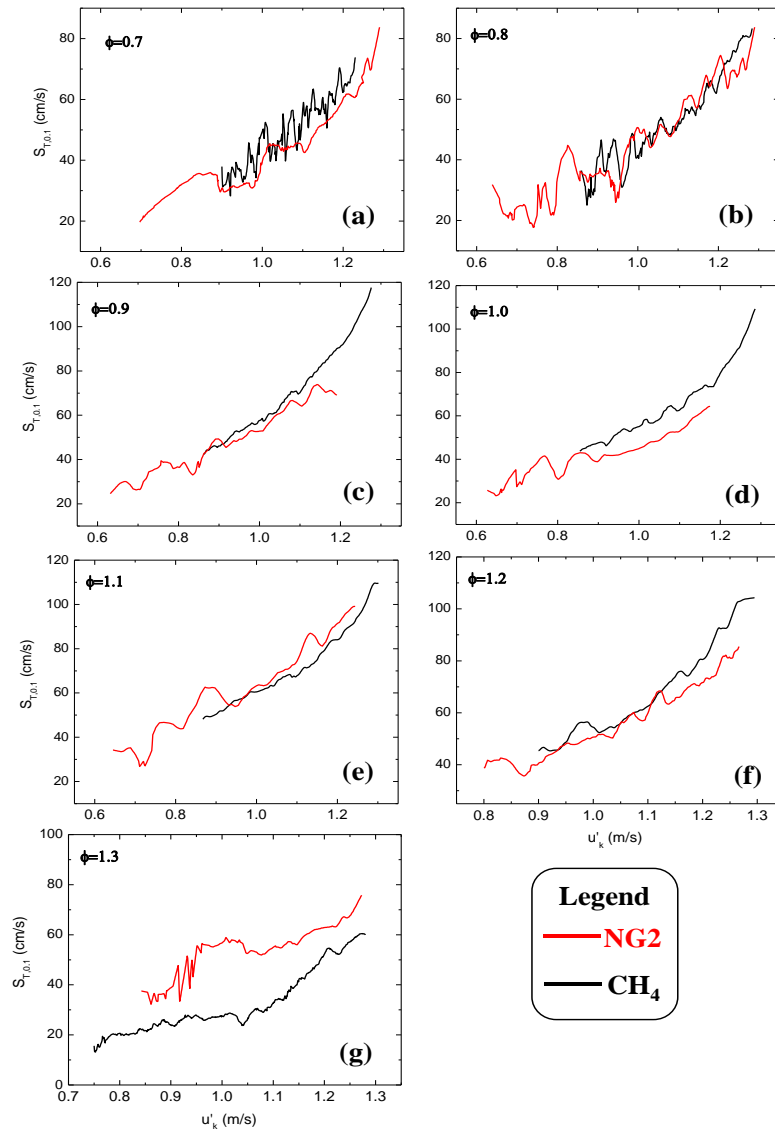


Figure 32. Comparison of turbulent flame speeds of NG2 and methane mixtures. The flame speeds of both fuels are similar for a wide range of equivalence ratio studied herein thus providing a good validation of the flame bomb.

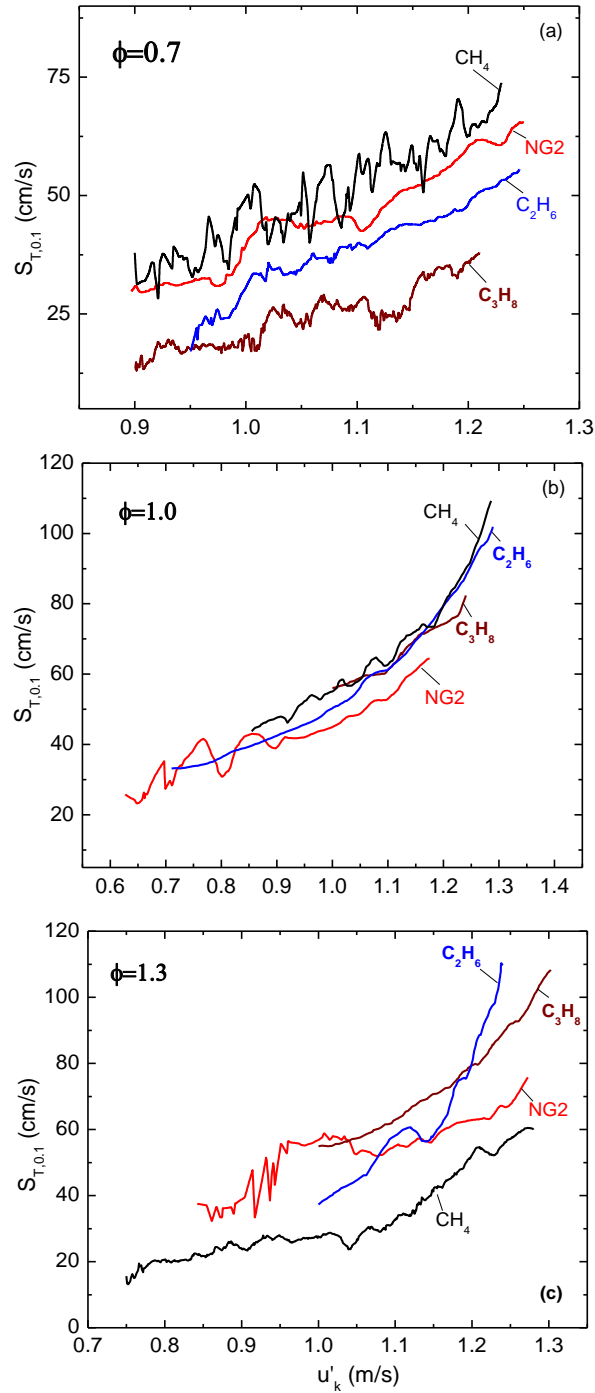


Figure 33. Displacement speeds of alkanes and NG2 at (a) fuel-lean (b) stoichiometric (c) fuel-rich conditions. Mixtures with $Le > 1$ have lower turbulent flame speeds (lean-ethane and -propane, and rich-methane) due to reduction in the stretched laminar flame speeds from the unstretched values.

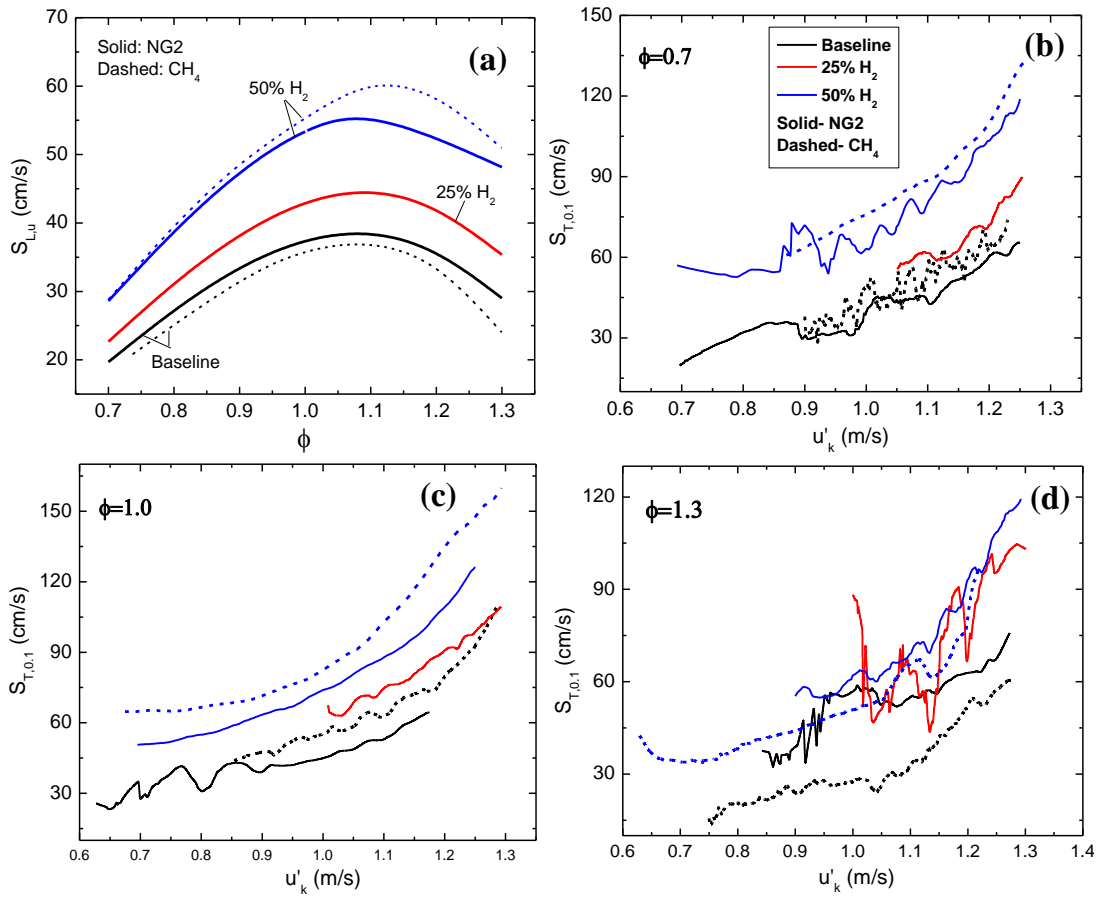


Figure 34. (a) Laminar flame speeds (curves are model predictions) of NG2 and CH₄ with varying levels of H₂. (b) Turbulent displacement speed for these mixtures measured herein. u'_k was estimated separately for each fuel. No appreciable difference is observed between the high-hydrogen-content mixtures of methane and NG2.

CHAPTER VII

CONCLUSIONS

1. Summary

This study focused on the design and development of a fan-stirred flame speed vessel for the measurements of global displacement speeds. To that effect, an existing cylindrical laminar flame speed vessel was modified, and four high-speed mixing impellers were installed in a central-symmetric arrangement at the vessel center. The fan designs were optimized using PIV in a Plexiglas model (1:1 scale) of the vessel. The fans were radial-type blades, and they generated near-homogeneous and -isotropic turbulence (HIT) with negligible mean flow ($< 10\% u'$). The flow fields were precisely quantified, and HIT conditions were verified using spatial homogeneity and isotropy maps, two-point correlations and energy spectra relations. Also, the ability to independently vary the integral length scale and turbulence intensity was identified. The intensity level changed with the rotational speeds of the fan, and the length scale decreased when blades with higher pitch angle was used.

The fan-stirred vessel was constructed to the desired specifications. Bearing-arrangements and shaft sealing were appropriately selected to withstand post-combustion conditions. Schlieren imaging was used in conjunction with a high-speed camera to capture the flame event. Flame propagation was a constant-pressure process for the usable part of the experiment (until the flame edge reached the window diameter). The equivalent-circle-

area method was used to determine the flame radius. The displacement speeds were estimated by differentiating the radius histories. The measured flame speeds increased as the flames expanded due to their accelerating nature. Effective intensity levels experienced by the flame at different stages were estimated by integrating the non-dimensional power-spectral-density function. Each experimental condition was repeated three times to estimate the scatter in the measurements. The average scatter was around ± 10 cm/s.

Turbulent flame speeds of alkanes and alkane-hydrogen blends were measured. Methane, ethane and propane were studied over wide range of equivalence ratios. Non-unity Lewis numbers affected turbulent flame propagation rates. Particularly, displacement speeds were noticeably higher for mixtures with $Le < 1$ than those with $Le > 1$ for the same equivalence ratio. Subsequently, lean methane was characterized with higher turbulent flame speeds than ethane and propane. Whereas, methane had lower flame speeds when compared to ethane and propane under fuel-rich conditions.

A natural gas surrogate (NG2: 81.25% CH_4 + 10% C_2H_6 + 5% C_3H_8 + 2.5% C_4H_{10} + 1.25% $n-C_5H_{12}$; on a volumetric basis) was also studied. The flame speeds of NG2 and methane were nearly identical thus validating the developed experimental technique. The effects of hydrogen addition to methane, NG2 were also investigated. Displacement speeds increased for both fuels with hydrogen addition, and the trends were consistent with those observed with the laminar flame speeds of the fuel blends. Additionally, displacement speeds of syngas blends (50:50 H_2 : CO) were also measured over a wide

range of lean-equivalence ratios. Displacement speeds of syngas mixtures increased as the laminar flame speed increased (from lean approaching stoichiometric condition).

2. Recommendations for future efforts

The preliminary measurements obtained herein are encouraging and serve as a good basis for a more-comprehensive database. A few recommendations for future work include,

1. Extension to higher intensity levels- gas turbines combustors typically operate at $Re \sim 10^4$. Such conditions can be achieved by increasing the intensity levels. High values of u'/S_L in flame bombs are associated with convection of the ignition-spark (and hence the growing kernel) away from the center of the imaging plane. Upgrading the current ignition system to a more-powerful one can help mitigate this problem.
2. Length scale effects- an assessment of the influence of L_T on the displacement speeds should be considered to aid in eliminating geometric dependencies from the measurements. Use of impellers with different pitch angles is suggested.
3. Verification of u'_k - Weiß et al. [39] and Akkerman et al. [78] suggested that the effective turbulent intensity acting on the flame is larger than those estimated by Bradley et al. [30]. Akkerman et al. [78] proposed that the averaging should be performed over the flame-size (radial) instead of assigning a single value of mean velocity for the entire domain when determining the RMS velocity generated by the fans. Validation of the velocity fields using laser Doppler velocimetry inside the fan-stirred is recommended.

4. Syngas-type mixtures- this study mainly focused on blending hydrogen with alkanes. High-hydrogen-content syngas-type fuels are being used increasingly in premixed gas turbines. It has been demonstrated here that the current instrumentation (camera) is sufficient to successfully capture pure-hydrogen and a generic HHC syngas blend. Studies on syngas-type mixtures with impurities such as ammonia and hydrogen sulphide are scarce, and it would be worthwhile to investigate the turbulent combustion characteristics of such candidate fuels.

REFERENCES

- [1] D. Bradley, M.Z. Haq, R.A. Hicks, T. Kitagawa, M. Lawes, C.G.W. Sheppard, R. Woolley, *Combust. Flame* 133 (2003) 415- 430.
- [2] S. Chaudhuri, F. Wu, D. Zhu, C.K. Law, *Phys. Rev. Lett.* 108 (2012) 044503-1-044503-5.
- [3] A.N. Lipatnikov, J. Chomiak, *Prog. Energ. Combust.* 31 (2005) 1-73.
- [4] A.N. Lipatnikov, J. Chomiak, *Prog. Energ. Combust.* 28 (2002) 1-74.
- [5] A.N. Lipatnikov, *Fundamentals of Premixed Turbulent Combustion*, CRC Press, Boca Raton, FL, 2012.
- [6] G.K. Batchelor, *Proc. Math. Phys. Eng. Sci.* 213 (1952) 349- 366.
- [7] H. Kobayashi, T. Tamura, K. Maruta, T. Niioka, F.A. Williams, *Proc. Combust. Inst.* 26 (1996) 389- 396.
- [8] C.C. Liu, S.S. Shy, M.W. Peng, C.W. Chiu, Y.C. Dong, *Combust. Flame* 159 (2012) 2608-2619.
- [9] J. de Vries. A Study on Spherical Expanding Flame Speeds of Methane, Ethane and Methane/Ethane Mixtures at Elevated Pressures. PhD Dissertation, Texas A&M University, 2009.
- [10] D. Bradley, P.H. Gaskell, X.J. Gu, *Combust. Flame* 104 (1996) 176- 198.
- [11] B. Renou, A. Mura, E. Samson, A. Boukhalfa, *Combust. Sci. Technol.* 174 (2002) 143- 179.
- [12] P. Venkateswaran, A. Marshall, D.H. Shin, D. Noble D, J. Seitzman, T. Lieuwen, *Combust. Flame* 158 (2011) 1602- 1614.
- [13] H. Kobayashi, H. Hagiwara, H. Kaneko, Y. Ogami, *Proc. Combust. Inst.* 31 (2007) 1451- 1458.
- [14] R.K. Cheng, I.G. Shepherd, *Combust. Flame* 85 (1991) 7- 26.
- [15] D. Bradley, M. Lawes, M.S. Mansour, *Combust. Flame* 158 (2011) 123- 138.
- [16] J.F. Driscoll, *Prog. Energ. Combust.* 34 (2008) 91- 134.
- [17] N. Peters, *J. Fluid Mech.* 384 (1999) 107- 132.

- [18] A. Pocheau, *Europhys. Lett.* 20 (1992) 401- 406.
- [19] R. Borghi, *On the Structure and Morphology of Turbulent Premixed Flames, Recent Advances in the Aerospace Science*, Plenum, New York, 1985, p. 117-138.
- [20] J. Savre, H. Carlsson, X.S. Bai, *Flow Turbul. Combust.* 90 (2013) 325- 341.
- [21] N. Peters, *Lecture notes on Combustion Theory- CEFRC-Princeton Summer School, Princeton, NJ. June 27- July 3 (2010).*
- [22] S. Chaudhuri, V. Akkerman, C.K. Law, *Phys. Rev. E* 84 (2011) 025322-1-026322-14.
- [23] T. Poinso, D. Veynante, *Theoretical and Numerical Combustion (2nd Edition)*, R.T. Edwards Inc., U.S.A., 2005.
- [24] M.P. Burke, Z. Chen, Y. Ju, F.L. Dryer, *Combust. Flame* 156 (4) (2009) 771-779.
- [25] M.R. Harker, T. Hattrell, M. Lawes, C.G.W Sheppard, N. Tripathi, R. Woolley, *Combust. Sci. Technol.* 184 (2012) 1818-1837.
- [26] W.M.T. Ashurst, *Combust. Sci. Technol.* 104 (1995) 19-32.
- [27] N. Peters, H. Wenzel, F.A. Williams, *Proc. Combust. Inst.* 28 (2000) 235- 243.
- [28] B. Leisenheimer, W. Leuckel, *Combust. Sci. Technol.* 118 (1996) 147- 164.
- [29] R.G. Abdel-Gayed, D. Bradley, M. Lawes, *Proc. Math. Phys. Eng. Sci.* 414 (1987) 389- 413.
- [30] D. Bradley, M. Lawes, M.S. Mansour, *Proc. Combust. Inst.* 32 (2009) 1587- 1593.
- [31] W. Hwang, J.K. Eaton, *Exp. Fluids* 36 (2004) 444- 454.
- [32] T. Gotoh, D. Fukayama, T. Nakano, *Phys. Fluids* 14 (2002) 1065- 1081.
- [33] T. Fallon, C.B. Rogers, *Exp. Fluids* 33 (2002) 233- 241.
- [34] L. Sabban, R. Van Hout, *J Aerosol Sci.* 42 (2011) 867- 882.
- [35] M. Birouk, C. Chauveau, B. Sarh, A. Quilgars, I. Gökalp, *Combust. Sci. Technol.* 113-114 (1996) 413- 428.
- [36] R.G. Abdel-Gayed, K.J. Al-Khishali, D. Bradley, *Proc. Math. Phys. Eng. Sci.* 391 (1984) 393- 414.

- [37] M. Birouk, B. Sarh, I. Gökalp, *Flow Turbul. Combust.* 70 (2003) 325- 348.
- [38] E.S. Semenov, *Combust. Explo. Shock* 1 (1965) 57- 62.
- [39] M. Weiß, N. Zarzalis, R. Suntz, *Combust. Flame* 154 (2008) 671- 691.
- [40] S. Kwon. *Premixed Hydrogen/Air Flames in Isotropic Turbulence*. PhD Dissertation, University of Michigan, 1990.
- [41] T.D. Fansler, E.G. Groff, *Combust. Flame* 80 (1990) 350- 354.
- [42] S. Kwon, M.S. Wu, J.F. Driscoll, G.M. Faeth, *Combust. Flame* 88 (1992) 221- 238.
- [43] S.S. Shy, W.K. I, M.L. Lin, *Exp. Therm. Fluid Sci.* 20 (2000) 105- 114.
- [44] R. Liu, D.S-K. Ting, G.W. Rankin, *Exp. Therm. Fluid Sci.* 28 (2004) 307- 316.
- [45] R. Liu R, D.S-K. Ting, M.D. Checkel, *Exp. Therm. Fluid Sci.* 31 (2007) 897- 908.
- [46] T. Brutscher, N. Zarzalis, H. Bockhorn, *Proc. Combust. Inst.* 29 (2002) 1825- 1832.
- [47] A. Smallbone, K. Tsuneyoshi, T. Kitagawa, *J Therm. Sci. Tech. - JPN.* 1 (2006) 31- 41.
- [48] M. Nakahara M, H. Kido H, *AIAA J.* 46 (2008) 1569- 1575.
- [49] C.C. Liu, S.S. Shy, H.C. Chen, M.W. Peng, *Proc. Combust. Inst.* 33 (2011) 1293- 1299.
- [50] S.B. Pope, *Turbulent flows*, Cambridge University Press, Cambridge, U.K., 2000.
- [51] P. Doron, L. Bertuccioli, J. Katz, T.R. Osborn, *J Phys. Oceanogr.* 31 (2001) 2108- 2134.
- [52] J.M. Foucault, M. Stanislas, *Meas. Sci. Technol.* 13 (2002) 1058- 1071.
- [53] P. Saarenrinne, M. Piirto, *Exp. Fluids Suppl.* (2000) S300–S307.
- [54] J. de Jong, L. Cao, S.H. Woodward, J.P.L.C. Salazar, L.R. Collins, H. Meng, *Exp. Fluids* 46 (2009) 499- 515.
- [55] C. Goepfert, J.L. Marié, D. Chareyron, M. Lance, *Exp. Fluids* 48 (2010) 809- 822.
- [56] K.R. Sreenivasan, *Phys. Fluids* 10 (1998) 528- 529.

- [57] P. Burattini, P. Lavoie, R.A. Antonia, *Phys. Fluids* 17 (2005) 098103-1- 098103-4.
- [58] W.J.T Bos, L. Shao, J.P. Bertoglio, *Phys. Fluids* 19 (2007) 045101-1- 045101-8.
- [59] W.W. Kim, S. Menon, H.C. Mongia, *Combust. Sci. Technol.* 143 (1999) 25- 62.
- [60] R.C. Aldredge, *Int. Commun. Heat Mass* 24 (1997) 565- 568.
- [61] F.E. Ames, R.J. Moffat, Effects of Simulated Combustor Turbulence on Boundary Layer Heat Transfer. Heat transfer in turbulent flow: AIAA/ASME Thermo physics and Heat Transfer Conference, Washington, D.C., June 18-20 (1990).
- [62] R.W. Moss, The Effects of Turbulence Length Scale on Heat Transfer. PhD Dissertation, University of Oxford, U.K., 1992.
- [63] M. Barringer, Design and Benchmarking of a Combustor Simulator Relevant to Gas Turbine Engines. MS Thesis, Virginia Polytechnic Institute and State University, 2001.
- [64] W. Lowry, J. de Vries, M. Krejci, E.L. Petersen, Z. Serinyel, W. Metcalfe, H. Curran, G. Bourque, *J Eng. Gas Turb. Power* 133 (2011) 091501-1- 091501-8.
- [65] M.C. Krejci, O. Mathieu, A.J. Vissotski, S. Ravi, T.G. Sikes, E.L. Petersen, A. Kéromnès, W. Metcalfe, H.J. Curran, *J Eng. Gas Turb. Power* 135 (2013) 021503-1- 021503-9.
- [66] W.K. Metcalfe, S.M. Burke, S.S. Ahmed, H.J. Curran, *Int. J. Chem. Kinet.* 45 (10) (2013) 638-675.
- [67] A.E. Dahoe, *J Loss Prevent. Proc.* 18 (2005) 152-166.
- [68] C. Mandilas, M.P. Ormsby, C.G.W. Sheppard, R. Woolley, *Proc. Combust. Inst.* 31 (2007) 1443-1450.
- [69] G. Bourque, D. Healy, H. Curran, C. Zinner, D. Kalitan, J.D. Vries, C. Aul, E. Petersen, *J Eng. Gas Turb. Power* 132 (2010) 021504-1- 021504-11.
- [70] W.B. Lowry, Effect of Blending on High-Pressure Laminar Flame Speed Measurements, Markstein Lengths and Flame Stability of Hydrocarbons, MS Thesis, Texas A&M University, 2010.
- [71] D. Healy, D.M. Kalitan, C.J. Aul, E.L. Petersen, G. Bourque, H.J. Curran, *Energ. Fuel* 24 (2010) 1521- 1528.
- [72] G. Yu, C.K. Law, C.K. Wu, *Combust. Flame* 63 (1986) 339- 347.

- [73] A. Morones, S. Ravi, D. Plichta, E.L. Petersen, N. Donohoe, A. Heufer, H.J. Curran, F. Güethe, T. Wind, Laminar and Turbulent Flame Speeds for Natural Gas/Hydrogen Blends at Elevated Pressures. ASME Turbo Expo GT 2014-26742, Düsseldorf, Germany, June 16- 20 (2014).
- [74] S. Chaudhuri, F. Wu, C.K. Law, Phys. Rev. E 88 (2013) 033005-1- 033005-13.
- [75] C.K. Law, Combustion Physics, Cambridge University Press, Cambridge, U.K., 2006.
- [76] H. Kido, M. Nakahara, K. Nakashima, J. Hashimoto, Proc. Combust. Inst. 29 (2002) 1855-1861.
- [77] Y-C. Chen, R.W. Bilger, Proc. Combust. Inst. 28 (2000) 521- 528.
- [78] A. Trouvé, T. Poinso, J. Fluid. Mech. 278 (1994) 1- 31.
- [79] V. Akkerman, C.K. Law, V. Bychkov, Phys. Rev. E 83 (2011) 026305-1- 026305-6.

APPENDIX A

FUNDAMENTALS OF TURBULENT FLOWS

The interaction of a turbulent flow and a flame needs to be understood to better design practical combustion systems such as gas turbines, internal combustion engines. While moderate levels of turbulence can improve mixing and burning rates of fuels, excessive levels may result in quenching and extinction. Similarly, a flame front can also alter a turbulent field. The thermal expansion occurring at the flame due to heat release results in an increase in the velocity component normal to the flame front, and such strong flow accelerations may induce flame-generated turbulence. On the contrary, the increased temperature from the heat of combustion results in a subsequent increase in kinematic viscosity of the medium causing the turbulent fluctuations to dissipate quickly (relaminarization of the flow).

This appendix provides an overview of important aspects of premixed turbulent combustion that are relevant to this study, and is organized as follows. First, an introduction to the basic features of turbulent flows is provided, followed by single-point correlations in homogenous and isotropic turbulence. The process of energy cascade and Kolmogorov hypotheses are then discussed. Two-point correlations are used to estimate the various relevant scales of turbulent motion. Finally, the properties of the spectra for turbulent kinetic energy and turbulent dissipation rates are presented.

1. Characteristics of turbulence

Reynolds number is a non-dimensional parameter that quantifies the influence of inertial forces to viscous forces acting in the flow. Flows can be classified as laminar, transitional, or turbulent. A laminar flow, typically observed at low Re , is smooth, uniform and predictable based on previous observations. In a transitional flow, small and distinct perturbations are superimposed on the smooth mean flow. Nevertheless, the perturbations are significantly lower when compared to the mean velocity, and the evolution of such perturbations can be well predicted by linear perturbation analysis. In a turbulent flow, however, the perturbation or velocity fluctuations are comparable or greater than the mean velocity, and the behavior of the flow becomes highly non-linear and unpredictable. The characteristics of turbulent flow include [A1],

- a. Multi-scale- a wide range of length and time scales characterize a turbulent flow
- b. Chaotic- a flow with strong sensitivity to initial and boundary conditions. Hence, statistical methods should be adopted for studying such flows.
- c. Diffusive- turbulent flow results in rapid mixing and increased rates of momentum, heat, and mass transfer. Subsequently, velocity fluctuations spread in the medium. Besides, turbulence has the tendency to eliminate steep gradients that may be present in the flow. For example, the velocity profile of a turbulent pipe flow is fuller when compared to the fully developed laminar flow (parabolic profile).
- d. 3-D and rotational flows- turbulent flows are three-dimensional and are rotational flows with high levels of fluctuating vorticity.

- e. Dissipative- The turbulent kinetic energy of the fluid is converted to internal energy through viscous action. A turbulent flow needs a constant source of energy, otherwise it decays owing to its dissipative nature.
- f. Continuum- The smallest scales of turbulent eddies (Kolmogorov scales) are still larger than the molecular scales of motion, and hence turbulent flow can be assumed to be a continuum phenomenon (except at low Re and high Mach numbers, but these conditions are not relevant to turbulent deflagrations).

2. Single-point correlation

The instantaneous velocity field in a turbulent flow can be decomposed (Reynolds decomposition) into mean (based on time or space or ensemble averaging) and fluctuating components such as,

$$u(x, t) = \bar{u}(x, t) + u'(x, t) \quad (\text{A1})$$

The root-mean-square velocity (u'_i) is used to quantify the magnitude of the velocity fluctuations. It should be noted that spatial and temporal coordinates are used with the fluctuating component to differentiate it from the RMS velocity.

$$\overline{u_i'^2} = \overline{(u_i - \bar{u}_i)^2} \quad (\text{A2})$$

Subsequently, the turbulent kinetic energy (k) can then be estimated as,

$$k = \frac{u'_i u'_i}{2} = \frac{1}{2}(u'^2 + v'^2 + w'^2) \quad (\text{A3})$$

While practical turbulent flows are extremely complex, simplifications such as stationary (invariance to temporal effects), homogeneous (invariance to spatial translation), and isotropic (invariance to rotations) turbulence can be adopted to better understand the underlying physics. In isotropic turbulence (single-point correlations) [A2],

$$\overline{u'^2} = \overline{v'^2} = \overline{w'^2} \quad (\text{A4})$$

$$u'(x, t) \neq v'(x, t) \neq w'(x, t) \quad (\text{A5})$$

$$\overline{u'(x, t)v'(x, t)} = \overline{v'(x, t)w'(x, t)} = \overline{w'(x, t)u'(x, t)} = 0 \quad (\text{A6})$$

$$k = 1.5u'^2 \quad (\text{A7})$$

3. Energy cascade and Kolmogorov hypotheses

An eddy is a turbulent fluid motion that is isolated within a region of size l (eddy dimension). The region occupied by a large eddy in a turbulent flow can also contain several smaller eddies [A3]. The largest eddies are characterized with length scales

comparable to the flow dimensions, and they break up, transferring energy to smaller eddies. This process of energy transfer is called the *energy cascade*, and the energy transfer continues until the eddy kinetic energy can be dissipated only through viscous action. Kolmogorov proposed three hypotheses to clarify the energy cascade process, and these hypotheses are considered as cornerstones in turbulent flow research.

The hypotheses stated below are taken from [A3].

a. First hypothesis- local isotropy

At sufficiently high Reynolds number, the small-scale turbulent motions are statistically isotropic.

b. Second hypothesis- first similarity hypothesis

In every turbulent flow, at sufficiently large Reynolds numbers, the statistics of the small-scale motions have a universal form that is uniquely determined by the mean dissipation rate ε and viscosity. However, the dissipation rate scales as u^3/l and is independent of viscosity. This range of scales is called the universal equilibrium range. Subsequently, the Kolmogorov scales can be defined as,

$$\text{Length: } \eta = \nu^{3/4} \varepsilon^{-1/4} \tag{A8}$$

$$\text{Time: } \tau_\eta = \nu^{1/2} \varepsilon^{-1/2} = \eta^{2/3} \varepsilon^{-1/3} \tag{A9}$$

$$\text{Velocity: } u'_\eta = (\nu\varepsilon)^{1/4} = (\eta\varepsilon)^{1/3} \quad (\text{A10})$$

$$\text{Reynolds Number: } Re_\eta = \frac{\eta u'_\eta}{\nu} = 1 \quad (\text{A11})$$

The various ratios of the smallest (η) to the largest scale (l) (assuming constant dissipation rate) can then be estimated as,

$$\text{Length: } \eta/l \sim Re_l^{-3/4} \quad (\text{A12})$$

$$\text{Velocity: } u_\eta/u_l \sim Re_l^{-1/4} \quad (\text{A13})$$

$$\text{Time: } \tau_\eta/\tau_l \sim Re_l^{-1/2} \quad (\text{A14})$$

It is imperative to point out two key features of these scaling laws. Though the difference between Kolmogorov and integral (largest) length scales is significant, the velocities are comparable. Second, the small-scale eddies have a higher strain rate (inverse of the time scales) when compared to larger eddies. This fact has profound implications to turbulent combustion [A2], wherein the mean turbulent stretch rate (arbitrary length L) can be expressed as,

$$\dot{s} = \frac{u'}{L} = \tau_L^{-1} \sim L^{-2/3} \varepsilon^{1/3} \sim \kappa^{2/3} \varepsilon^{1/3} \quad (\text{A15})$$

It can then be readily seen that the stretch rate scales with the wavenumber ($\kappa = 2\pi/L$), and that maximum stretch rate is associated with the smallest eddies. The increase in a surface area of a material surface (Ex. flame wrinkled by a turbulent flow) by eddy action can be expressed as $\frac{d \ln(A)}{dt} = \dot{s}$. Furthermore, it was also shown from DNS [A2] that $\frac{dA}{dt} \propto \frac{A}{\tau_\eta}$, providing evidence that the small-scale eddies in the turbulent flow control the change in $A(t)$.

c. Third hypothesis- second similarity hypothesis

In every turbulent flow, at sufficiently large Reynolds numbers, there is $\eta \ll l \ll L$ range of scales of turbulent motions, such that the statistics of eddies of scale l are uniquely determined by the mean dissipation rate ε but are independent of the viscosity. This range of scales is called the inertial range of the turbulent spectrum.

To summarize, the spectrum of eddies in a turbulent flow can be classified into two ranges: (1) energy-containing large-scale eddies that can be inhomogeneous and anisotropic; (2) universal equilibrium eddies which are statistically uniform and isotropic. The universal equilibrium range can be subdivided into inertial and dissipative scales. Turbulent kinetic energy is produced at the large-scale cascades in the inertial range and is eventually converted to internal energy in the dissipation range of the spectrum.

4. Two-point correlations

A turbulent flow is a collection of eddies of a wide range of velocity and length scales.

The two-point correlation tensor can then be defined as,

$$R_{ij}(x, r, t) = \overline{u'_i(x, t)u'_j(x + r, t)} \quad (\text{A16})$$

For HIT conditions, R_{ij} solely depends on the separation distance r between the two points and not on the position x inside the flow field. Then R_{ij} can be simplified as,

$$R_{ij}(r) = u'^2 \left\{ g(r)\delta_{ij} + [f(r) - g(r)] \frac{r_i r_j}{r^2} \right\} \quad (\text{A17})$$

Where $f(r)$ and $g(r)$ are called the longitudinal and transverse autocorrelation functions. The longitudinal (transverse) autocorrelation is associated with the normalized correlation between the same components of flow velocity vector, measured in two different points located on a line that is parallel (perpendicular) to the velocity components. Figure 35 shows the shapes of the correlation functions in HIT conditions. Furthermore, $R_{ij}=0$ when $i \neq j$. Other properties of the correlation functions include:

$$\text{Using continuity equation: } g(r, t) = f(r, t) + \frac{r}{2} \frac{\partial f(r, t)}{\partial r} \quad (\text{A18})$$

$$f(r \rightarrow 0) \rightarrow 1 \text{ and } g(r \rightarrow 0) \rightarrow 1 \quad (\text{A19})$$

$$f(r \rightarrow \infty) \rightarrow 0 \text{ and } g(r \rightarrow \infty) \rightarrow 0 \quad (\text{A20})$$

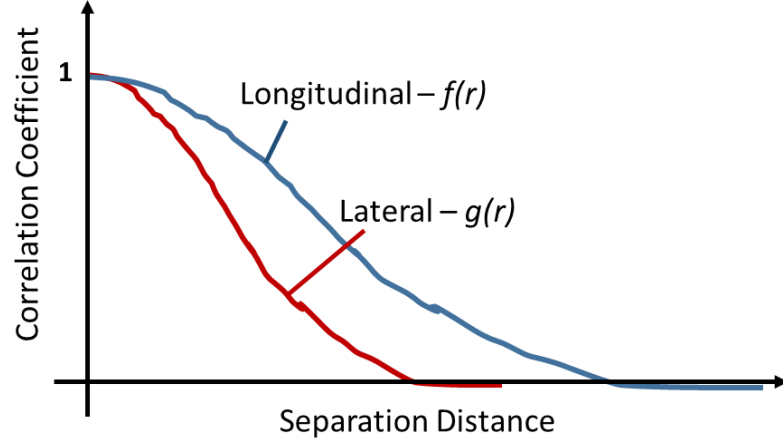


Figure 35. Variations of typical longitudinal and lateral correlation functions with separation distance. The areas under the curves yield the integral length scales. Also, the Taylor microscale is defined as the intersection of an osculating parabola at the origin with the abscissa.

a. Integral (Euler) scales

Typical shapes of the correlation functions are shown in Fig. 35. The longitudinal (L_{\parallel}) and transverse (L_{\perp}) integral length scales can then be defined as (areas under the respective correlation functions),

$$L_{\parallel} = \int_0^{\infty} f(r) dr \quad (\text{A21})$$

$$L_{\perp} = \int_0^{\infty} g(r) dr \quad (\text{A22})$$

From Eq. A18, and since $[r f(r)]_0^\infty = 0$, it can be shown that from A21 and A22,

$$L_\perp = \frac{1}{2}L_\parallel \quad (\text{A23})$$

b. Taylor scales

The longitudinal (λ_\parallel) and transverse (λ_\perp) Taylor microscales are then estimated as,

$$\lambda_\parallel = \left[-\frac{1}{2}f''(0, t) \right]^{-1/2} \quad (\text{A24})$$

$$\lambda_\perp = \left[-\frac{1}{2}g''(0, t) \right]^{-1/2} \quad (\text{A25})$$

They can be approximated as osculating parabolas about the origin (symmetric) whose equation is of the form,

$$p(r) = 1 - \frac{r^2}{\lambda^2} \quad (\text{A26})$$

The Taylor microscale is the radius at which the parabolas intersect the x-axis (see Fig.1).

Some useful properties of Taylor scales include,

$$\lambda_{\perp} = \frac{\lambda_{\parallel}}{\sqrt{2}} \quad (\text{A27})$$

$$\text{Relation with the integral scales: } R_{\lambda} = \frac{u'\lambda}{\nu} = \left(\frac{20}{3} \text{Re}_L\right)^{-1/2} \quad (\text{A28})$$

$$\text{Relation with the Kolmogorov scale: } \lambda/u' = (15\nu/\varepsilon)^{1/2} = \sqrt{15} \tau_{\eta} \quad (\text{A29})$$

5. Energy spectrum

The turbulent kinetic energy is distributed amongst eddies of different sizes. The turbulent kinetic energy contained in the wavenumber range (κ_A, κ_B) can then be estimated as,

$$k_{(\kappa_A, \kappa_B)} = \int_{\kappa_A}^{\kappa_B} E(\kappa) d\kappa \quad (\text{A30})$$

Where, $E(\kappa)$ is the energy-spectrum function.

The contribution to the dissipation rate is

$$\varepsilon_{(\kappa_A, \kappa_B)} = \int_{\kappa_A}^{\kappa_B} 2\nu\kappa^2 E(\kappa) d\kappa \quad (\text{A31})$$

From Kolmogorov's second hypothesis, the energy-spectrum function has a universal form in the inertial subrange and can be written as,

$$E(\kappa) = C \varepsilon^{2/3} \kappa^{-5/3} \quad (\text{A32})$$

This is the Kolmogorov -5/3 spectrum, and the C is the universal Kolmogorov constant (C=1.5 from experimental measurement). The log-log plot of the energy spectrum function (normalized by the Kolmogorov length scale) at $R_\lambda = 500$ is shown in Fig. 36. $E(\kappa)$ scales as κ^2 at low wavenumbers, $E(\kappa) \sim \kappa^{-5/3}$ in the inertial subrange, and decays exponentially at higher wavenumbers. Thus the energy-containing scales are restricted to large eddies (small wavenumbers).

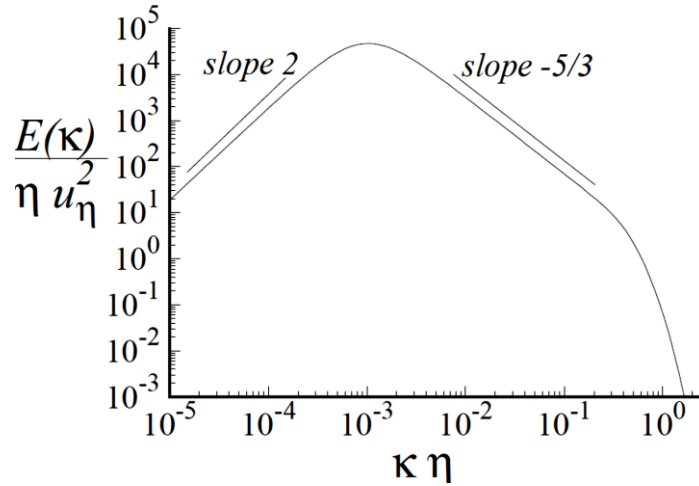


Figure 36. Energy-spectrum function normalized by the Kolmogorov length scale at $R_\lambda = 500$ (Reprinted with permission of Cambridge University Press and adapted from S. B. Pope, Chapter 6, pp. 182-263, *The Scales of Turbulent Motion in Turbulent Flows*, Copyright 2008 Stephen B. Pope).

The corresponding dissipation spectrum function is

$$D(\kappa) = 2\nu \kappa^2 E(\kappa) = 2\nu C \varepsilon^{2/3} \kappa^{1/3} \quad (\text{A33})$$

The dissipation spectrum and the cumulative dissipation function are shown at $R_\lambda = 600$ as a function of the wavelengths and wavenumbers (both normalized by the Kolmogorov length scale- Fig. 37). The shape of the dissipation function is consistent with the Kolmogorov hypotheses, and the peak dissipation scales with the Kolmogorov length scale (needs to be equal to η).

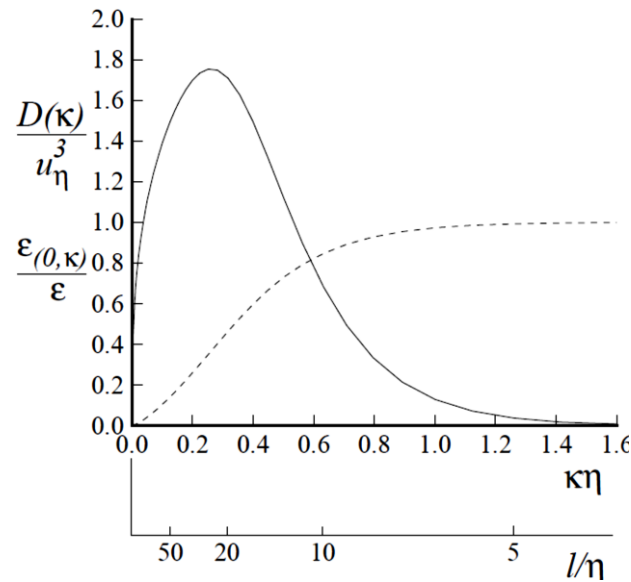


Figure 37. Dissipation spectrum (solid line) at $R_\lambda = 600$. The cumulative dissipation is also shown (dashed line) (Reprinted with permission of Cambridge University Press and adapted from S. B. Pope, Chapter 6, pp. 182-263, *The Scales of Turbulent Motion in Turbulent Flows*, Copyright 2008 Stephen B. Pope). For the Reynolds number considered herein, the dissipation is restricted to the higher wavenumbers [$(\kappa\eta \rightarrow 0)$ or $(l/\eta) \gg 1$].

It was shown earlier that the ratio of the Kolmogorov and Integral length scales can be related as a function of Reynolds number (based on the latter- Eq. A12). Such a scaling implies that the bandwidth of scales increases as the Re is increased. $E(\kappa)$ for various

Taylor Reynolds numbers are shown. When the wavenumbers are normalized by the integral length scale, the inertial subrange extends to higher wavenumbers (Kolmogorov scales reduce). Similarly, normalization by the Kolmogorov length scale shifts the energy-containing scales to lower wavenumbers. In both cases, the bandwidth between the energy-producing and energy-dissipating scales increases as the Reynolds number is increased (see Fig. 38).

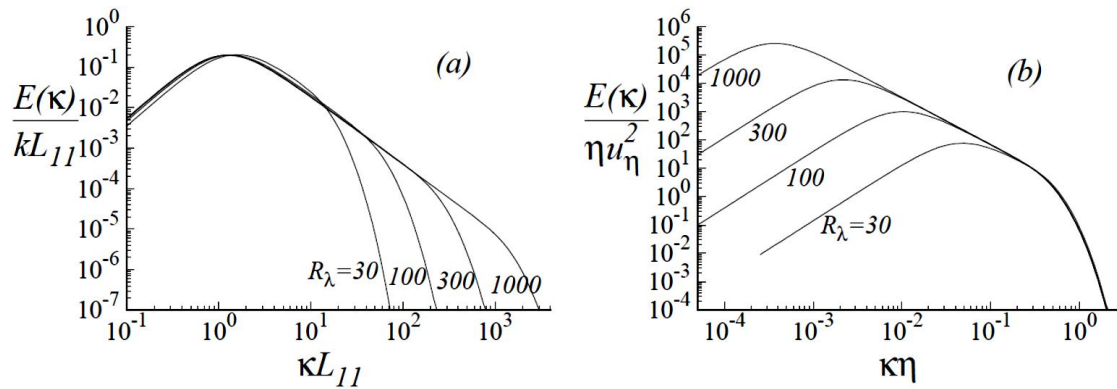


Figure 38. Energy spectra at various Re scaled with the integral scale in (a) and with the Kolmogorov scale in (b). (Reprinted with permission of Cambridge University Press and adapted from S. B. Pope, Chapter 6, pp. 182-263, *The Scales of Turbulent Motion in Turbulent Flows*, Copyright 2008 Stephen B. Pope). The separation of scales increases as Reynolds number is increased.

A final remark: the separation of scales is present only at sufficiently high Reynolds number consistent with the Kolmogorov hypotheses, and the energy and the dissipation spectra overlap at low Re, and a clear separation of scales is not observed [A3].

6. Non-dimensional numbers for turbulent combustion

In the inertial subrange of the turbulent spectrum, an eddy of arbitrary size l ($\eta < l < L_T$) can be related to its scaled velocity $u'(l)$ as,

$$\frac{u'(l)^3}{l} = \varepsilon \quad (\text{A34})$$

Where, ε is the dissipation rate of turbulent kinetic energy, and L_T is the integral length scale; and the turn over time for the eddy is given by

$$\tau(l) = \frac{l}{u'(l)} = \varepsilon^{-1/3} l^{2/3} \quad (\text{A35})$$

Premixed turbulent combustion can be considered as a laminar flame propagating into a turbulent flow and interacting with a wide range of eddies. The characteristic chemical time scale of a laminar flame is defined as,

$$\tau_c = \delta / S_{L,u}^\circ \quad (\text{A36})$$

Where,

$S_{L,u}^\circ$: is the unburnt, unstretched laminar flame speed.

$\delta = \nu / S_{L,u}^\circ$: is the Zeldovich flame thickness where ν is the kinematic viscosity

(Note: The Zeldovich flame thickness is used over the thermal thickness defined using the gradient method from chemical kinetics simulation, $\delta_L = (T_b - T_u) / \left(\frac{dT}{dx}\right)_{max}$, as the former results in unity Reynolds number for laminar flame propagation).

Damköhler number (Da) is defined as the ratio of the characteristic eddy timescale to the chemical time scale, τ_c . Da is typically defined for the largest eddy, namely, at the integral length scale.

$$Da = \frac{\tau_T}{\tau_c} = \left(\frac{u'}{S_L}\right)^{-1} \left(\frac{L_T}{\delta}\right) \quad (\text{A37})$$

Karlovitz number relates the smallest length scale of the Kolmogorov turbulence to the smallest length scale of the laminar flame, and is defined as,

$$Ka = \left(\frac{\delta}{\eta}\right)^2 = \left(\frac{u'}{S_L}\right)^{\frac{3}{2}} \left(\frac{L_T}{\delta_L}\right)^{-\frac{1}{2}} \quad (\text{A38})$$

The turbulent Reynolds number based on the integral length scale is defined as,

$$Re_T = \frac{u' L_T}{\nu} = \left(\frac{u'}{S_L}\right) \left(\frac{L_T}{\delta_L}\right) = (Da Ka)^2 \quad (\text{A39})$$

References

- [A1] H. Tennekes, J. Lumley, A First Course in Turbulence, The MIT Press, Cambridge, MA. 1972.
- [A2] A.N. Lipatnikov, Fundamentals of Premixed Turbulent Combustion, CRC Press, Boca Raton, FL. 2012.
- [A3] B. Pope, Turbulent flows, Cambridge University Press, Cambridge, U.K., 2000.